AN EVALUATION OF THE SENSITIVITY OF NUCLEAR MAGNETIC RESONANCE MEASUREMENTS TO HYDRAULIC PARAMETERS OF THE VADOSE ZONE

By

Samuel O Falzone

A dissertation submitted to the

Graduate School-Newark

Rutgers, the State University of New Jersey

In partial fulfillment of the requirements

For the degree of

Doctor of Philosophy

Graduate Program in Environmental Science

Written under the direction of

Dr. Kristina Keating

And approved by

_____

_____

_____

_____

Newark, New Jersey

January, 2016

THESIS ABSTRACT

An Evaluation of the Sensitivity of Nuclear Magnetic Resonance Measurements to Hydraulic Parameters of the Vadose Zone

By Samuel O Falzone

Dissertation Director:

Professor Kristina Keating

Hydrogeologic processes of the vadose zone have important implications for many environmental issues including agricultural practices such as irrigation, water resource management, and contaminant transport, among others. Current methods for characterizing the vadose zone involve invasive and sparse data collection techniques. While geophysics has the potential to measure hydrogeologic processes non-invasively, current geophysical measurements have not been widely used to study the vadose zone. Of interest in this study is developing nuclear magnetic resonance (NMR) as a means to investigate the vadose zone.

The first laboratory study in this thesis investigated the NMR relaxation time versus saturation curve of unconsolidated geologic media for samples exhibiting NMR relaxation in different diffusion regimes. Six synthetic sands were created that varied in both grain size and total iron content, in order to simulate different pore size distributions and surface relaxivities. The relative relaxation time versus saturation curve was found to

be linear for fast diffusion regime samples and a power law relationship for samples outside the fast diffusion regime. This study proves that samples in different diffusion regimes have different relaxation time versus saturation relationships.

The second laboratory study investigated the response in the NMR measurement due to hysteresis caused by drainage and imbibition. The water retention curves, WRC, of four synthetic sands and two loamy sand soils were measured with a porous plate experiment during both drainage and imbibition. Hysteresis was observed for the WRC's of all samples, but not observed for NMR parameters versus water content. This study proves that NMR is insensitive to differences in the WRC as expressed during drainage and imbibition.

Surface NMR is an NMR field measurement, which is capable of measuring a vertical profile of water in the subsurface, and offers a new way of studying the vadose zone. The third study investigated the ability of signal cancellation algorithms to remove the signal originating from a surface water layer present during a surface NMR measurement. An infiltration experiment resulted in a scenario in which the measurement loop was submerged in a layer of surface water. The algorithms presented in this study were capable of removing the signal originating from the surface water layer, resulting in a usable dataset for monitoring infiltration.

Acknowledgements

I would like to thank my advisor, Kristina Keating, for assisting and mentoring me through this process; and for providing insightful feedback on my work. I would also like to thank my committee members, Lee Slater, Dimitrios Ntarlagiannis, and Daniel Giménez for their support to this thesis.

I would like to thank Alec Gates, Yuan Gao, Kristina Keating, Lee Slater, and Dimitrios Ntarlagiannis for providing funding for living, travel, conference, material, and other assorted expenses necessary for the successful completion of this thesis. I thank Alan Allgeier, Roger Leach, and everyone else at the DuPont Experimental Station whom I had the pleasure of working with during my internship. I also would like to thank the New Jersey Water Resource Research Institute (NJWRRI), through which material funding for this thesis was provided.

I would like to thank Eiichi Fukushima, Hugh Daigle, Yanbin Yao, Mike Müller-Petke, and the anonymous reviewers for insightful comments and suggestions that have made the publications of the manuscripts in this thesis stronger. I thank Elliot Grunewald for providing additional comments focused on improving the data analysis and presentation of the surface NMR datasets.

I would like to thank Elliot Grunewald and David Walsh of Vista Clara for providing the SAVSARP datasets and their technical support. I would also like to thank Peter Turner of Vista Clara and Ty Ferré and Andrew Hinnell of Arizona State University for their work in collecting the surface NMR and ERT data. I would like to thank Carl Roiser from the Christina River Basin Critical Zone Observatory at the Stroud

Water Research Center for assistance in obtaining the natural soils used in this study. I also would like to thank Daniel Giménez for assistance in designing and setting up the porous plate experiment, as well as providing equipment used in the experiment. I would also like to thank John Nimmo for providing feedback on my research goals.

I would like to thank the faculty and staff of the Department of Earth and Environmental Science at Rutgers, the State University of New Jersey at Newark. I would especially like to thank Liz Morrin for providing critical assistance throughout this process. I would also like to thank my fellow graduate students in my research group, as well as other groups in the department, for their important advice and assistance.

Most of all, I would like to thank my family for providing philosophical support during this process. I thank my parents for keeping me grounded. I thank my Aunt and Uncle for providing insight into the PhD process and NMR concepts. I thank my brother for being a necessary diversion from time to time. I would also like to thank my dog, Iko, who sat at my feet the whole time I prepared this document. Most of all I would like to thank my wife for providing for me, both financially and spiritually, during this process, and for tolerating very long working hours and, at times, long times away from home – I am looking forward to spending more time with you and our future daughter.

Table of Contents

List of Figures

List of Tables

Chapter 1

Thesis Overview

1.1 Motivation

The Food and Agriculture Organization of the United Nations predicts that, in order to feed the growing world population, global food production must rise by 70% from 2005 levels by 2050 (HLEF, 2009). Driven by population growth and increasingly precious water resources, agricultural practices will need to become more efficient in the future in order to provide for increasing demand. In order to conserve water resources necessary for irrigation, a comprehensive understanding of subsurface hydrogeologic processes is necessary.

Nearly all water used for irrigating crops enters into the water cycle through the vadose zone, or the region between the root-zone and the water table. It is therefore important to understand the physical processes driving flow through this region in order to maximize production while conserving water resources. Studying how water flows through the vadose zone, however, relies on invasive probes and laboratory measurements. These measurements have the potential to disturb the natural state of soils and produce uncertain results. Geophysics however provides a means to study the subsurface without disturbing the natural state of soils, and has been successfully used to study subsurface hydrogeologic processes non-invasively (Slater et al., 2006). By relating the physics governing a geophysical measurement to the physics governing how water

moves through the subsurface, geophysical measurements can provide an alternative to standard methods for investigating the vadose zone (Ferré et al., 2007). One method in particular that has become well established in geophysical research for studying groundwater processes below the water table is nuclear magnetic resonance, NMR (Behroozmand et al., 2015). The ultimate goal of this thesis is to develop NMR as a geophysical method for investigating the vadose zone.

NMR is capable of investigating hydrogeologic processes because of its direct sensitivity to the amount of water in a pore space, by interpreting the signal magnitude of the measurement. The measurement is also capable of predicting the size of saturated pores, by interpreting the measurement's relaxation time (Seevers, 1966; Brownstein and Tarr, 1979; Godefroy et al., 2001). NMR has also been shown to be an effective field method, able to provide non-invasive surveys of groundwater to depths up to 100 m using surface based instruments (Legchenko et al., 2004) and borehole instruments (Knight et al., 2015). More recently, it has been shown that surface based instruments can monitor infiltration within the vadose zone (Walsh et al., 2014). By increasing our understanding of how NMR measurements relate to hydrogeologic processes of the vadose zone, NMR can inform our understanding of how best to manage water resources.

The research presented in this study is focused on further defining how the NMR relaxation time relates to hydrogeologic state variables characteristic, which govern the flow of water within the vadose zone. Chapters 2 explores the effect of physical and mineralogical characteristics on the interpretation of NMR measurements as a function of saturation. Chapter 3 explores the effect of drainage and imbibition processes on the NMR relaxation time. Finally, Chapter 4 develops cancellation algorithms for removing

standing water signal from a surface NMR measurement, in order to increase the sensitivity of the measurement to water within the subsurface.

1.2 Background

1.2.1 Vadose zone hydrogeology

Soils within the vadose zone are typically unsaturated, and contain a significant atmospheric gas phase within their pore space. Unlike in the saturated zone below the water table, in which water is typically under positive/outward pressure, water in the vadose zone is subjected to negative/adhesive forces due to the interaction of water with the mineral surface (Richards, 1931). Because of these adhesive forces, also known as capillary forces, water cannot be removed from unsaturated geologic media without being subjected to a positive/external force necessary to counteract them, such as suction (Buckingham, 1907). The energy state of water in unsaturated geologic media resulting from capillary forces is defined by the hydrogeologic state variable known as matric potential, ψ, which is typically defined in terms of negative pressure. As the ψ decreases (or gets more negative) the water content, θ, will decrease. Washburn's equation (Washburn, 1921) relates ψ to a pore size threshold known as the critical radius, r_c, which defines the maximum radius that can be saturated at a specific value of ψ known as the air entry value, ψ_c,

$$\psi_c = -\frac{2\gamma_{ls}\cos\Phi}{r_c}, \tag{1-1}$$

where γ_{ls} is the surface tension at the liquid-air interface and Φ is the contact angle of water on the pore surface, both resulting from cohesive and adhesive forces between the liquid and air phases, and the solid matrix. Consequently, the size of saturated pores within an unsaturated soil will vary due to changes in ψ; as ψ decreases, water is limited to smaller pores.

The water retention curve (WRC) defines the relationship of θ to ψ, and is used to explain how a soil will drain and imbibe water as capillary forces are overcome by environmental conditions. This relationship is characteristic of different soil types. Due to the relation of ψ to pore size as defined in equation 1-1, the WRC of a soil is related to the pore size distribution of a soil: soils with smaller pores will remain saturated at smaller ψ than soils with larger pores (Nimmo, 1997). Quantification of the WRC of a soil is necessary for determining hydrogeologic state variables such as the unsaturated hydraulic conductivity, or the ability of a soil to conduct water through its unsaturated pore space dependent on θ (Richards, 1931). Predicting how water will move through unsaturated soils is therefore dependent on characterizing the WRC. More information on these concepts can be found in Koorevaar et al. (1983).

The WRC is difficult to characterize because it is dependent on the specific drainage and imbibition history of a soil (Nimmo, 1992). During drainage, as ψ decreases, water will drain from pores with radii greater than r_c. The opposite is true during imbibition; as ψ increases, water will saturate pores with radii less than r_c. Hysteresis due to drainage and imbibition history can occur if pores have a regulating effect on the flow of water to or from pores. During drainage, smaller pores can block the

flow of water from larger pores, while during imbibition, larger pores can block the flow of water to smaller pores. This process results in separate discrete pathways of the WRC during drainage and imbibition, and can lead to uncertainty of how a soil will react to different environmental conditions (Likos et al., 2014).

1.2.2 Near-surface geophysical methods

Geophysical methods have proven useful for investigating hydrogeologic processes in the subsurface by providing non-invasive survey alternatives to conventional invasive methods (Sneider et al., 2007). Measurements of the saturated zone have shown the ability to determine hydraulic conductivity (Slater, 2007), identify fracture zones (Robinson et al., 2015), characterize ground water flow pathways (Wynn, 2002), and monitor biologically mediated contaminant degradation (Personna et al., 2013). Other studies have shown that geophysical methods may be relatable to the WRC (Muñoz-Castelblanco et. al., 2012). While geophysical methods have been adapted to study the vadose zone (Ferré et al., 2007), the petrophysical relationships between the measurements and physical processes characteristic of the vadose zone are still a source of ongoing research (Binley et al., 2005; Attwa and Günther, 2013).

While geophysical methods have been shown to be capable of measuring changes in θ in the vadose zone (Reedy and Scanlon, 2003), the ability of geophysics to measure ψ has not been proven. A geophysical measurement must be capable of determining both the θ and the ψ in order to successfully determine the WRC of soils. This thesis seeks to

continue the development of NMR for the study of the vadose zone by improving how the measurement is related to θ, ψ, and consequently the WRC.

1.2.3 NMR background

NMR has been adapted for use in geophysics as a surface instrument (Behroozmand et al., 2015) and as a borehole instrument (Walsh et al., 2013b). Recently, instruments have been developed specifically for measuring the vadose zone (Walsh et al., 2013a). While other geophysical measurements are indirectly sensitivity to θ of geologic porous media, NMR is capable of measuring θ directly because of its ability to measure the combined magnetization of protons in water within a pore space (Timur, 1969). Additionally, the NMR measurement has been shown to be sensitive to the physical properties of the pore space (Seevers, 1966; Brownstein and Tarr, 1979; Godefroy et al, 2001). The ability of the NMR measurement to directly detect water and to provide insight into the physical nature of saturated pores provides an opportunity for geophysics to monitor hydrogeologic processes, including those affecting flow in the vadose zone.

Nuclear magnetic resonance occurs in atoms with unpaired protons or neutrons that possess a non-zero nuclear spin angular momentum (Callaghan, 2011). This property provides a means to measure the presence of these atoms by generating external magnetic fields. Of specific interest in near-surface geophysics is the ability to measure hydrogen, which is primarily found in water and organic compounds in the subsurface. When hydrogen atoms, in which the most common isotope has a nucleus consisting of a single

unpaired proton, are placed in a static magnetic field, their nuclear magnetic spins will align with and precess about the field at the Larmor frequency, f_0. This frequency is proportional to the strength of the static magnetic field, B_0, and the gyromagnetic ratio of hydrogen,γ_H,

$$f_0 = \frac{\gamma_H}{2\pi} B_0 , \tag{1-2}$$

In NMR field measurements f_0 ranges from ~2 kHz for surface-based measurements to 2 MHz for borehole instruments. In laboratory measurements f_0 can be much higher (Callaghan, 2011). The NMR experiment begins when an energizing magnetic field, oscillating at f_0, tips the protons' magnetic spins out of alignment. When the applied field is removed, the protons' spins return, or relax, back to the axis of the static magnetic field. The change in the precession of the spins induces a measurable signal. This study focuses on the change in the transverse component of the NMR signal, $A_{XY}(t)$, with time, t, which describes the signal measured in the plane perpendicular to the static magnetic field.

In porous media, such as soils, $A_{XY}(t)$ is a multi-exponential decay,

$$A_{XY}(t) = \sum_i A_i e^{-t/T_{2i}} , \tag{1-3}$$

where A_i is the i^{th} signal component with a relaxation time of T_{2i}. Multi-exponential decay occurs because water in porous media occupies different physical environments. The sum of A_i, A_0, results from the combined magnetization of all energized protons, and is therefore proportional to the amount of water within the sample. In saturated porous media A_0 is related to the total porosity and in unsaturated porous media is linearly

proportional to the θ. $A_{XY}(t)$ is typically inverted to represent the distribution of A_{0i} versus T_{2i}, and is referred to as the T_2-distribution. The mean relaxation time of the sample is characterized by a single relaxation time, typically the geometric mean of the distribution, T_{2ML}.

The interpretation of the measurement is dependent on the specific mechanisms responsible for relaxation. There are three dominant mechanisms of relaxation in porous media: bulk fluid relaxation, T_{2B}, which occurs when protons couple with other protons within the fluid; surface relaxation (Bloembergen et al., 1961), T_{2S}, which occurs when protons couple with the pore surface; and diffusion relaxation (Brownstein and Tarr, 1979), T_{2D}, which occurs due to protons diffusing through magnetic field inhomogeneities (Keating and Knight, 2008),

$$\frac{1}{T_{2ML}} = \frac{1}{T_{2B}} + \frac{1}{T_{2S}} + \frac{1}{T_{2D}}. \tag{1-4}$$

In porous media, T_{2S} is usually the dominant relaxation mechanism, and $T_{2ML} \approx T_{2S}$. The petrophysical relationship discussed in Godefroy et al. (2001) relates relaxation time to the mean pore radius, r_{ML}, for saturated samples,

$$T_{2ML} = \frac{r_{ML}}{\rho_2 \alpha} + \frac{r_{ML}^{\,2}}{2\alpha D}, \tag{1-5}$$

where D is the self-diffusion coefficient of water, α is the shape parameter of the pore (α = 1, 2, or 3; for planar, cylindrical, and spherical pores respectively), α/r_{ML} is the mean surface-area-to-volume ratio, and ρ_2 is the surface relaxivity, which defines the ability of the pore surface to enhance relaxation. ρ_2 is dependent on the presence of paramagnetic

sites on the pore surface, such as Fe(III) bearing minerals. The relaxation time is therefore sensitive to both pore size and the mineralogical characteristics of the porous media (Keating and Knight, 2007); both these characteristics can influence relaxation in similar ways. Directly relating relaxation time to pore size is therefore dependent on an understanding of ρ_2, which is difficult to characterize. Pore size and ρ_2 can also change the fundamental interpretation of the NMR measurement.

Different interpretations of the relaxation time are described by diffusion regimes, which define how water will move through, and consequently sample, a pore volume during an NMR measurement (Brownstein and Tarr, 1979). As pore size and ρ_2 increase, the relation of NMR relaxation to pore size changes. When a sample is in the fast diffusion regime, in which the diffusing protons are sampling the entire pore volume within the course of an NMR measurement, relaxation of all protons will be averaged within a single pore and $A_{XY}(t)$ from each pore is mono-exponential,

$$A_{XY}(t) = A_0 e^{-t/T_2}. \tag{1-6}$$

In the fast diffusion regime, the relaxation time is predominantly sensitive to the pore size; in this case the first term of equation 1-5 is dominant, and there is a linear relationship between relaxation time and pore size. If pore size and ρ_2 are large, to the extent that protons are incapable of sampling the entire pore volume during the measurement, the sensitivity of relaxation to pore size is reduced. In this case, relaxation is said to occur outside the fast diffusion regime, and $A_{XY}(t)$, from a single pore, is multi-exponential as expressed in equation 1-2. Relaxation in this case is still related to pore

size, but now the second term in equation 1-5 is dominant and the relaxation time is a function of r^2.

Investigating the vadose zone with NMR requires understanding how the measurement changes as a function of saturation in addition to differences in the interpretation of the measurement resulting from different diffusion regimes. Equation 1-5 is based on the assumption that the pore space is saturated. In unsaturated samples, however, signal originates from, and the relaxation time is only sensitive to, the water saturated fraction of the pore space (Costabel and Yaramanci, 2011b). Because the size of saturated pores varies as a function of saturation as defined in equation 1-1 (Washburn, 1921), the NMR relaxation time is also a function of saturation (Bird and Preston, 2004; Ioannidis et al., 2006; D'Orazio et al., 1990; Falzone and Keating, 2016a). Additional research however is required to relate relaxation time to ψ in unsaturated porous media before NMR can be used to effectively study the vadose zone. What is not well understood is how to interpret relaxation time as a function of saturation when samples exhibit relaxation in different diffusion regimes. Relating relaxation time to ψ also requires an understanding of how the measurement is effected by hysteresis. It is also important to demonstrate the ability of field NMR measurements to obtain a quality of field data that is capable of observing these relationships.

1.3 Summary of Research

The focus of this thesis is to address two research topics concerning the successful use of NMR as a field method to investigate the vadose zone: how NMR relaxation time

measurements of unconsolidated geologic media are affected by variations in saturation and ψ, and whether NMR field methods can be used to obtain reliable measurements of water within the vadose zone. This thesis is divided into three chapters to address these research topics. The first two chapters focus on defining the relationship of relaxation time to saturation and relating this relationship to the WRC. The final chapter focuses on improving the quality of data obtained from field NMR measurements to study the vadose zone. Each chapter has been previously submitted to a peer-reviewed scientific journal for publication. References for all papers have been consolidated at the end of this manuscript for simplicity.

1.3.1 A laboratory study to determine the effect of pore-size, surface relaxivity, and saturation on NMR T_2 relaxation measurements

Chapter 2 presents the results from a laboratory study to determine the relation of NMR relaxation time to saturation in samples that occupy different diffusion regimes, which occur due to different physical characteristics, such as the ρ_2 and the pore size distribution. While previous studies have presented models for how NMR relaxation varies as a function of saturation (Costabel and Yaramanci, 2011a; Costabel, 2011; Mohnke et al., 2015), these models have not been tested for a wide range of soil types. Sands were synthetically modified to produce samples with distinct mean grain diameters and total iron contents in order to vary pore size and ρ_2. The saturation of these samples was then increased in order to evaluate the relative T_{2S} versus saturation curve. Models based on ideal filling mechanisms and pore structures are presented to explain this

relation. The findings of this study show that the relative NMR relaxation time versus saturation curve is more complicated than simple models predict, and can vary dependent on different diffusion regimes. This chapter was published in the journal *Near Surface Geophysics* (Falzone and Keating, 2016a).

1.3.2 The NMR relaxation response of unconsolidated sediments during drainage and imbibition

Chapter 3 presents a laboratory study focusing on the effect of hysteresis, due to drainage and imbibition, on the NMR relaxation time measurement. Whether NMR relaxation times exhibit hysteresis due to drainage and imbibition is currently disputed in the literature. Mohnke et al. (2015) presented a numerical model that predicts the NMR relaxation time versus θ curve will display hysteresis. Contrary to this prediction, in Porion et al. (1998) it was observed that NMR relaxation time versus θ did not exhibit hysteresis. In the laboratory study presented in Chapter 3, NMR measurements were collected from a porous plate experiment during drainage and imbibition for a wide range of soils at magnetic field strengths similar to those used for NMR field measurements (2 MHz). Gravimetric measurements of the WRC, also obtained during the porous plate experiment, show well defined hysteresis loops for all samples; however, the NMR relaxation time versus saturation curves do not exhibit hysteresis. These findings confirm the observations of Porion et al. (1998) and contradict the predictions of Mohnke et al. (2015), by showing that NMR relaxation times are not sensitive to differences in drainage

and imbibition. This chapter has been submitted for publication to *Vadose Zone Journal* (Falzone and Keating, 2016c).

1.3.3 Algorithms for removing surface water signals from surface NMR infiltration surveys

Unlike Chapters 2 and 3, Chapter 4 focuses on a problem associated with surface NMR measurements of the vadose zone: signal originating from surface bodies of water involved in an infiltration test. Chapter 4 focuses on removing this unwanted signal source from surface NMR datasets, so that the sensitivity of the measurement to signal originating from water in the vadose zone is maximized. The three algorithms presented in this study were demonstrated to successfully remove signal from surface water associated with a ground water storage and recovery site from datasets collected during the infiltration survey first published in Walsh et al. (2014). The data in this study proves that surface NMR, through additional processing steps, can be adapted for studying the vadose zone, and proves that complications from infiltration tests can be corrected. This chapter has been submitted for publication to *Geophysics* (Falzone and Keating, 2016b), and is currently in review.

Chapter 2

A Laboratory Study to Determine the Effect of Pore-Size, Surface Relaxivity, and Saturation on NMR T_2 Relaxation Measurements[1]

2.1 Abstract

In this study we present laboratory experiments investigating the effect of pore-size and surface relaxivity, ρ_2, on the nuclear magnetic resonance (NMR) response of variably saturated sands that relax both within and outside the fast diffusion regime. We measured the NMR response of sands with a range of grain sizes (129 to 753 μm), which resulted in samples with different pore-sizes, and a range of iron concentrations (0.07% to 0.38%), which resulted in sands with different ρ_2 values. The laboratory results showed that the relation between relaxation time and water saturation depended on the regime in which relaxation occurred. For samples relaxing in the fast diffusion regime (i.e., small pores, low surface relaxivity), the relation between relaxation time and water saturation was linear; for the remaining samples, the relation between relaxation time and saturation demonstrated a power law relationship with an exponent greater than one. In addition we performed numerical simulations based on common pore-filling mechanisms (i.e., capillary tubes or thin films). The numerical simulations did not predict the experimental results for the relative surface relaxation versus saturation trends. We conclude that, in addition to the diffusion regime in which relaxation occurs, the shape of the relaxation time versus saturation curve depends on the pore-filling mechanism, the

[1] Published in *Near Surface Geophysics* as Falzone and Keating (2016a)

value of ρ_2, and the pore-size. The dependence of NMR relaxation on the pore-filling mechanism of saturating porous media may complicate efforts to develop a relation between relaxation time and saturation for use in characterizing unsaturated porous media.

2.2 Introduction

Nuclear magnetic resonance (NMR) measurements are used in geophysics to probe the pore-scale environment of water (or oil) bearing geologic material. The measurement is unique in geophysics as it is the only method that can directly detect hydrogen. NMR has been used since the 1950's to characterize petroleum reservoirs (e.g., Kenyon, 1991; Brown and Fatt, 1956); more recently, instrumentation has been developed that allows NMR to be used for hydrogeologic investigations of the top 100 m of the subsurface (e.g., Behroozmand et al., 2015; Legchenko et al., 2002; Yaramanci et al., 2002; Yaramanci and Müller-Petke, 2009; Walsh et al., 2010). NMR measurements can be made in the field using a surface-based instrument, which consists of a large wire loop laid out on the ground, or in a borehole using a well-logging instrument (Müller-Petke et al., 2011b; Knight et al., 2012). When used for hydrogeologic investigations, the NMR measurement is typically used to estimate variations in water content and hydraulic conductivity with depth. Although NMR is not widely used to investigate unsaturated sediments, instrumentation has recently been developed that is capable of collecting high-resolution, non-invasive measurements of the top ~1 m of the surface and has the potential to provide a fast and inexpensive method for characterizing the vadose zone (Walsh et al., 2014). In addition to field instruments, laboratory NMR instruments are used to characterize the NMR response of materials, to improve petrophysical relations, and to test novel applications of NMR, such as estimating mobile versus immobile porosity or determining the size and orientation of clay platelets (Swanson et al., 2012; Porion et al., 2010). Of interest in our research is improving the interpretation of NMR

measurements in unsaturated, unconsolidated materials for use in characterizing in the vadose zone.

The NMR signal is an exponential decay, characterized by an initial signal amplitude, A_0, and a distribution of relaxation times, or T_2-distribution. A_0 is directly proportional to the number of relaxing hydrogen atoms and can be used to determine the volume of water present within a sample. The interpretation of NMR data in geophysics typically assumes that the measured volume is fully saturated (e.g., Behroozmand et al., 2015; Kenyon, 1991; Knight et al., 2012; Mohnke and Yaramanci, 2008; Seevers, 1966), in which case A_0 is proportional to the total porosity. Assuming that relaxation occurs in the fast diffusion regime (i.e., that protons can move through and sample an entire pore within the time scale of the NMR measurement), in a saturated sample, the T_2-distribution is related to the pore-size distribution, PSD (Kenyon et al., 1988; Seevers, 1966; Timur, 1969). In this case the average relaxation time (determined from the T_2-distribution) is proportional to the average pore radius and consequently inversely proportional to the surface-area-to-volume ratio (Seevers, 1966); the constant of proportionality is called the surface relaxivity. It is the relation between the T_2-distribution and the surface-area-to-volume ratio that allows NMR measurements to be used to estimate the hydraulic conductivity (e.g., Knight et al., 2012). We are interested in expanding the NMR theory developed for saturated geologic media and applying it to geologic media with varying degrees of saturation to extend the use of NMR measurements to characterize the vadose zone.

While the literature on NMR measurements of water-saturated materials is extensive, there are only a limited number of studies that focus on the interpretation of

NMR measurements for applications in the vadose zone. Such studies have shown that the T_2-distribution, via its relation to the PSD, can be used to estimate the water retention curve (e.g., Costabel and Yaramanci, 2011b; Costabel and Yaramanci, 2013; Jaeger et al., 2009); however, this interpretation requires that the NMR measurement be collected on a fully saturated sample and that relaxation occurs in the fast diffusion regime. For NMR measurements made on unsaturated geologic media, as noted by Costabel and Yaramanci (2011a), the T_2-distribution is not a measure of the PSD, but rather a measure of the distribution of the water within the pore space at a specific degree of saturation. This observation is confirmed by experiments showing that the T_2-distribution and the average relaxation time are a function of saturation (Chang and Ioannidis, 2002; D'Orazio et al., 1990; Jaeger et al., 2009; Pohlmeier et al., 2009; Stingaciu et al., 2009; Yao et al., 2015). Because of this relation, a number of studies have successfully estimated the unsaturated hydraulic conductivity and the water retention curve for unsaturated, unconsolidated materials (Bird and Preston, 2004; Costabel and Yaramanci, 2011a; Costabel and Yaramanci, 2013; Chen et al., 1994; Ioannidis et al., 2006). However, while these studies demonstrate the value that NMR measurements have for estimating vadose zone properties, the experiments were conducted using simple materials (e.g., glass bead or clean sands), and it is not known if the results can be extended to more complex geologic media.

A number of factors have been shown to complicate the interpretation of NMR data in saturated geologic media and we anticipate that such factors will have a similar impact on the interpretation of NMR data in unsaturated geologic media. First, the surface relaxivity, which is used to determine pore-size from NMR measurements, is

strongly affected by the presence, concentration and mineral form of iron(III) (Keating and Knight, 2007; Foley et al., 1996; Bryar and Knight, 2002). Increases in the concentration of iron(III) on the surface of a pore will decrease the relaxation time. Second, the standard interpretation of NMR data assumes that relaxation occurs in the fast diffusion regime; however, it has been shown that for unconsolidated materials with large pores and high iron(III) concentration relaxation can occur outside the fast diffusion regime (i.e., the slow or intermediate diffusion regime; Dlugosch et al., 2013; Hinedi et al., 2010). Third, the presence of magnetic minerals such as magnetite can cause inhomogeneities in the magnetic field, which also enhances relaxation (e.g., Keating and Knight, 2008). In this study, we focus on the first two factors stated here and address the following research question: What is the effect of variations in surface relaxivity and pore-size, and consequently the diffusion regime, on the relation between NMR relaxation time and water saturation? While we expect that magnetic minerals will also have an impact on this relation, for simplicity we leave understanding their effects on the relation between NMR relaxation time and water saturation to another study. To the best of the authors' knowledge, no study has been published that systematically investigates the relation between NMR relaxation time and water saturation for geologic media with a range of surface relaxivity values and pore-sizes.

To understand how varying surface relaxivity and pore-size affects the relation between NMR relaxation time and water saturation, we collected laboratory measurements on sand packed columns. To vary the surface relaxivity, the iron(III) concentration was varied by coating the surface of the sands with different concentrations of the iron-oxide mineral hematite. To vary the pore-size, we used sands with different

grain sizes. Samples with large pores and high surface relaxivity were expected to violate the fast diffusion assumption. NMR measurements were then collected while the samples underwent imbibition. The results from the laboratory measurements were compared to numerical simulations of the NMR response of pore systems during imbibition. The simulations were performed for pore systems with a range of pore-sizes and surface relaxivities expected in natural sands using two different pore-filling mechanisms. This study improves the interpretation of NMR relaxation data collected in the vadose zone by providing an understanding of the effect of pore characteristics on the NMR response of unsaturated geologic media.

2.3 Background

The NMR phenomenon occurs in atoms with unpaired protons or neutrons that possess a non-zero nuclear spin angular momentum, such as hydrogen with a nucleus consisting of a single proton (Callaghan, 2011). When hydrogen atoms are placed in a static magnetic field their nuclear spins align with and precess about the field. The frequency of precession, called the Larmor frequency, is proportional to the strength of the static magnetic field. For geophysical studies the Larmor frequency ranges from ~2 kHz for surface-based measurements, which are collected in the Earth's magnetic field, up to over 300 MHz for laboratory studies in which strong magnets are used to generate the static magnetic field (e.g., Rassi et al., 2011). The measurements made in this study were collected at a Larmor frequency of 2 MHz, which is within an order of magnitude of the frequency used in most well-logging instruments. The NMR experiment begins when an oscillating magnetic field, tuned to the Larmor frequency, is applied, tipping the spins

out of alignment with the static field. When the applied field is removed, the protons return, or relax, back to their equilibrium position. The change in the precession of the spins in the static magnetic field induces a measurable signal. This study focuses on the change in the transverse component of the NMR signal, or the component of the magnetization in the plane perpendicular to the static magnetic field, $M_{XY}(t)$, with time, t, as this is the component of the magnetization that is most commonly measured in near-surface NMR applications. To measure $M_{XY}(t)$, and determine the transverse relaxation time, T_2, we use a CPMG pulse sequence (Carr-Purcell-Meiboom-Gill; Carr and Purcell, 1954; Meiboom and Gill, 1958). The CPMG pulse sequence is a 90^o pulse, followed by a series of refocusing 180^o pulses with alternating phase angles, separated by the echo spacing, t_E. The purpose of the refocusing pulses is to reduce dephasing of the precessing protons due to magnetic field inhomogeneities. Data are collected halfway between the 180^o pulses, by measuring the echo produced when the phases of the precessing protons are maximally realigned. Additional details on the CPMG pulse sequence can be found in Callaghan (2011) and Dunn et al. (2002).

2.3.1 NMR relaxation in a single pore

We start by considering the NMR response of the simple case of water in a single water-saturated pore. In this case, $M_{XY}(t)$ is described by a multi-exponential decay (Brownstein and Tarr 1979),

$$M_{XY}(t) = M_0 \sum_k f_k e^{-t/T_{2Sk}} , \qquad (2\text{-}1)$$

where M_0 is the initial magnetization and is proportional to the number of protons, or the volume of water, in the pore and f_k is the relative amplitude of each component of the magnetization decaying with a surface relaxation time of T_{2Sk}. Values of T_{2Sk} are ordered from longest to shortest, with the longest mode represented by T_{2S0}, the zeroth mode surface relaxation time. In equation 2-1 we have neglected the component of relaxation corresponding to the bulk fluid relaxation time and the effect of inhomogeneities in the static magnetic field. We note that the effect of bulk fluid relaxation can be accounted for in the laboratory by collecting measurements on the bulk fluid; the effect of inhomogeneities in the static magnetic field can be accounted for by collecting measurements at multiple t_E values.

Brownstein and Tarr (1979) showed that in a single pore the relaxation behavior can be separated into three diffusion regimes: the slow, intermediate, and fast diffusion regime. The boundary of the diffusion regimes is defined by the control parameter, κ,

$$\kappa \equiv \frac{\rho_2 a}{D}, \tag{2-2}$$

where a is the average distance a proton can travel within the time scale of an NMR measurement, equivalent to the pore radius for a single pore. D is the self-diffusion coefficient of water (D=2.46×10^{-9} m^2·s for water at 30°C). ρ_2 is the surface relaxivity, a measure of the ability of the pore surface to decrease the relaxation time, which is a function of the concentration and distribution of paramagnetic ions on the surface of the pore (e.g., iron(III) and manganese(II); Foley et al., 1996).

In the slow and intermediate diffusion regimes, which we refer to as “outside the fast diffusion regime”, relaxation occurs at the pore surface but the decay of magnetization is controlled by the diffusion of the spins to/from the surface of the pore. In this case, the distribution of magnetization within the pore is both time-dependent and non-uniform (Kleinberg et al., 1994). The slow diffusion regime is defined by $\kappa >> 10$; in this regime >60% of the signal relaxes with T_{2S0}. The intermediate diffusion regime is defined by $1 << \kappa << 10$; in this regime >95% of the signal relaxes with T_{2S0}.

In the fast diffusion regime, also called the surface limited regime, the relaxing spins can diffuse through the entire pore space within the time scale of the NMR measurement and the rate of decay of magnetization is governed by relaxation at the surface of the pore. The fast diffusion regime is defined by $\kappa << 1$; in this regime the relaxation in a single pore is represented by a single exponential decay, i.e., 100% of the signal relaxes with T_{2S0}. In this study we use the limit, $\kappa \leq 0.1$ to determine the fast diffusion regime, which was said to be a sufficient condition for fast diffusion by Ryu (2009).

Generally, T_{2S0} is given by (Godefroy et al., 2001),

$$\frac{1}{T_{2S0}} = \frac{1}{\frac{a}{\alpha\rho_2} + \frac{a^2}{2\alpha D}}. \tag{2-3}$$

where α is a shape parameter (α=1 for planar pores, 2 for cylindrical pores, and 3 for spherical pores). In the case of fast diffusion, the first term in the denominator dominates; for simple pores $\alpha/a = S/V$, where S/V is the surface-area-to-volume ratio of the pore and so equation 2-3 reduces to (Godefroy et al., 2001; Seevers, 1966),

$$\frac{1}{T_{2S0}} = \rho_2 \frac{S}{V}. \tag{2-4}$$

In the slow diffusion regime, the second term of the denominator of equation 2-3 dominates.

2.3.2 NMR relaxation in geologic media

The previous discussion focused on relaxation in a single pore; however, geologic media consists of multiple pores with multiple pore environments. In water saturated geologic media the measured NMR signal, $A_{XY}(t)$, is a multi-exponential decay even in the fast diffusion regime,

$$A_{XY}(t) = A_0 \sum_i h_i e^{-t/T_{2i}}, \tag{2-5}$$

where A_0 is the initial signal magnitude and is proportional to the volume of water in the measured sample, h_i is the proportion of the signal relaxing with a relaxation time of T_{2i}, and the sum is taken over all relaxation environments. In saturated samples, A_0 is proportional to the total porosity. We note that in equation 2-5, unlike equation 2-1, the bulk fluid relaxation time of the saturating water, T_{2B}, has not been neglected. The relation between T_{2i}, the i^{th} surface relaxation time, T_{2Si}, and T_{2B} is,

$$\frac{1}{T_{2i}} = \frac{1}{T_{2Si}} + \frac{1}{T_{2B}}. \tag{2-6}$$

The value of T_{2B} is affected by temperature, due to associated changes in the viscosity of water, and by dissolved paramagnetic ions (Bloembergen and Morgan, 1961). If

relaxation occurs in the fast diffusion regime and, if the additional assumption is made that ρ_2 is constant across all pores, each value of T_{2i} in equation 2-5 corresponds to a specific pore-size. The T_2-distribution is then a linear transformation of the PSD (e.g., Bird and Preston, 2004). When fast diffusion cannot be assumed the T_2-distribution still represents the PSD but is not a linear transformation (Keating and Falzone, 2013). In practice, a single relaxation time, the mean-log relaxation time, T_{2ML}, is used to represent the T_2-distribution and is calculated from,

$$T_{2ML} = \sum_i h_i \log T_{2i} \ . \tag{2-7}$$

Equation 2-6 then becomes,

$$\frac{1}{T_{2ML}} = \frac{1}{T_{2S}} + \frac{1}{T_{2B}}, \tag{2-8}$$

where T_{2S} is the mean-log surface relaxation time across all pores. In geologic media, T_{2B} is typically much longer than T_{2S}, and therefore $T_{2ML} \sim T_{2S}$ in most cases. T_{2ML} is related to the average pore-size or S/V using equation 2-3 or 2-4. A third term in equations 2-6 and 2-8 accounting for inhomogeneities in the magnetic field, the diffusion relaxation time, has been neglected as it was found to be negligible for the materials used in this study (Keating and Falzone, 2013). κ for geologic material can now be calculated using equation 2-2 with r_{ML}, the average pore radius, substituted for a. For additional information concerning these concepts, see Dunn et al. (2002).

2.3.3 NMR relaxation in unsaturated porous media

The interpretation of NMR measurements of saturated porous media is not directly transferable to unsaturated porous media. For example, unlike in saturated media, in unsaturated porous media, A_0 is not proportional to total porosity. However, A_0 is proportional to the water saturation, S_W. Following the notation of Costabel and Yaramanci (2011b), the NMR estimated water saturation, S_{NMR}, which is assumed to be equivalent to S_W, is calculated from,

$$S_{NMR} = \frac{A_0 - A_{0,Res}}{A_{0,Sat} - A_{0,Res}}, \tag{2-9}$$

where $A_{0,Res}$ and $A_{0,Sat}$ are the initial NMR signal magnitude from measurements of samples at residual and full saturation respectively.

While many studies have shown that the relaxation time varies as a function of saturation, only one study by Costabel and Yaramanci (2011b) quantified this relation. Costabel and Yaramanci developed a model based a capillary tube model, i.e., the idea that the soil pore space behaves as a bundle of capillary tubes. In this model at a given suction there is a critical radius r_c that determines whether a pore is empty or filled. Pores with radii, r, greater than r_c are empty while pore with r less than or equal to r_c are filled. Based on the assumption the T_{2ML} is proportional to r_c, Costabel and Yaramanci (2011b) introduced a Brooks-Corey parameterization of unsaturated NMR measurements, in which there is a power law relation between T_{2S0} and S_{NMR},

$$S_{NMR} = \left(\frac{T_{2S0}}{T_{2S0,Sat}} \right)^{\lambda}, \tag{2-10}$$

where $T_{2S0,Rel}$ is the relative T_{2S0}, or the value of T_{2S0} at a specific degree of saturation divided by $T_{2S0,Sat}$, the relaxation time at saturation, and λ is a fitting parameter, assumed to correspond to the parameter relating matric potential to saturation in the Brooks-Corey model of the water retention curve (Brooks and Corey, 1964). Equation 2-10 is consistent with the relation between relaxation time and saturation seen in a number of previous studies (e.g., Chen et al., 1994; Costabel and Yaramanci, 2011a). In particular, $\lambda \geq 1$ for the porous glass materials (Vycor and VitraPOR #5) with pore diameters of 4 nm and 1 μm (Mattea et al., 2004), for glass beads with mean diameters of 300 μm (Ioannidis et al., 2006), and for industrial sands with low iron(III) concentrations and mean grain diameters ranging from 0.06 mm to 2 mm (Costabel and Yaramanci, 2011b). While Ioannidis et al. (2006) and Mattea et al. (2004) examined the longitudinal relaxation time versus S_W relation, this relation is parallel to the $T_{2S0,Rel}$ versus S_W relation when T_{2B} is constant and diffusion relaxation is negligible (Dunn et al., 2002). Costabel and Yaramanci (2011b) speculated that the value of λ depends on the homogeneity of grain size of the materials measured with λ~0.1 for very inhomogeneous material and as high as ~2 for very homogeneous material. However, what has not been considered is the effect of ρ_2, pore-size, and consequently diffusion regime, on the $T_{2S0,Rel}$ versus S_W relation. In our work we examine the effects of ρ_2, via the iron(III) concentration, and the pore-size, via the mean grain diameter, d_{mean}, on the NMR relaxation response of unsaturated geologic media. We first present NMR measurements made on sand packed columns, with a range of iron(III) concentrations and d_{mean}. We next numerically simulate the relation between $T_{2S0,Rel}$ and S_W using two simplified pore-filling mechanisms.

Finally, we compare results of the numerical simulations to the results of the laboratory measurements.

2.4 Laboratory Methods and Materials

2.4.1 Sample preparation

The effect of surface relaxivity and pore-size on the relation between NMR relaxation time and water saturation was examined by making NMR measurements on columns packed with sand. Silica sand (99.5% SiO_2, 0.157% Al_2O_3, 0.084% Fe_2O_3; Best Sand Corporation) was used as an analog for a naturally occurring material. To ensure that the samples had a range of pores sizes, we used sands with three ranges of grain sizes: fine sand (grain diameters from 88 to 149 μm), medium sand (grain diameters from 149 to 210 μm), and coarse sand (grain diameters from 400 to 841 μm).

To make samples with different surface relaxivities, the iron(III) concentration on the surface of the sand grains was varied. Two subsets of each grain size range were coated with different concentrations of hematite (Fe_2O_3) (low-concentration and high-concentration) (synthesized following the method of Schwertmann and Cornell, 1991; further details provided in Keating and Falzone, 2013); a third subset of each grain size range was left uncoated. This procedure resulted in nine samples: uncoated, low-coated, and high-coated fine sand, referred to as uF, lF, and hF respectively; uncoated, low-coated, and high-coated medium sand, referred to as uM, lM, and hM respectively; and uncoated, low-coated, and high-coated coarse sand, referred to as uC, lC, and hC respectively (Table 2-1). All samples were washed by flowing water through a column

packed with the sand for 8 hours at a flow rate of 50 μL/min; prior to the NMR experiments the samples were dried in an oven at 80°C overnight.

Table 2-1. Sample descriptions and names.

Sample Description	Sample Name
Uncoated Fine Sand	uF
Low-Coated Fine Sand	lF
High-Coated Fine Sand	hF
Uncoated Medium Sand	uM
Low-Coated Medium Sand	lM
High-Coated Medium Sand	hM
Uncoated Coarse Sand	uC
Low Coated Coarse Sand	lC
High-Coated Coarse Sand	hC

2.4.2 Experimental procedures

Two sets of NMR experiments, a static saturation experiment and a wetting experiment, were conducted on cylindrical columns (composed of Lexan; inner diameter 2.9 cm, inner height 11.7 cm, volume 77.3 cm^3) packed with sand according to the dry packing method outlined in Oliviera et al. (1996). Filter paper (11 μm) was placed at both the top and the bottom of the columns to ensure that sand did not escape during the experiment and that the bulk density, p_b remained constant. Prior to each NMR experiment, the column was weighed to determine the dry sand mass. An initial NMR measurement was used to quantify the background signal from the column and instrument prior to this study. This measured signal was subtracted from all NMR measurements in this study.

The static saturation experiment was used to evaluate the accuracy of S_{NMR} as a means of predicting S_W. Known volumes of water ranging from 0 to ~30 mL were added to the sand-packed columns to produce six saturation states (i.e., S_W = 0, ~0.1, ~0.2, ~0.5, ~0.6, and 1). One NMR measurement was made on columns packed with each of the nine sample materials at each value of S_W (54 measurements total).

In the wetting experiment, NMR measurements were made on sand packed columns under changing saturation. Deionized water was pumped into the base of the columns using a peristaltic pump with a flow rate of 50 μL/min. A valve at the top of the column was left open to prevent atmospheric gas from being trapped. NMR measurements were made at 20-minute intervals until saturation was reached. It was assumed that saturation was reached when A_0 remained constant (within a threshold of 0.1%) for a period of 120 minutes. For all columns saturation was reached within 10 hours.

2.4.3 NMR measurements and analysis

All NMR measurements were made using a 2 MHz Rock Core Analyzer (Magritek Ltd). For each measurement, the column was aligned in the center of the NMR instrument to ensure that the static magnetic field was homogeneous across the column. Each NMR dataset was collected using a CPMG pulse sequence with 50,000 echoes and t_E = 200 μs. Each echo was sampled with 32 points with a dwell time of 1 μs. All CPMG measurements were stacked 32 times; each stack was separated by a delay time of 10 s, resulting in measurement time of 10.7 mins. Based on the pump rate of 50 μL/min and

the measurement run time, we estimate the saturation of the experiments will vary by <4% during the acquisition of the measurement.

Prior to the inversion, each NMR dataset was subsampled to 5000 data points to improve the speed of the fitting algorithm. The subsampled dataset was fit using a non-negative least squares algorithm with second order Tikhonov regularization with 160 log-spaced values of T_{2i} ranging from 10^{-4} to 10^{1} s (Tikhonov, 1963; Whittall et al., 1991), which represents the likely range of times with which the observed NMR signal can relax. The regularization parameter, which determines the degree of smoothness, was chosen using the L-curve corner criteria such that both the model norm and the residual were minimized (Hansen and O'Leary, 1993).

2.4.4 Physical and NMR properties

The total iron concentration, [Fe], mean grain diameter, d_{mean}, and the specific surface area, S_s of the sands used in this study were previously characterized by Keating and Falzone (2013) and are only briefly discussed here (Table 2-2). All S_S values were measured with the BET method using N_2 as the adsorbate; the sample mass was chosen such that the total measured surface area for was >1 m^2. For samples with $S_S < 0.15$ m^2/g, the BET measurements were repeated using Kr as the adsorbate; these measurement were found to confirm the values of S_S measured with N_2. For all samples the variation in [Fe], determined spectrophotometrically using the ferrozine method, was small. [Fe] ranged from 0.07 ± 0.02% for sample uC, to 0.38 ± 0.05% for sample hF. For the medium and coarse sands the addition of hematite resulted in an increase in [Fe], as expected. For the

fine sands, uF and lF had the same [Fe] value, while [Fe] of hF was greater. The d_{mean} values for the uncoated sands, determined from laser diffraction particle size analysis, ranged from 129 μm for the fine sand to 733 μm for the coarse sand, indicating that the sand packs have a range of average pore diameters. The values of d_{mean} did not show a trend with [Fe] indicating that coating the surfaces of the sands with hematite did not result in a measurable increase in d_{mean}. While it may be expected that the hematite coating would increase d_{mean} slightly, the size of the hematite synthesized for this experiment was expected to be on the nanometer scale (Schwertmann and Cornell, 1991), and so any change was outside the measureable range of the instrument. S_s was higher for the coated samples for sands of a constant grain size indicating that S_S increased with [Fe]. For each sand pack p_b was calculated by normalizing the dry mass of the sand in the packed columns by the volume of the sample holder (Table 2-2). p_b ranged from 1.42 ± 0.06 g/cm^3 for uF to 1.565 ± 0.007 g/cm^3 for lC. There was no observable trend in p_b with d_{mean} or [Fe]. The small range in the p_b values indicate that there was only minor variability in the way the columns were packed and that the addition of hematite did not change p_b.

Table 2-2. Physical and chemical sample properties: bulk density, p_b, average grain diameter, d_{mean}, specific surface area, S_s, and iron concentration [Fe].

Particle Size	**Sample Name**	d_{mean} **(μm) †**	S_s **(m²/g) †**	**[Fe] (%wt.) †**	p_b **(g/cm³)**
Fine Sand	uF	129 ± 11	0.37 ± 0.01	0.18 ± 0.04	1.42 ± 0.06
	lF	139 ± 3	0.373 ± 0.003	0.18 ± 0.01	1.51 ± 0.02
	hF	135 ± 5	0.55 ± 0.02	0.38 ± 0.05	1.42 ± 0.02
Medium Sand	uM	235 ± 13	0.15 ± 0.01	0.08 ± 0.01	1.48 ± 0.02
	lM	238 ± 6	0.20 ± 0.02	0.09 ± 0.01	1.558 ± 0.007
	hM	256 ± 2	0.306 ± 0.009	0.20 ± 0.03	1.48 ± 0.03
Coarse Sand	uC	733 ± 16	0.080 ± 0.007	0.07 ± 0.02	1.56 ± 0.02
	lC	709 ± 33	0.120 ± 0.005	0.10 ± 0.02	1.565 ± 0.007
	hC	753 ± 14	0.224 ± 0.006	0.22 ± 0.05	1.53 ± 0.01

† Keating and Falzone (2013)

Keating and Falzone (2013) calculated the values of ρ_2 and κ for the sample materials used in this study (Table 2-3). The value of ρ_2 ranged from 2.34 ± 0.08 μm/s for the sample uC to 14.0 ± 0.6 μm/s for the sample hF. For the fine and medium samples, ρ_2 increased with [Fe]; however, for the coarse samples, hC had a smaller value of ρ_2 than lC despite having a larger value of [Fe]. The values of κ ranged from 0.06 to 0.29 and can be divided based on the criteria for fast diffusion suggested by Ryu (2009): samples that relax in the fast diffusion regime ($\kappa \leq 0.1$; uF, lF and uM) and samples that do not relax in the fast diffusion regime ($\kappa > 0.1$; hF, lM, hM, uC, lC and hC).

Table 2-3: NMR properties: surface relaxivity, ρ_2, and control parameter, κ.

Particle Size	Sample Name	ρ_2 (μm/s) †	κ †
Fine Sand	uF	3.20 ± 0.05	0.06
	lF	3.28 ± 0.05	0.07
	hF	14.0 ± 0.6	0.27
Medium Sand	uM	3.03 ± 0.05	0.1
	lM	7.1 ± 0.2	0.24
	hM	10.9 ± 0.5	0.4
Coarse Sand	uC	2.34 ± 0.08	0.25
	lC	2.82 ± 0.08	0.29
	hC	2.4 ± 0.2	0.27

† Keating and Falzone (2013)

2.5 Laboratory Results

2.5.1 NMR response of saturated samples

We start by considering the NMR response of the saturated samples. The saturated distributions from one column of each of the samples, obtained after saturation had been reached in the wetting experiment, are shown in Figure 2-1. Replicate columns showed similar distributions. For all saturated samples, the NMR response exhibited a multi-exponential decay of magnetization. The shapes of the T_2-distributions were consistent with the results in Keating and Falzone (2013). For all samples, the T_2-distributions displayed multiple peaks: one large peak centered at short relaxation times (10^{-2} s $\leq T_2 \leq 10^{0}$ s), which we refer to as the short peak, and one or more smaller peaks centered at longer relaxation times (10^{-3} s $\leq T_2 \leq 10^{-1}$ s), which we refer to as the long peaks. The location and width of the short and long peaks varied with both d_{mean} and [Fe]. For the uncoated samples, the shape of the T_2-distributions was similar for the sands of all

grain sizes with one narrow short peak and one separated long peak; however, the location of the center of the peaks shifted to shorter relaxation times for the samples with smaller grains. For samples with the same grain size, the short peak broadened and shifted to shorter relaxation times with increasing [Fe]. Additionally, for samples with the largest [Fe] the number of long peaks increased and merged with the short peak, such that they were unresolved. Also observed in some of the distributions was a small peak centered at a relaxation time of ~3 s; this peak, attributed to water that was present in the tubing and fitting at the bottom of the column, was removed from the distributions shown in Figure 2-1 and was not included in the relaxation time analysis.

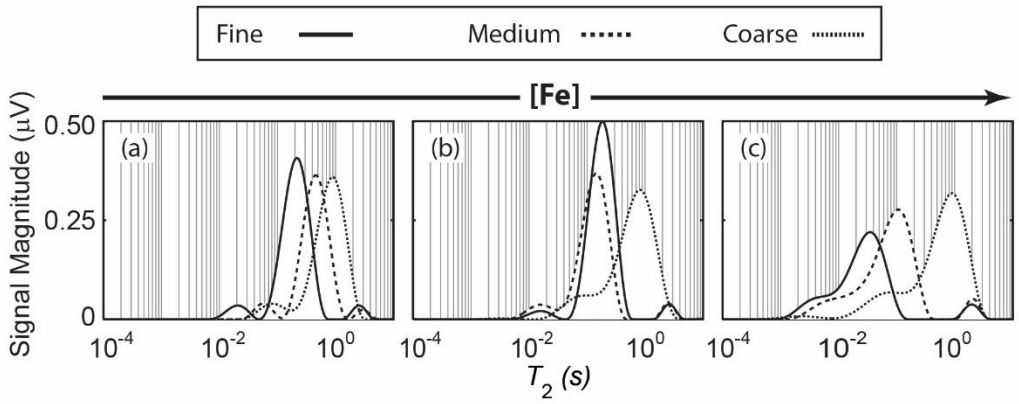

Figure 2-1. Saturated relaxation time distributions from one sample for each of the uncoated sands, uF, uM, and uC (a), the low-coated sands, lF, lM, and lC (b), and the high-coated sands, hF, hM, and hC (c).

The values of T_{2ML} for the saturated samples collected at the end of the wetting experiment are shown in Table 2-4. The mean and standard deviations of the saturated T_{2ML} values were obtained from three replicate samples in the saturated state at the end of

the wetting experiment. T_{2ML} varied over one order of magnitude and ranged from 0.026 ± 0.007 s for hF to 0.53 ± 0.07 s for uC. For the uncoated samples T_{2ML} increased with d_{mean}; for samples with the same grain size, T_{2ML} decreased with [Fe].

Table 2-4. NMR parameters of saturated samples: mean log relaxation time, T_{2ML}, and surface relaxation time, T_{2S}.

Particle Size	Sample Name	T_{2ML} (s)	T_{2S} (s)
Fine Sand	uF	0.16 ± 0.01	0.18 ± 0.02
	lF	0.133 ± 0.006	0.141 ± 0.007
	hF	0.026 ± 0.007	0.027 ± 0.007
Medium Sand	uM	0.34 ± 0.02	0.39 ± 0.03
	lM	0.090 ± 0.001	0.093 ± 0.001
	hM	0.060 ± 0.009	0.06 ± 0.01
Coarse Sand	uC	0.53 ± 0.07	0.7 ± 0.1
	lC	0.40 ± 0.02	0.47 ± 0.02
	hC	0.35 ± 0.01	0.40 ± 0.02

Repeated NMR measurements on samples of 50 mL of deionized water yielded a T_{2B} value of 2.64 ± 0.03 s; this value is similar to literature values for deionized water (Keating and Knight, 2010). T_{2B} of the effluent from each sand pack column during the wetting experiment was also measured. The average value of T_{2B} of all measurements was 2.60 ± 0.02 s; this was the value used in all further calculations.

T_{2S} was calculated from T_{2ML} and T_{2B} using equation 2-8; the value given is the mean of the three replicate samples the error is the standard deviation. The values of T_{2S} range from 0.027 ± 0.007 s for sample hF to 0.7 ± 0.1 s for sample uC. As with T_{2ML}, for the uncoated samples, T_{2S} increased with d_{mean} and, for samples with the same grain size, T_{2S} decreased with [Fe].

We note that while the diffusion relaxation time can influence NMR measurements, previous studies have shown that for the hematite used in this study there is no change in T_{2ML} associated with changing t_E (Keating and Knight, 2007; Keating and Falzone, 2013). We thus neglect the effect of the diffusion relaxation time in this study.

2.5.2 NMR response as a function of saturation

In this work, we assume that S_{NMR}, calculated from equation 2-9, is equivalent to S_W. To evaluate the accuracy of this assumption, we first compared S_{NMR} to S_W for the measurements collected during the static saturation experiment. The plot of S_W versus S_{NMR} is shown in Figure 2-2. As expected, the relation between S_W and S_{NMR} was well described by a line with a slope of 0.96 ± 0.01 and an intercept of 0.03 ± 0.02; the coefficient of determination for the linear relation was $R^2 = 0.99$. We conclude that S_W was accurately represented by S_{NMR}.

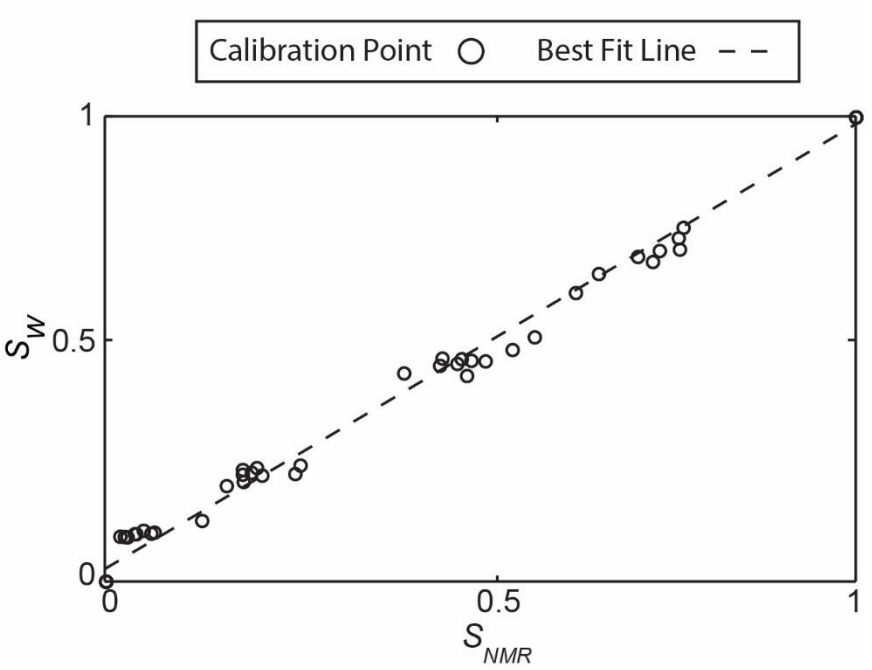

Figure 2-2. Gravimetrically determined saturation, S_w, versus NMR estimated saturation, S_{NMR}. Each data point is the mean determined from three repeated measurements. Errors are smaller than the size of data points. The dashed lines in the line of best fit with a slope of 0.96 ± 0.01 and y-intercept of 0.03 ± 0.02, and $R^2 = 0.99$.

As with the results from the saturated samples, the NMR data collected on the unsaturated samples during the wetting experiment displayed a multi-exponential decay of magnetization. The T_2-distributions at different values of S_{NMR} for one sample of each material type are shown in Figure 2-3. Data from replicate columns showed similar distributions and trends. The T_2-distributions shown when $S_{NMR} = 1$ in Figure 2-3 are the same as T_2-distributions shown in Figure 2-1. As with the saturated distributions, for all samples, the unsaturated T_2-distributions had two or more dominant peaks: one located between 10^{-2} s $\leq T_2 \leq 10^{0}$ s, referred to as the short peak, and one or more located between 10^{-4} s $\leq T_2 \leq 10^{-1}$ s, referred to as the long peaks. We also observed a small isolated peak centered at a relaxation time of ~3 s in some of the distributions. We again

attribute this peak to water located in the tubing and fittings of the sample holders and omit it from the plots shown in Figure 2-3 and for the calculation of T_{2ML}. We make the following observations that are consistent for all materials: (1) at low saturations (S_{NMR} < 0.1) the majority of the signal was in the long peaks, (2) at intermediate saturations (0.1 < S_{NMR} < 0.6) the contribution shifted from the long peaks to the short peak, and (3) at high saturations (S_{NMR} > 0.6) the majority of the signal was in the short peak.

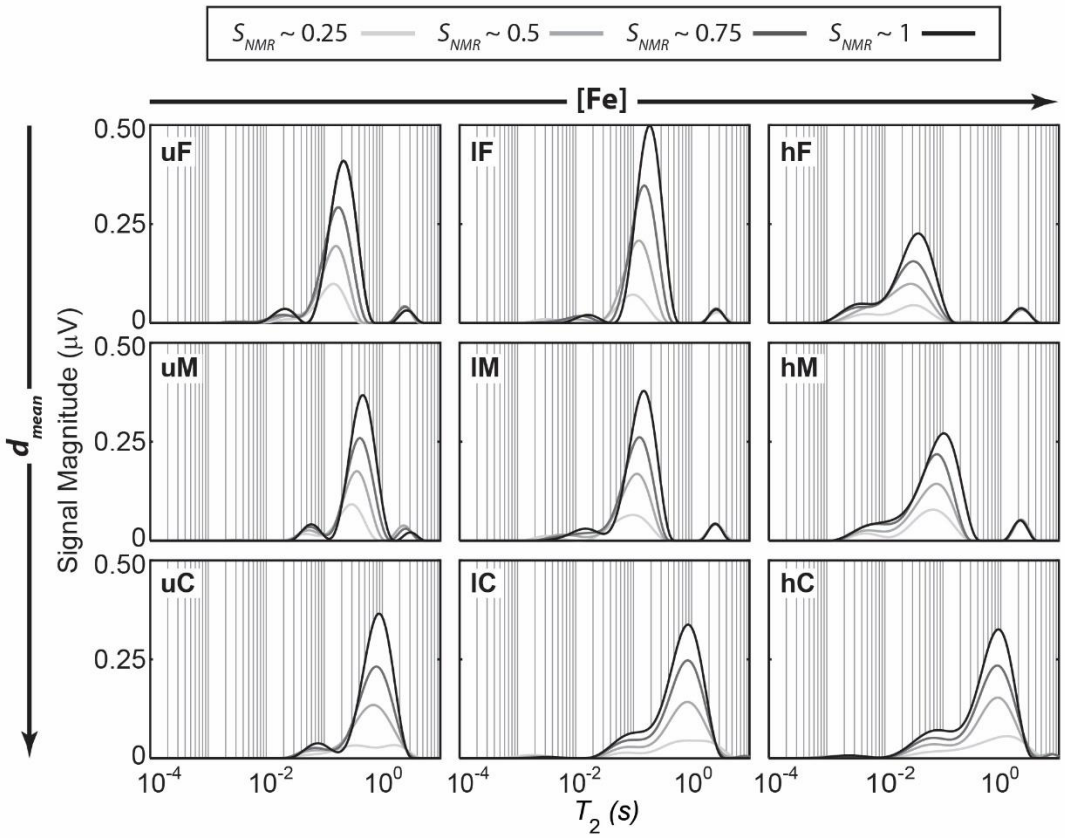

Figure 2-3. Relaxation time distributions versus NMR determined saturation, S_{NMR}, for one measurement of the uncoated, low, and high- coated fine sand (uF, lF, and hF), the uncoated, low, and high- coated medium sand (uM, lM, and hM), and the uncoated, low, and high- coated coarse sand (uC, lC, and hC). Measurements on replicate samples showed similar trends.

At each value of S_{NMR}, T_{2ML}, determined from the T_2-distribution, and T_{2B} were used to calculate T_{2S} from equation 2-8. In Figure 2-4 $T_{2S,Rel}$ was calculated from T_{2S} at each S_{NMR} divided by T_{2S} for the saturated samples and is plotted versus S_{NMR} for the three replicate samples from each sand type. Also shown in Figure 2-4 is the identity line (dashed gray line). The results of our study are consistent with other studies that show that $T_{2S,Rel}$ increases with S_{NMR} (Chen et al., 1994; Costabel, 2011; Costabel and Yaramanci, 2011b; Ioannidis et al., 2006; Mattea et al., 2004). Comparing the shapes of each of the graphs, we can see that the $T_{2S,Rel}$ versus S_{NMR} curves fall into two groups. The curves in which $T_{2S,Rel}$ increases linearly versus S_{NMR}, which includes samples uF, uM, lF, and lM, we refer to as group 1, while the curves in which there is a concave down relation between $T_{2S,Rel}$ and S_{NMR}, which includes samples hF, hM, uC, lC, and hC, we refer to as group 2. We note that the samples in each group can be classified by their associated value of κ: group 1 where $\kappa \leq 0.1$, group 2 where $\kappa > 0.1$.

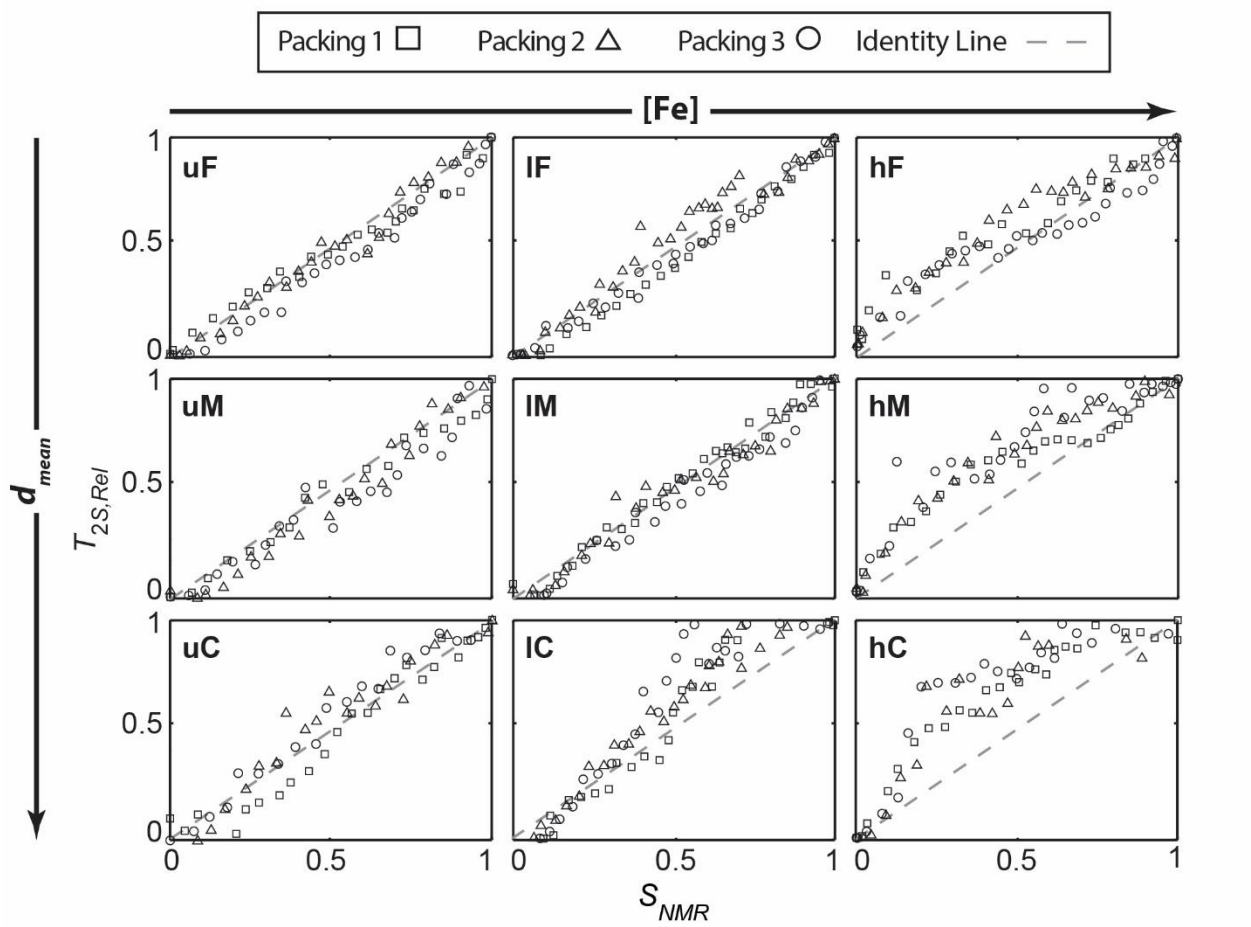

Figure 2-4. Relative surface relaxation, $T_{2S,Rel}$, versus NMR determined saturation, S_w, for the uncoated, low-, and high-coated fine sand (uF, lF, and hF), the uncoated, low-, and high-coated medium sand (uM, lM, and hM), and the uncoated, low-, and high-coated coarse sand (uC, lC, and hC).

2.6 Modeling NMR Relaxation in Unsaturated Porous Media

We next numerically simulate the NMR relaxation response as a function of S_w. We consider two simple theoretical pore-filling mechanisms: a thin film model, Figure 2-5(a) and a capillary tube model, Figure 2-6(a). We chose these pore-filling mechanisms because they are commonly used to explain flow in the vadose zone (see e.g., Koorevaar et al., 1983). In each model at a given value of S_w, the geometric distribution of water

within the pore space is different depending on the pore-filling mechanism and the NMR relaxation time can be calculated based on the water distribution.

2.6.1 The thin film model

The thin film model simulates water filling a single pore and assumes that in an unsaturated state the water exists as a thin film on the surface of the pore, the thickness, *th*, of which is governed by S_W, Figure 2-5(a) (Koorevaar et al., 1983). Costabel (2011) developed an analytical solution to model the NMR relaxation behavior of a thin film of water on a pore surface for a pore with an ideal shape (planar, cylindrical, or spherical). The solution follows Brownstein and Tarr (1979), which uses an eigenvalue approach to solve the Bloch-Torrey equations that govern NMR relaxation (Torrey, 1956), to predict the value of $T_{2S0,Rel}$ at a given value of S_w. As with the original Brownstein and Tarr solution, this model can be evaluated by changes in κ rather than individual variations in ρ_2 or *r*. The plot of $T_{2S0,Rel}$ versus S_w for a cylindrical pore with values of κ ranging from 0.01 to 10 are shown in Figure 2-5(b); similar results were found for planar and spherical pores. From Figure 2-5(b) we see that, for relaxation occurring in the fast diffusion regime (i.e., $\kappa \leq 0.1$), $T_{2S0,Rel}$ increases linearly with S_W; for relaxation occurring outside the fast diffusion regime (i.e., $\kappa > 0.1$), $T_{2S0,Rel}$ increases with S_W and is a concave up function. The predictions from the thin film model are consistent with the Brooks Corey parameterization of the $T_{2S0,Rel}$ versus S_W (equation 2-10) as described by Costabel and Yaramanci (2011b). However, while Costabel and Yaramanci predicted that the exponent λ depends on the degree of heterogeneity in the grain sizes, the thin film model is a single

pore model and shows that λ depends on the diffusion regime (i.e., the value of κ) alone. Furthermore, the solution to the thin film model predicts that λ will always be less than or equal to 1, which is inconsistent with the measurements where $\lambda > 1$ (e.g., Ioannidis et al., 2006).

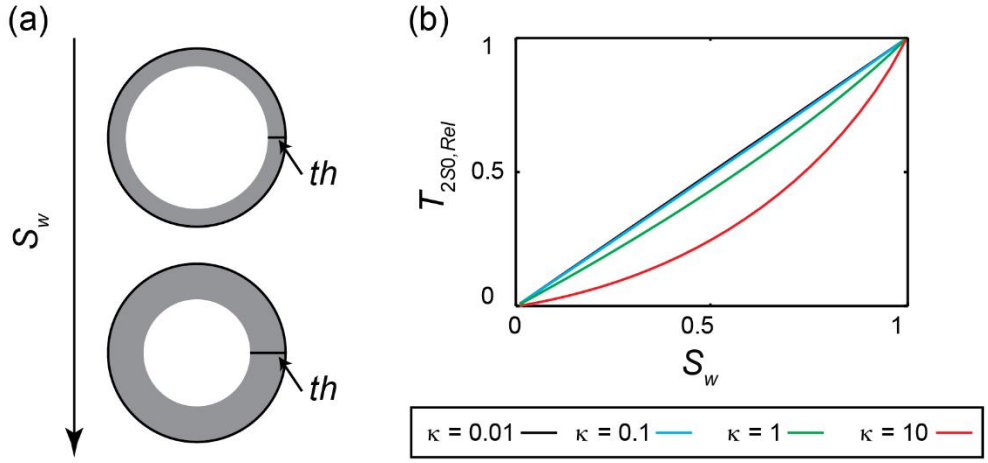

Figure 2-5. The pore-filling mechanism associated with the thin film model in a cylindrical pore for two saturation steps (a); indicated on the figure is the thickness, *th*, of the thin film for each saturation step. The predicted values of relative zeroth-mode relaxation time, $T_{2S0,Rel}$, versus saturation, S_w, for $\kappa = 0.01$ to 10 (b). The model was developed by Costabel (2011).

2.6.2 The capillary tube model

The capillary tube model (Figure 2-6(a); Brooks and Corey, 1964), as previously described, assumes that the pore space can be represented as a bundle of capillary tubes of different radii. In this model water is imbibed into a tube due to capillary suction; at a given suction there is a critical radius, r_c, such that all pores with radius $r \leq r_c$, are filled

while pores with $r > r_c$ are empty (Koorevaar et al., 1983). The value of S_w is determined from the volume of filled pores divided by the total pore volume. While equation 2-10, is also based on a capillary tube model, the model presented here differs in that it does not assume that T_{2ML} is proportional to r_c, but instead calculates the value T_{2ML} based on the filled pores at each saturation.

In the simulations for the capillary tube model, the pore-size distribution is represented by a log-normal distribution of pore radii characterized by a mean pore radius, r_{ML}, and a standard deviation, σ. We use values of r_{ML} ranging from 10 to 500 μm, to represent the range of pore-sizes expected in natural sands (sand grain sizes vary from 62.5 to 1000 μm; Koorevaar et al., 1983). We use values of σ ranging from 0.4, which represents a narrow PSD, to 1, which represents a broad PSD. We use values of ρ_2 ranging from 0.1 to 100 μm/s to be consistent with literature values for ρ_2, which range from 0.31 μm/s for very clean quartz sand up to 300 μm/s for sands coated with magnetite (Keating and Knight, 2008).

For each pore-size in the PSD, T_{2S0} was calculated using equation 2-3. T_{2S0} was then used to calculate T_{20} from equation 2-6 with T_{2B} = 2.6 s. For each value of r_c, T_{2ML} was calculated from the T_{20}-distribution of all pores with $r \leq r_c$ using equation 2-7, h_i was equal to the relative volume, determined from the PSD, of pores of that size. T_{2S} was then determined from equation 2-8 with T_{2B} = 2.6 s. S_W was calculated from the sum of the PSD for all pores with $r \leq r_c$. The relative value of T_{2S}, $T_{2S,Rel}$, i.e., T_{2S} at each saturation normalized by the saturated value of T_{2S}, is plotted versus saturation in Figure 2-6(b).

From the simulated NMR response of the capillary tube model, we see that the relation between $T_{2S,Rel}$ and S_W varies as a function of ρ_2, r_{ML}, and σ, and cannot be evaluated solely based on changes in κ as is the case in the thin film model. For narrow pore-size distributions, $T_{2S,Rel}$ is a concave down function of S_W, the shape of which could be described by equation 2-10 with $\lambda > 1$, as predicted by Costabel and Yaramanci (2011b). For the intermediate pore-size distributions, however, the shape of the curves is not consistent with the model discussed in Costabel and Yaramanci (2011b). When $\sigma = 1$ $T_{2S,Rel}$ is a concave up function of S_W, which can be described by equation 2-10 with $\lambda < 1$.

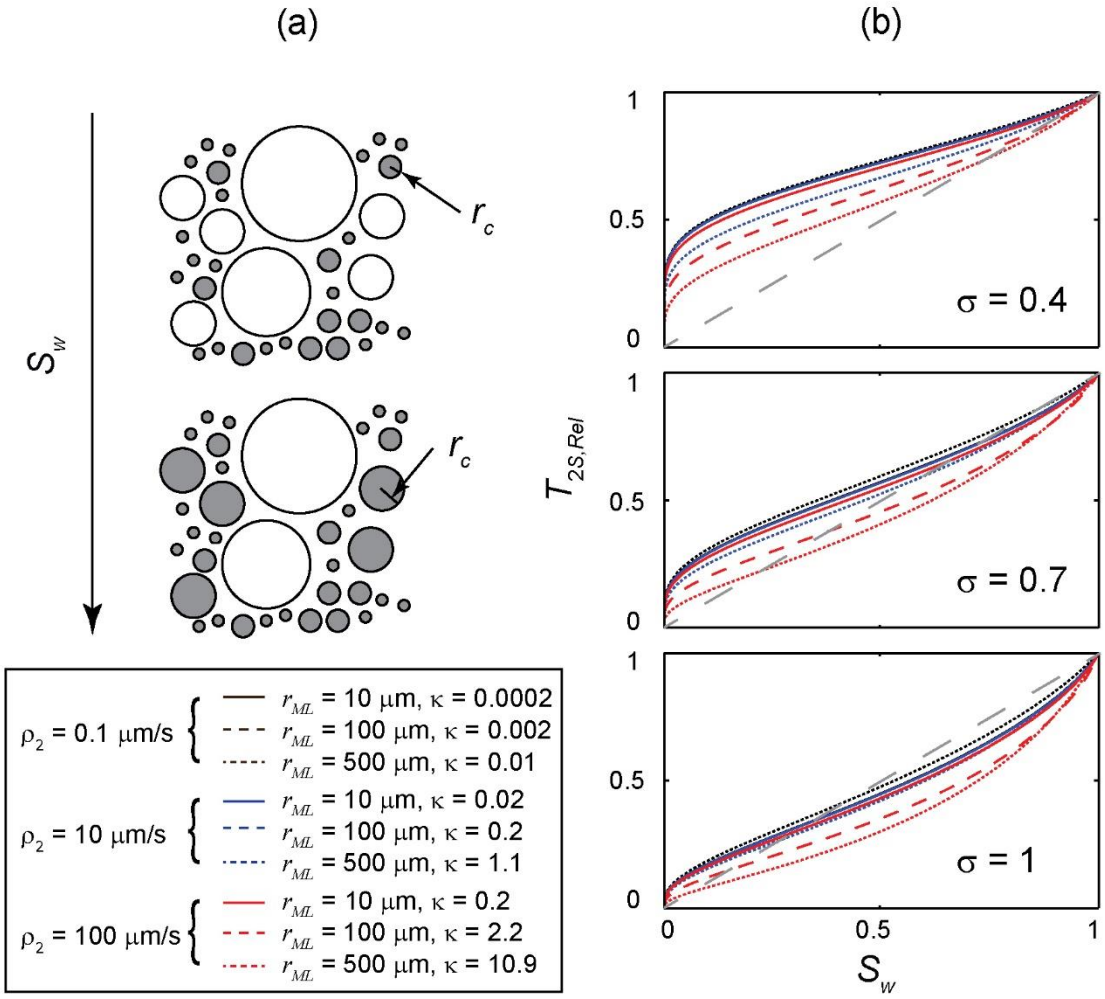

Figure 2-6. The pore-filling mechanism associated with the capillary model (a). The predicted change in relative surface relaxation time, $T_{2S,Rel}$, versus saturation, S_w, for log normally distributed cylindrical pores with average pore radius ranging from 10 to 500 μm, and standard deviations of 0.4, 0.7, and 1, and surface relaxivities ranging from 0.1 to 100 μm/s (b). Also shown in (b) is a grey dashed line representing 1:1 correspondence.

2.7 Discussion

The goal of this study was to understand the effect of pore-size and ρ_2, and consequently the effect of the diffusion regime in which relaxation occurs, on the relation between NMR relaxation time and water saturation. We first discuss the laboratory

results and characterize the $T_{2S,Rel}$ versus S_{NMR} curves by fitting the data using equation 2-10. We next compare the laboratory results to the results from the numerical simulations.

The curves relating $T_{2S,Rel}$ to S_{NMR} for the laboratory results (Figure 2-4) are consistent with the model presented by Costabel and Yaramanci (2011b) (equation 2-10). To quantify the $T_{2S,Rel}$ versus S_{NMR} relation, we fit each curve using equation 2-10 to determine a value for λ. The value of λ was calculated from a linear regression of log S_{NMR} versus log $T_{2S,Rel}$, with an intercept of log(1). To eliminate outliers, only values of $S_{NMR} > 0.1$ were used, which ensured that all data points had a high signal-to-noise ratio. The λ values ranged from 0.8 ± 0.1 to 2.3 ± 0.8 for all material types; the R^2 value was greater than 0.90 for all datasets. To understand the effect of different pore properties on the $T_{2S,Rel}$ versus S_{NMR} curve, we plot λ versus d_{mean}, ρ_2, and κ (Figure 2-7). In Figure 2-7, the data points are the mean and the error bars are the standard deviation determined from the three replicate samples.

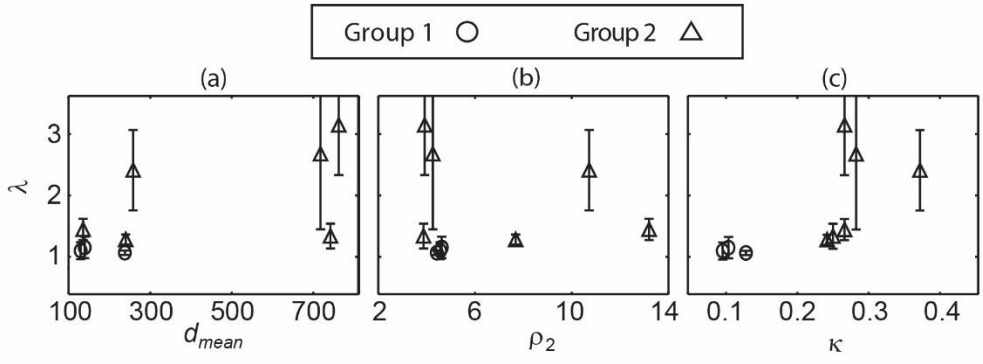

Figure 2-7. λ, the exponent in equation 2-10 versus mean grain size, d_{mean} (a), surface relaxivity, ρ_2 (b), and the control parameter, κ (c) for all samples. Data points and error bars represent the mean and standard deviations of predicted values of the exponent from three replicate wetting experiments.

From the plot of λ versus d_{mean}, Figure 2-7(a), and the plot of λ versus ρ_2, Figure 2-7(b), we see that λ does not show a strong correlation with d_{mean} or ρ_2. However, when we consider λ as a function of κ, Figure 2-7(c), we observe that κ shows a positive correlation to λ, although it is difficult to elaborate on the nature of this relation using this data. Specifically, λ is between 0.8 ± 0.1 and 1.0 ± 0.2 for group 1 samples where $\kappa \leq 0.1$ and λ increases from 1.2 ± 0.2 to 2.3 ± 0.8 for group 2 samples, where $\kappa > 0.1$. Contrary to the suggestion of Costabel and Yaramanci (2011b) that λ depends on the grain size homogeneity, the dependence of λ on κ suggests that this is not the case. In order to better understand how the pore-filling mechanism affects the relation between $T_{2S,Rel}$ and S_{NMR}, we next compare the laboratory results with the two numerical simulations.

The results from the laboratory experiments are not consistent with any of the numerical simulations based on the two pore-filling mechanisms. The laboratory results suggest that the relation between $T_{2S,Rel}$ and S_{NMR} (Figure 2-4) depends on the diffusion regime in which relaxation occurs and that for samples relaxing in the fast diffusion regime, $T_{2S,Rel}$ increases linearly with S_{NMR}. This behavior is confirmed by the thin film model (Figure 2-5) but is not confirmed with the capillary model, where the relation was not seen to depend on diffusion regime, and there were no circumstances under which $T_{2S,Rel}$ was found to increases linearly with S_{NMR}. In the laboratory data, for samples relaxing outside the fast diffusion regime, a concave down relation between $T_{2S,Rel}$ and S_{NMR} was observed; a curve of a similar shape was observed in the capillary model, but was not observed in the thin film model. While the results using the capillary model do not correspond to the experimental results, the exponent of the curves determined from

both the capillary model and the experimental results are positive for samples relaxing outside the fast diffusion regime.

One possible reason for differences between the numerical simulations and the experimental results is that the simple pore-filling mechanisms do not accurately describe the physical processes occurring during the imbibition of our samples. A more complex pore space than can be described with a simple pore-filling mechanism, such as a thin film or a bundle of cylindrical capillary tubes used here, could potentially explain the difference between the numerical simulations and the experimental results. For example, a recent study modeled the NMR response as a bundle of capillary tubes with triangular cross sections (Mohnke, 2014). While Mohnke, did not explicitly consider the relation between $T_{2S,Rel}$ and S_{NMR}, the plots of the T_2-distrbutions for different saturations provide evidence that a more complex geometric model could explain the behavior observed in our experimental data.

2.7 Conclusion

The laboratory and numerical results presented here provide insight into how variations in pore-size and surface relaxivity can affect the NMR relaxation time versus saturation relation. The data presented in this study demonstrates that the diffusion regime, the value of ρ_2 and the pore-size are all important factors in understanding the relation between $T_{2S,Rel}$ and S_{NMR}. The experimental results from this study confirmed that the shape of the $T_{2S,Rel}$ versus S_{NMR} curve depends on the diffusion regime in which relaxation occurs, which is determined from ρ_2 and the pore-size.

The numerical simulations based on two pore-filling mechanisms, the thin film and capillary models, were conducted in an attempt to explain the observed NMR relaxation behavior of the samples in this study. These models do not adequately explain the experimental results, indicating that these simple pore-filling mechanisms are inadequate to explain NMR relaxation behavior. Our study provides evidence that more complex geometrical models are necessary for explaining the observed $T_{2S,Rel}$ versus S_{NMR} curves for a wide range of samples. Additional research is thus needed to develop improved pore-filling mechanisms before an understanding of the effect of pore properties on the $T_{2S,Rel}$ versus S_{NMR} can be fully realized.

In order to use NMR measurements to characterize the water retention curve or to determine the matric potential in the vadose zone, we need to account for the effect of soil properties, including pore-size and surface relaxivity, on the NMR response of unsaturated soils. Although the results presented in this study provide a basis for interpreting NMR measurements in the vadose zone for sands with a range of pore-sizes and surface relaxivities, we believe that it also demonstrates the need to characterize a larger range of sediments, including silts and clays, with a wide range of mineralogy. Quantifying the effect of soil properties on the NMR response of unsaturated soils will improve our understanding of fundamental NMR behavior and ultimately enhance our ability to non-invasively characterize the vadose zone.

Chapter 3

The NMR Relaxation Response of Unconsolidated Sediments during Drainage and Imbibition[2]

3.1 Abstract

In this laboratory study, nuclear magnetic resonance relaxation data were collected on unconsolidated sediment to determine the NMR response, characterized by the transverse relaxation rate, T_{2ML}^{-1}, or the sum of echoes, SOE, during drainage and imbibition. Measurements were made on four synthetic sands, with a range of grain sizes and iron content, and two natural loamy sand soils. A porous plate apparatus was used to induce drainage and imbibition, and the water content, θ, was plotted as a function of the matric potential, ψ, to give the water retention curve (WRC). The drainage and imbibition branches of the WRC were then compared to the corresponding branches of the θ versus T_{2ML}^{-1} and the θ versus SOE curves.

Our results show that, even while hysteresis was observed between the drainage and imbibition branches of the WRC, no hysteresis was observed in the θ versus T_{2ML}^{-1} or SOE curves. However, we find that both T_{2ML}^{-1} and SOE varied as a function of θ. While these results demonstrate that it is not possible to distinguish drainage from imbibition using NMR measurements, the dependence of T_{2ML}^{-1} and SOE on θ suggests that it may

[2] Submitted for publication in *Vadose Zone Journal* as Falzone and Keating (2016c)

be possible to use them to characterize a single branch, or an average of the two branches of the WRC.

3.2 Introduction

Characterizing unsaturated flow within the vadose zone is critical for understanding soil processes, including the ability of a soil to store and release nutrients and contaminants. Physics-based models of unsaturated flow require an accurate understanding of the water retention curve (WRC), which relates the water content, θ, of a soil to the matric potential, ψ, across a range of conditions from oven dry to full saturation. While many methods have been developed that are capable of measuring θ in the field on the scale of centimeters (e.g., time domain reflectometry; Dahan et al., 2003) to meters (e.g., electrical resistivity tomography; Mawer et al., 2013), currently all available methods for determining ψ in the field are invasive (e.g., tensiometers; Whalley et al., 2013). In the laboratory, the WRC can be accurately determined using the porous plate method (Buckingham, 1907) by artificially varying ψ; however, such measurements are time consuming and require field samples to be available and transported to the laboratory, which can disrupt the sample's natural pore structure. A complicating factor in determining the WRC is that the curve exhibits hysteresis: the drainage branch of the WRC does not follow the same path as the imbibition branch of the WRC. There have been attempts to characterize the WRC with electrical resistivity measurements (Muñoz-Castelblanco et al., 2012), however, the sensitivity of these measurements to differences between drainage and imbibition remains. Electrical resistivity and induced polarization measurements were found to be sensitive to hysteresis in some studies (Ulrich and Slater, 2004; Hen-Jones et al., 2014), but not in others (Muñoz-Castelblanco et al., 2012). Of interest in our research is the use of the geophysical method nuclear magnetic resonance

(NMR) as a measurement for determining θ and ψ, during both drainage and imbibition, and consequently the WRC.

NMR relaxation measurements are used in geophysics to characterize porous media in the field, either with non-invasive surface instruments, such as surface NMR (Behroozmand et al., 2015), or minimally-invasive borehole instruments (Dlubac et al., 2013). Laboratory NMR measurements are used for pore size analysis (Keating and Falzone, 2013), and to examine theoretical relationships between NMR parameters and hydrological parameters, such as permeability (e.g., Timur, 1969; Weller et al., 2010). The signal from the NMR relaxation measurement is a multiple exponential decay and is inverted to yield an initial signal magnitude and a distribution of relaxation times, typically represented by a single relaxation time or rate. To avoid inverting the raw NMR data, the sum of the exponential decay can also be used to characterize the NMR relaxation behavior (Chen et al., 2000). Interest in using NMR for the hydrogeologic characterization of soils stems from the fact that the initial signal magnitude is proportional to the number of protons in water within the measured sample, and thus to θ. Another benefit of NMR measurements is that the relaxation rate is sensitive to the physical and chemical environment of protons within a pore space. In saturated media it has been shown that the relaxation time distribution is proportional to the pore-size distribution (Mohnke and Yaramanci, 2008; Keating and Falzone, 2013). While few studies have focused on the sum of echoes, it is also related to θ and the pore size distribution of the system (Chen et al., 2000). Because of the measurement's sensitivity to θ and pore size, NMR has been used to determine the depth to the water table (Müller-Petke et al., 2011a), and to estimate the saturated hydraulic conductivity in aquifers (e.g.

Knight et al., 2015). NMR has also been used to monitor infiltration during aquifer storage and recovery (Walsh et al., 2014) and multiple tools have recently been developed specifically for examining θ in the vadose zone (Sucre et al, 2011; Walsh et al., 2013a,b). In vadose zone applications the use of NMR has been limited to estimating θ, and information about pore sizes, available from the relaxation time distribution or the sum of echoes, has not yet been exploited.

Numerous studies have shown that the NMR relaxation time distribution is a function of θ (e.g., Bird and Preston, 2004; Ioannidis et al., 2006; Mohnke, 2014; Falzone and Keating, 2016a). Unlike in saturated systems, where the NMR response is a function of the pore size distribution of the measured sample, in unsaturated systems the NMR response is a function of the water-filled pore-space and thus is related to the water-filled pore size distribution. This relationship suggests that the plot of NMR relaxation rate versus θ can be used to parameterize the WRC, and studies have attempted to do so with varied success (Costabel and Yaramanci, 2011b; Costabel and Yaramanci, 2013; Costabel and Günther, 2014). The measurement's sensitivity to the water-filled pore size distribution suggests that it may be correlated with ψ and may be able to capture the hysteresis present in the WRC. A numerical study demonstrated that, for triangular pores, the NMR relaxation rate has different values at similar values of θ for the drainage and the imbibition branches of the WRC, and thus suggests that NMR relaxation measurements can capture differences in ψ during drainage and imbibition (Mohnke et al., 2015). In contrast, however, a laboratory study on synthetic silica gels found that the NMR relaxation measurements, made in a magnetic field with a strength ~10 times greater than those used for geophysical applications, did not exhibit hysteresis during

drainage and imbibition (Porion et al., 1998). In this study we aim to resolve the conflict present in the literature. We ask the question: what is the NMR response as a function of θ during drainage and imbibition of unconsolidated materials? We focus on measurements made at the ultra-low magnetic field strengths, relevant for geophysical NMR equipment. To the best of the authors' knowledge, no study has conclusively determined if the NMR response, for measurements made at ultra-low magnetic field strengths, shows differences during drainage and imbibition in unconsolidated sediments.

Measurements were made on four synthetic sands with a range of mean grain diameters, d_{mean}, which influences both the NMR measurement (Keating and Falzone, 2013) and the WRC (Nimmo, 1997), and a range of total iron content, influences the NMR measurement (Foley et al., 1996). Measurements were also made on two natural loamy sand soils, one with high total iron content and one with low total iron content. For all materials, the WRC, a curve relating θ to the NMR relaxation rate, and a curve relating θ to the sum of echoes were determined during drainage and imbibition. By comparing these curves, we can examine the NMR response as a function of θ and determine if NMR relaxation measurements are sensitive to hysteresis present in the WRC.

3.3 Background

3.3.1 Drainage/imbibition hysteresis of the water retention curve

The WRC describes changes in θ due to changes in ψ, and is characteristic of the pore-size distribution (PSD) of a soil. Pores will drain and fill with water at specific

values of ψ depending on their size. The value of ψ at which a pore will drain or fill, known as the air-entry value or ψ_c, is given by (Washburn, 1921),

$$\psi_c = -\frac{2\gamma_{ls}\cos\Phi}{r_c}, \tag{3-1}$$

where r_c is the maximum pore radius that is capable of being filled at ψ_c, γ_{ls} is the surface tension of the liquid-air interface, and Φ is the contact angle between the saturating fluid and the pore surface. Both γ_{ls} and Φ result from the cohesion between the saturating fluid and the solid matrix.

Characterizing the WRC is complicated by hysteresis; during drainage the WRC follows a separate path than during imbibition. Many complex conceptual models explain hysteresis (e.g. Miller and Miller, 1956; Mualem, 1974; Nimmo, 1992); however, the simplest way of describing this behavior is by considering the distribution of different size pores within a soil. During drainage, small pores block flow from larger pores and, consequently, larger pores remain saturated for values of ψ smaller than their corresponding ψ_c values. The blocked larger pores only drain when ψ_c of the smaller regulating pores is reached. During imbibition, larger pores block flow to smaller pores and, as a result, smaller pores remain empty for values of ψ greater than their corresponding ψ_c values. The blocked smaller pores only fill when ψ_c of the larger regulating pores is reached. The regulating effect of flow caused by small pores during drainage and large pores during imbibition leads to the observed hysteresis and a dependence of the WRC on the history of drainage and imbibition. This effect can lead to large uncertainty when trying to quantify the WRC in the field.

3.3.2 NMR theory

The NMR phenomenon occurs in atoms with unpaired protons or neutrons that possess a non-zero nuclear spin angular momentum, such as hydrogen with a nucleus consisting of a single proton (Callaghan, 2011). Protons in a static magnetic field align with and precess about the field at the Larmor frequency, which is proportional to the magnitude of the magnetic field. For geophysical measurements the Larmor frequency ranges from ~2 kHz, for surface-based measurements made in Earth's magnetic field, to 2 MHz for borehole instruments (Dunn et al., 2002; Legchenko et al., 2004; Walsh et al., 2008, 2013a,b; Behroozmand et al., 2015). The laboratory measurements made in this study were collected at 2 MHz. The NMR experiment begins when an energizing pulse, tuned to the Larmor frequency, tips the protons out of alignment with the static field. When the energizing pulse is stopped, the protons relax back to their equilibrium position; the return to equilibrium induces a measurable signal through induction. This study focuses on NMR data collected using the CPMG (Carr-Purcell-Meiboom-Gill) pulse sequence (Carr and Purcell, 1954; Meiboom and Gill, 1958), consisting of a 90^o pulse, followed by a series of 180^o pulses, separated by the echo spacing, t_E. The 180^o pulses reduce dephasing of the precessing protons that can occur when the static magnetic field is inhomogeneous. The resulting signal is the time, t, decaying transverse (or perpendicular) component of the total signal, $A_{XY}(t)$, measured at points half way between the 180^o pulses where the phases of the protons are maximally realigned (Callaghan, 2011).

In unconsolidated sediments $A_{XY}(t)$ is a multi-exponential decay,

$$A_{XY}(t) = \sum_i A_i e^{-t/T_{2i}}, \tag{3-2}$$

where A_i is the component of total signal magnitude relaxing with a relaxation time of T_{2i}, the inverse of the relaxation time T_{2i}^{-1} is the relaxation rate, and the sum is taken over all relaxation environment. The initial signal magnitude, $A_0 = \sum_i A_i$, is proportional to the volume of water in the measured sample and can be used to determine θ. A_i is often plotted versus T_{2i}, to give the relaxation time distribution, or T_2-distribution. In saturated porous media it is typically assumed that each T_{2i} value in the T_2-distribution corresponds to a different pore size, and the T_2-distribution represents the PSD. In partially saturated porous media, the distribution only represents the fraction of the PSD that is saturated at a given θ. In practice, a single relaxation rate is typically used to characterize the T_2-distribution; here we use the mean log relaxation rate, T_{2ML}^{-1}, determined from the inverse of the geometric mean of the T_2-distribution.

In porous media, relaxation occurs by three parallel process, surface relaxation, diffusion relaxation, and bulk fluid relaxation,

$$T_{2ML}^{-1} = T_{2S}^{-1} + T_{2D}^{-1} + T_{2B}^{-1}, \tag{3-3}$$

where T_{2S}^{-1} is the surface relaxation rate, T_{2D}^{-1} is the diffusion relaxation rate, and T_{2B}^{-1} is the bulk fluid relaxation rate. T_{2B}^{-1} can be determined from a CPMG measurement of the saturating fluid and is typically much less than T_{2S}^{-1}. It is generally assumed that the magnetic field is homogeneous and $T_{2D}^{-1} \sim 0$; this assumption can be tested by comparing CPMG measurements made at multiple values of t_E. If T_{2ML}^{-1} does not increase with t_E^2

then the assumption that T_{2D}^{-1} is insignificant is valid (Kleinberg and Horsfield, 1990; Keating and Knight, 2007). Assuming, $T_{2D}^{-1} \sim 0$ and $T_{2B}^{-1} << T_{2S}^{-1}$, then $T_{2ML}^{-1} \sim T_{2S}^{-1}$.

T_{2S}^{-1} is inversely proportional to the mean pore radius, r, and proportional to the pore surface-area-to-volume ratio, S/V (Brownstein and Tarr, 1979),

$$T_{2S}^{-1} = \rho_2 \frac{\alpha}{r} = \rho_2 \frac{S}{V}, \tag{3-4}$$

where ρ_2 is the surface relaxivity and α is the characteristic pore shape parameter (1 for planar, 2 for cylindrical, and 3 for spherical pores); S/V is equal to α/r. Equation 3-4 assumes that relaxation is surface limited, meaning that protons can travel to and sample the surface of the pore within the time scale of the experiment, which has been found to be true for most porous geological material (Latour et al., 1992; Kleinberg et al., 1994). When relaxation is not surface limited, T_{2S}^{-1} is influenced by the self-diffusion coefficient of the saturating fluid, and is a function of r^2 (Godefroy et al., 2001).

The sum-of-echoes (SOE), another parameter used for characterizing the NMR relaxation behavior with a single value, is the integral under the exponentially decaying signal and is related to both θ (from A_i) and the PSD (from T_{2i}) as shown by (Chen et al., 2000),

$$SOE = \int_0^\infty \sum_i A_i e^{-t/T_{2i}} = \sum_i A_i T_{2i} \propto \theta \sum_i \frac{A_i}{A_0} T_{2i}\,. \tag{3-5}$$

Using SOE has advantages over calculating T_{2ML}^{-1} in that it does not require inversion of the raw dataset, which can be strongly affected by the choice of regularization parameter SOE is also less sensitive to noise than the inversion. One disadvantage of using the SOE,

however, is that the response due to θ cannot be separated from the response due to the PSD.

3.4 Materials and Methods

To determine the NMR response of unconsolidated sediments during drainage and imbibition, we collected measurements on fine and coarse grain synthetic sands, and natural soils. Subsamples from the fine and coarse synthetic sands were coated with hematite to create samples with increased iron content as described in Keating and Falzone (2013). This process resulted in four synthetic sands: a fine-grain uncoated sand (uF), a fine-grain coated sand (cF), a coarse-grain uncoated sand (uC), and a coarse-grain coated sand (cC). The natural samples were two loamy sand soils collected from the Christina River Basin Critical Zone Observatory (CRB-CZO) at the Stroud Water Research Center in Southeastern Pennsylvania. One CRB-CZO soil (StL) is from an agricultural area with low total iron content; the other (StH) is from a forested area with high total iron content.

Values used for total iron content, d_{mean}, and S_s are from Keating and Falzone (2013) for the synthetic sands, and from data collected in this study for the CRB-CZO soils. The total iron (Fe(III) + Fe(II)) content was determined spectrophotometrically using the ferrozine method (Stookey, 1970). d_{mean} was determined from laser diffraction particle size analysis. S_S was determined with N_2 BET (Brunauer-Emmett-Teller) adsorption analysis, using a sample mass such that the total measured surface area was > 1 m^2. For samples with $S_S < 0.15$ m^2/g, the value of S_s was confirmed using Kr BET adsorption analysis.

3.4.1 Saturated sample preparation

To determine if $T_{2D}^{-1} \sim 0$, and to characterize the NMR properties of the samples, NMR data were first collected on saturated samples. For the synthetic sands, the data used were previously published in Keating and Falzone (2013). For the CRB-CZO soils, the data were collected for this study and follow the same procedure as was used for the synthetic sands. Sample material was first packed into a cylindrical Teflon sample holder (3.1 cm inner diameter, 5.6 cm inner height, 13.5 cm^3 inner volume) using a dry packing method (Oliviera et al., 1996). Each sample was vacuum saturated with deionized water using a vacuum of ~88 kPa. NMR measurements (described below) were made on three replicate samples for each material type.

3.4.2 Porous plate sample preparation and experiment description

For the porous plate experiment, sample material was dry packed (Oliviera et al., 1996) into Nylon sample holders (2.5 cm inner diameter, 2.5 cm inner height, 12.3 cm^3 inner volume) with one open side, to be placed in contact with the porous plate, and a port on the other side (diameter ~1 cm) to allow for air movement in and out of the sample. Three replicate samples were created from each material. Both ends were covered with 11 μm filter paper, fixed to the sample holder using room temperature vulcanizing silicone, to ensure consistent sample packing. Samples were vacuum saturated at ~88 kPa then weighed to determine the saturated mass. The bulk density, p_b, was determined by the dry sample mass and the volume of the sample holder. The

porosity, ϕ, was determined by subtracting the dry mass from the saturated mass and dividing by the volume of the sample holder.

In the porous plate apparatus (similar to that described in Buckingham, 1907) samples are placed on porous ceramic plate and suction is applied to a water reservoir beneath the plate. A porous ceramic plate with an air entry value rating of 50 kPa was used. Samples were fixed to the porous plate with a mixture of kaolinite clay and deionized water (1:1 by weight) to ensured hydraulic connectivity between the porous plate and samples. Contact between the porous plate and the water reservoir was maintained for the duration of the experiment. Suction was pulled using a vacuum pump on a two-chamber outflow reservoir connected to the water reservoir. One chamber was filled with desiccant to control evaporation; the other chamber was partially filled with deionized water. ψ was set using a vacuum regulator. The porous plate and samples were placed in a sealed canister with beakers full of deionized water to control the humidity. A port on the side of the chamber was left open to ensure the free flow of air into the sample columns.

Data for the drainage curve were collected first followed by data for the imbibition curve. To induce drainage ψ was decreased from -0.6 to -35 kPa; to induce imbibition ψ was increased from -35 to -0.5 kPa. Throughout the experiment, the mass of the outflow reservoir was measured every 5 s; the balance was set to auto-calibrate to control for drift in the mass readings. Once equilibrium was reached, i.e. the change of the outflow reservoir mass varied by $< \pm 0.01$ g for ≥ 4.5 hours, the samples were removed from the porous plate, weighed to determine θ, and the NMR datasets were collected.

3.4.3 NMR data collection and analysis

For each measurement, the sample was aligned in the center of the NMR instrument to ensure that the static magnetic field was homogeneous across the sample. All measurements were collected using the CPMG pulse sequence. Each echo was sampled using 32 data points. For the saturated samples data were collected with t_E = 200, 400, 600 and 800 μs; for the porous plate experiment data were collected with t_E = 200 μs. The delay time between stacks was set to three times the length of the data record. For the saturated samples, data were stacked 32 times and 50,000 echoes were collected for each stack. For the porous plate experiment, data were stacked until the signal-to-noise ratio was >100 (ranging from 8 to 800 stacks), and, in order to speed up the experiment, the number of echoes was chosen such that data record captured the full signal decay (ranging from 750 to 20,000 echoes).

Prior to inversion, each NMR dataset was subsampled to 5000 data points to improve the speed of the fitting algorithm; datasets with <5000 echoes were not subsampled. A non-negative least squares inversion algorithm with second order Tikhonov regularization (Tikhonov, 1963; Whittall et al., 1991) was used to fit the data with 160 log-spaced values of T_{2i} ranging from 10^{-4} to 10^{1} s as this represents the range of times with which the observed NMR signal can relax given the measurement constraints. The regularization parameter, which determines the degree of smoothness, was chosen using the L-curve corner criteria such that both the model norm and the residual norm were minimized (Hansen and O'Leary, 1993).

The NMR parameters were determined from the raw NMR data and the T_2-distribution. For each dataset, SOE was calculated from the sum of the raw signal. T_{2ML} was calculated from each T_2-distribution. T_{2ML}^{-1} is given by the inverse of T_{2ML}. The plot of T_{2ML}^{-1} versus t_E^2 was used to calculate T_{2D}^{-1} as described in Keating and Knight (2007). T_{2B}^{-1} was determined from three replicate measurements on samples of deionized water. T_{2S}^{-1} was calculated from T_{2ML}^{-1}, T_{2D}^{-1}, and T_{2B}^{-1} using equation 3-3, S/V was calculated from $S/V = S_s p_b/\phi$, and ρ_2 was calculated from T_{2S}^{-1} and S/V using equation 3-4.

3.5 Results

The physical and chemical properties of the materials used in this study are given in Table 3-1. The error values given in Table 3-1 are the standard deviations determined from measurements made on three replicate subsamples. For each of the synthetic sands the total iron content ranged from 0.07 ± 0.02% for uC to 0.38 ± 0.05% for cF, and the addition of hematite increased the total iron content. For the CRB-CZO soils the total iron content was 0.75 ± 0.04% for StL and 1.80 ± 0.09% for StH. For the synthetic sands d_{mean} varied from 129 ± 11 μm for uF to 753 ± 14 μm for cC. The values of d_{mean} of the synthetic sands did not show a trend with total iron content indicating that coating the surfaces of the sands with hematite did not result in a measurable increase in d_{mean}. For the CRB-CZO soils d_{mean} was 191 ± 23 μm for StL and 106 ± 13 μm for StH. For the synthetic sands S_S ranged from 0.080 ± 0.007 m^2/g for uC to 0.55 ± 0.02 m^2/g for cF; for the uncoated sands S_S decreased with d_{mean}. For synthetic sands of a given grain size (e.g.

uF and cF), S_S was higher for the coated sand. For the CRB-CZO soils S_S was larger than for the synthetic sands: 6.2 ± 0.1 m^2/g for StL and 18.3 ± 0.3 m^2/g for StH.

Table 3-1: Material Properties: total iron content, average grain diameter, d_{mean}, and specific surface area, S_s. Data for the fine and coarse sands are from Keating and Falzone, (2013). Data for the CRB-CZO soils were determined for this study. The errors given are the standard deviations from measurements on three replicate subsamples.

Full Name	**Abbreviated Name**	**Total Iron Content (%wt.)**	d_{mean} **(μm)**	S_s **(m^2/g)**
Uncoated fine sand†	uF	0.18 ± 0.04	129 ± 11	0.37 ± 0.01
Coated fine sand†	cF	0.38 ± 0.05	135 ± 5	0.55 ± 0.02
Uncoated coarse sand†	uC	0.07 ± 0.02	733 ± 16	0.080 ± 0.007
Coated coarse sand†	cC	0.22 ± 0.05	753 ± 14	0.224 ± 0.006
CRB-CZO: low iron	StL	0.75 ± 0.04	191 ± 23	6.2 ± 0.1
CRB-CZO: high iron	StH	1.80 ± 0.09	106 ± 13	18.3 ± 0.3

†, Data first presented in Keating and Falzone (2013)

The values of p_b and ϕ, calculated from the samples for the porous plate experiment are shown in Table 3-2. p_b ranged from 1.55 ± 0.02 g/cm^3 for StH to 1.66 ± 0.02 g/cm^3 for StL and ϕ ranged from 38 ± 1% for uC to 43.1 ± 0.3% for StH. The narrow range of p_b and ϕ indicated that there was minor variability in the packing of the samples.

Table 3-2: Properties of the samples used in the porous plate experiment: bulk density, p_b, and porosity, ϕ. The errors given are the standard deviations from measurements on three replicate subsamples.

Full Name	Abbreviated Name	p_b (g/cm^3)	ϕ (%)
Uncoated fine sand	uF	1.56 ± 0.05	42.2 ± 0.8
Coated fine sand	cF	1.59 ± 0.03	41.4 ± 0.3
Uncoated coarse sand	uC	1.62 ± 0.02	38 ± 1
Coated coarse sand	cC	1.61 ± 0.02	39 ± 1
CRB-CZO: low iron	StL	1.66 ± 0.02	40.1 ± 0.7
CRB-CZO: high iron	StH	1.55 ± 0.02	43.1 ± 0.3

The NMR parameters determined from the saturated samples, T_{2ML}^{-1}, T_{2D}^{-1}, T_{2S}^{-1}, and ρ_2, are shown in Table 3-3 and were calculated using the results from NMR measurements on deionized water which gave T_{2B}^{-1} = 0.383 ± 0.001 s^{-1}. This value for T_{2B}^{-1} is consistent with previous measurements on deionized water (Falzone and Keating, 2016a). T_{2ML}^{-1} showed no dependence on t_E^2 for all the synthetic sands or for StH indicating $T_{2D}^{-1} \sim 0$ for these samples. For StL, T_{2ML}^{-1} showed a small dependence on t_E^2; however, the value of T_{2ML}^{-1} (49 ± 2 s^{-1} at t_E = 200 μs) was greater than the value of T_{2D}^{-1} (0.5 ± 0.3 s^{-1} at t_E = 200 μs). Since for all samples T_{2ML}^{-1} is much greater than both T_{2B}^{-1} and T_{2D}^{-1}, surface relaxation was the dominant relaxation mechanism. The ρ_2 values ranged from 1.9 ± 0.6 μm/s for StL to 14.0 ± 0.6 μm/s for cF. Although across all materials, ρ_2 did not increase with total iron content, for a given group of materials (e.g., the synthetic sands), ρ_2 increased with total iron content.

Table 3-3: NMR Parameters: the mean log relaxation rate, T_{2ML}^{-1}, the diffusion relaxation rate, T_{2D}^{-1}, the peak surface relaxation rate, T_{2S}^{-1}, and the surface relaxivity, ρ_2, determined from the NMR measurements made on saturated samples. The errors given are the standard deviations from measurements on three replicate samples.

Full Name	**Abbreviated Name**	T_{2ML}^{-1} **(s^{-1})**	T_{2S}^{-1} **(s^{-1})**	T_{2D}^{-1} **(s^{-1})**	ρ_2 (μm/s)
Uncoated fine sand†	uF	6.25 ± 0.06	5.6 ± 0.1	~0	3.20 ± 0.05
Coated fine sand†	cF	38.5 ± 0.3	37.0 ± 0.3	~0	14.0 ± 0.6
Uncoated coarse sand†	uC	1.9 ± 0.1	1.4 ± 0.1	~0	2.34 ± 0.08
Coated coarse sand†	cC	2.86 ± 0.03	2.50 ± 0.05	~0	2.4 ± 0.2
CRB-CZO: low iron	StL	49 ± 2	45.9 ± 0.3	0.5 ± 0.3	1.9 ± 0.6
CRB-CZO: high iron	StH	153.4 ± 0.2	150.8 ± 0.2	~0	2.35 ± 0.07

†, Data first presented in Keating and Falzone (2013)

The WRCs are shown in Figure 3-1. Hysteresis was observed in all of the WRCs. As expected, the shape of the drainage and imbibition curves depended on the grain size distribution, which we characterize with d_{mean}. Finer materials retained water at the smaller ψ than coarser materials. Furthermore, comparing curves for the uF and cF samples (Figure 3-1a) or the curves for the uC and cC samples (Figure 3-1b), we see that the shape of the WRC was not affected by the hematite coating. At the greatest ψ in the imbibition branch of the WRC, none of the samples reached their saturated θ values, most notably the coarse grain sands, where $\theta < 0.1$ at $\psi = -0.5$ kPa. This behavior is typical of coarse-grained material, as it is more difficult to saturate large pores under capillary flow.

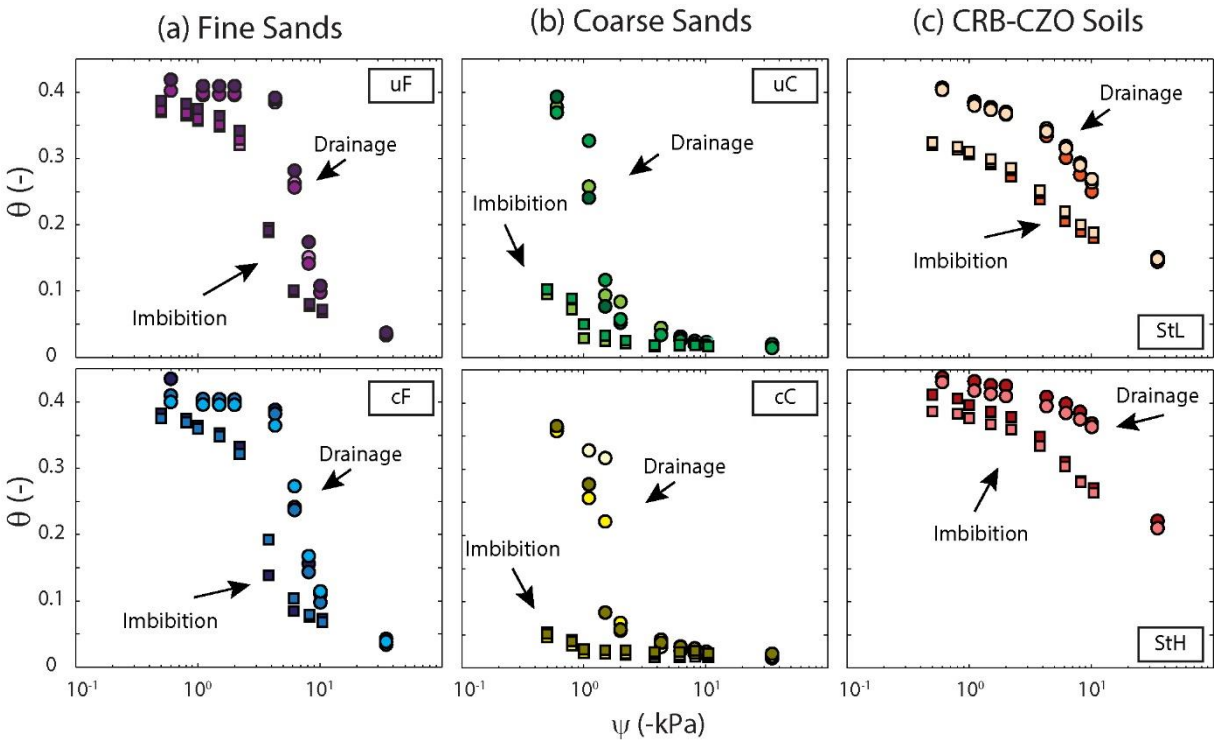

Figure 3-1: The water retention curve for the fine sands (a), the coarse sands (b), and CRB-CZO soils (c). The circles represent data collected during the drainage phase of the experiment; the squares represent data collected during the imbibition phase of the experiment. The colors represent the replicate samples for each material type.

A subset of T_2-distributions collected during drainage and imbibition, are shown in Figure 3-2 for the synthetic sands and Figure 3-3 for the CRB-CZO soils. The T_2-distributions varied as a function of θ. At high saturation, the shape and position of the T_2-distributions change depending on d_{mean} and ρ_2. Consistent with previous studies (e.g. Keating and Falzone, 2013), samples with smaller d_{mean} and/or larger ρ_2 have distributions centered at shorter relaxation times; samples with larger d_{mean} and/or smaller ρ_2 have distributions centered at longer relaxation times. Also consistent with previous studies, the location of the T_2-distribution shifted with saturation (Falzone and Keating, 2016a; Bird and Preston, 2004; Mohnke, 2014; Ioannidis et al., 2006). During drainage

(Figure 3-2a for the synthetic sands and Figure 3a for the CRB-CZO soils) the T_2-distributions shifted to shorter T_2 as θ decreased. During imbibition (Figure 3-2b for the synthetic sands and Figure 3-3b for the CRB-CZO soils) the T_2-distributions shift towards longer T_2 as θ increased.

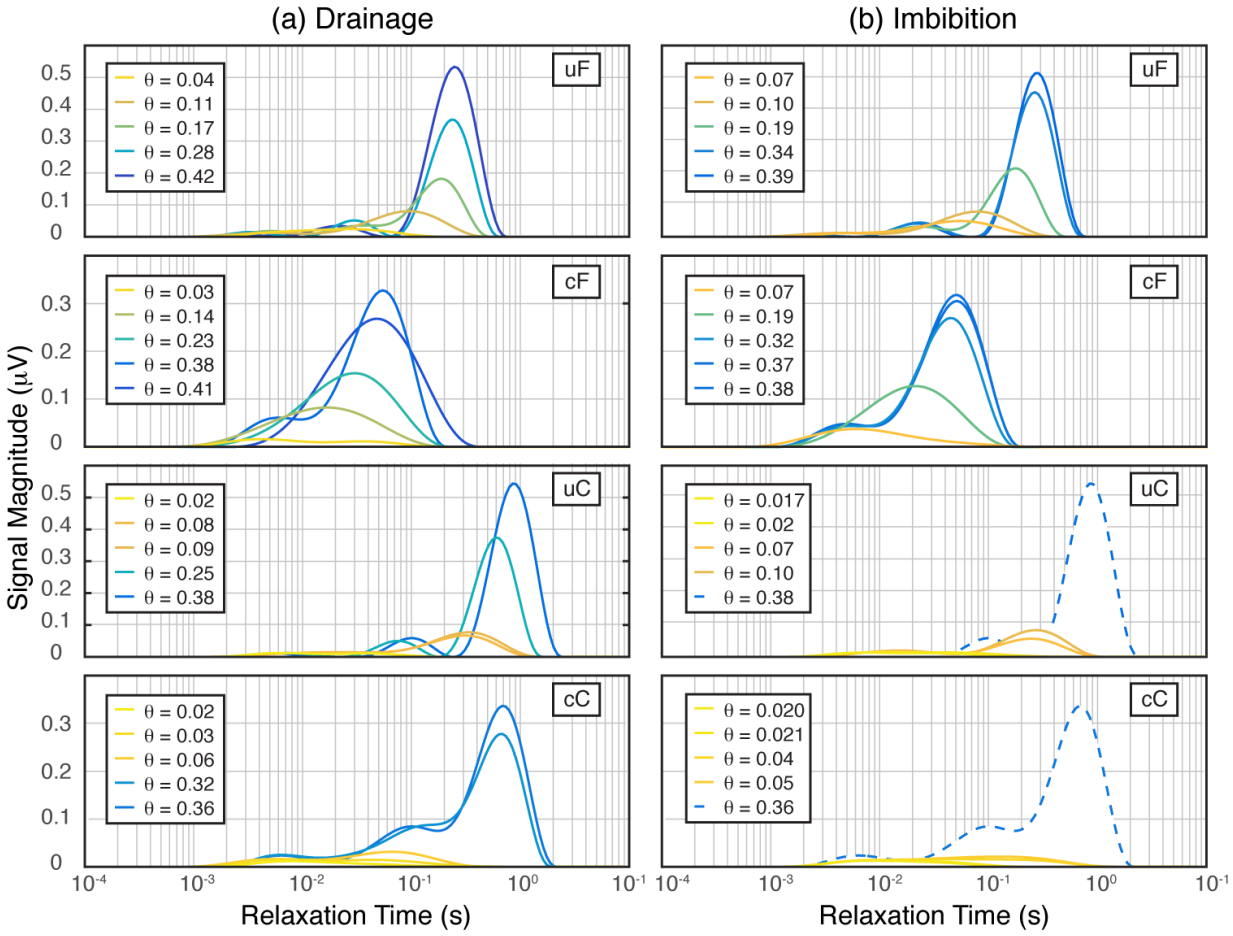

Figure 3-2: T_2-distributions determined from the data collected during drainage (a) and imbibition (b) for the synthetic sands. Data are shown for one sample from each material type; replicate samples exhibited similar behavior. Color of the curve represents the gravimetric water content values (as shown in the legend). The distributions with dashed lines in the uC and cC imbibition panels were from data collected for the drainage curve, and are shown for comparison.

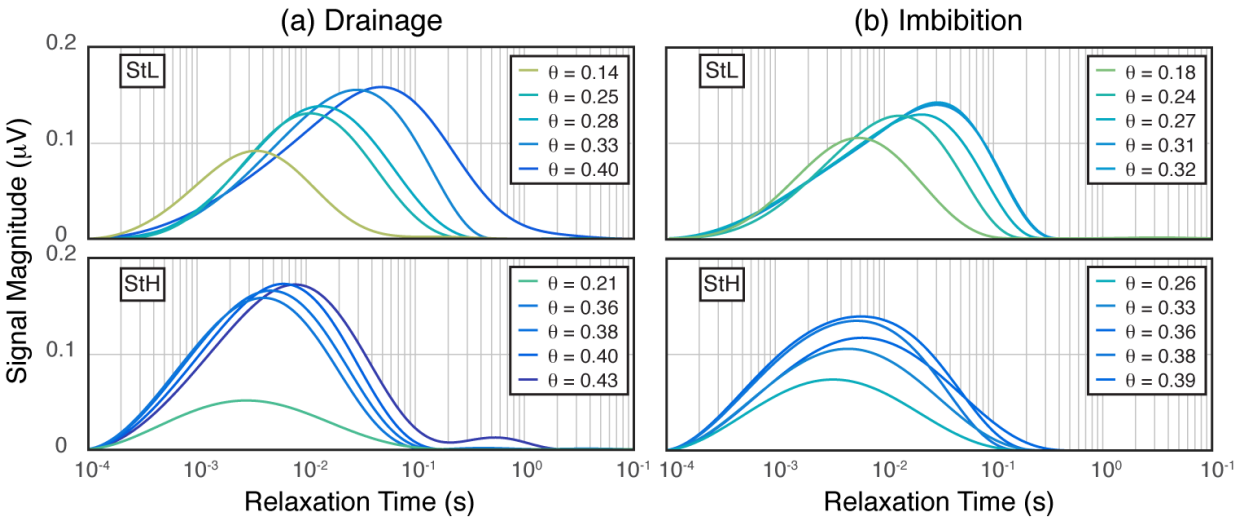

Figure 3-3: T_2-distributions determined from the data collected during drainage (a) and imbibition (b) for the CRB-CZO soils. Data are shown for one sample from each material type; replicate samples exhibited similar behavior. Color of the curve represents the gravimetric water content values (as shown in the legend).

A_0 shows a linear trend with θ (R^2 = 0.996; $p << 0.01$) for data collected during the drainage curve (Figure 3-4). Similar results were seen for data collected during the imbibition curves. While most of the data points fall along the line of best fit, there are a few outliers from measurements on the StH samples. We suspect that these outliers arise because, at lower saturations (< 0.3), some of the signal from these samples is relaxing faster than can be detected using t_E = 200 μs; this is consistent with the short relaxation times seen in the T_2-distributions for the StH samples.

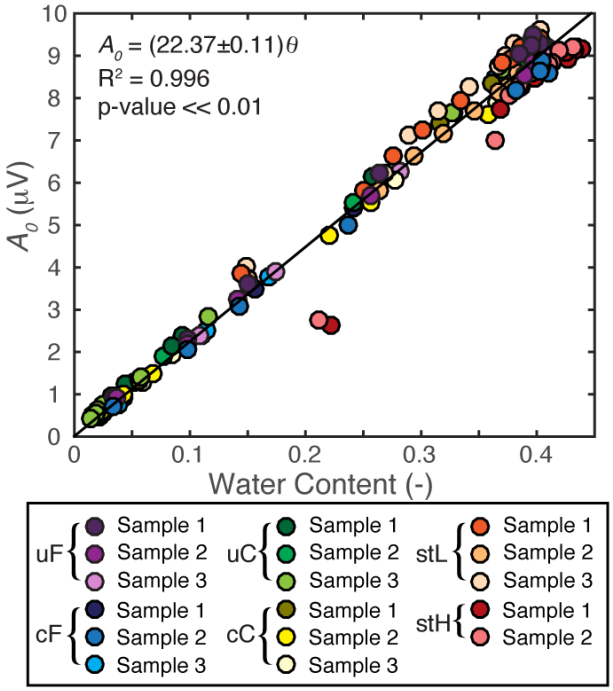

Figure 3-4: NMR initial signal magnitude (A_0) versus the water content. Data shown was collected during drainage.

The plot of θ versus T_{2ML}^{-1} shows that for all samples θ decreases with T_{2ML}^{-1} (Figure 3-5). There are two major observations we make from these plots (1) none of the θ-T_{2ML}^{-1} curves show hysteresis and (2) the position of the θ-T_{2ML}^{-1} curves are linked to d_{mean} and ρ_2. Notably, for samples uC and cC, with the largest d_{mean} and slowest saturated relaxation rates, the curve spans a large range of T_{2ML}^{-1} values (1.5 to 2 orders of magnitude). For the other samples the T_{2ML}^{-1} values span less than 1.5 orders of magnitude. Unlike the WRCs where the curves were only dependent on the grain size distribution, for the θ-T_{2ML}^{-1}, curves exhibited differences between samples with similar grain size distributions but different values of ρ_2 (compare the curves for uF and cF in Figure 3-5a, and for uC and cC in Figure 3-5b).

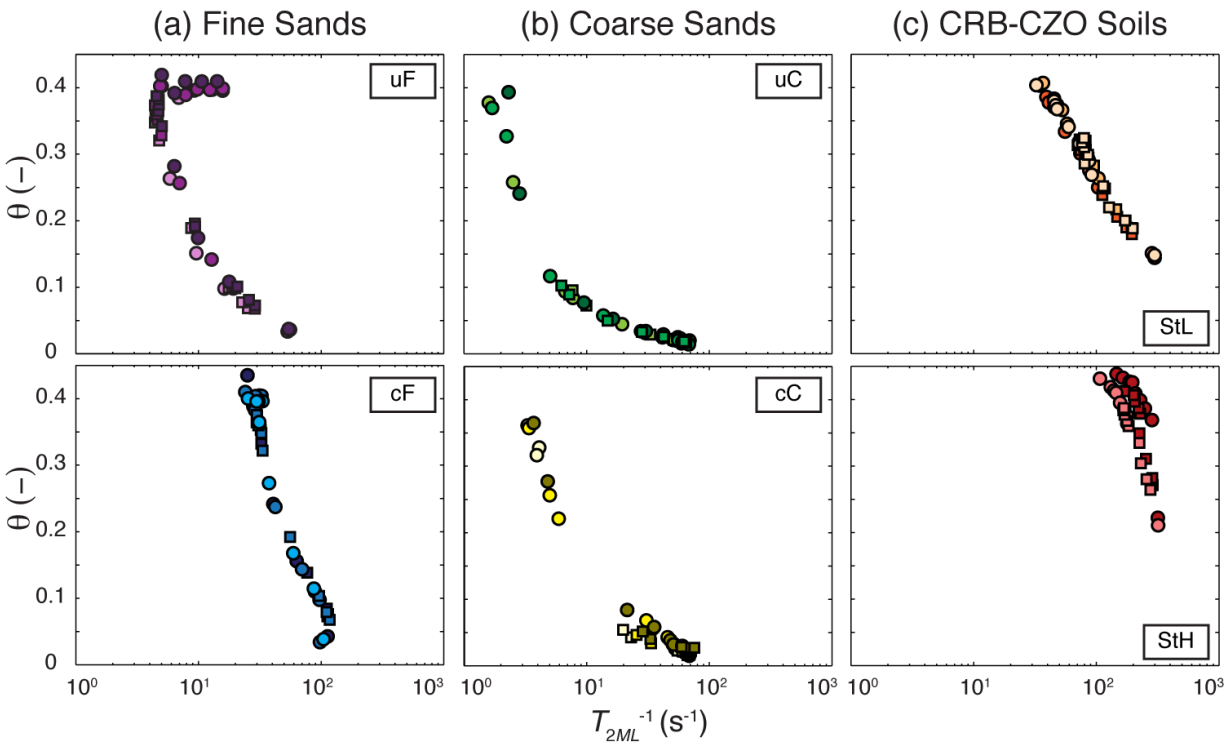

Figure 3-5: The mean log relaxation time, T_{2ML}^{-1}, versus water content, θ, curves for the fine sands (a), the coarse sands (b), and CRB-CZO soils (c). The circles represent data collected during the drainage phase of the experiment; the squares represent data collected during the imbibition phase of the experiment. The colors represent the replicate samples for each material type.

The plot of θ versus SOE shows that for all samples θ increases with SOE (Figure 3-6). We make the same observations for the θ-SOE curves that were seen in the θ-T_{2ML}^{-1} curves: (1) the θ-SOE curves do not exhibit hysteresis, and (2) the position of the θ-SOE curves depends on d_{mean} and ρ_2. Samples with the largest d_{mean} (uC and cC; Figure 3-6b) have SOE values that span 2.5 to 3 orders of magnitude, while samples with smaller d_{mean} and larger ρ_2 (uF and cF; Figure 3-6a; StL and StH; Figure 3-6c) span 1.5 to 2 orders of magnitude. As with the θ-T_{2ML}^{-1} curves there are differences between the θ-*SOE* curves

for samples with similar grain size distributions but different values of ρ_2 (compare the curves for uF and cF in Figure 3-6a, and the curves for uC and cC in Figure 3-6b).

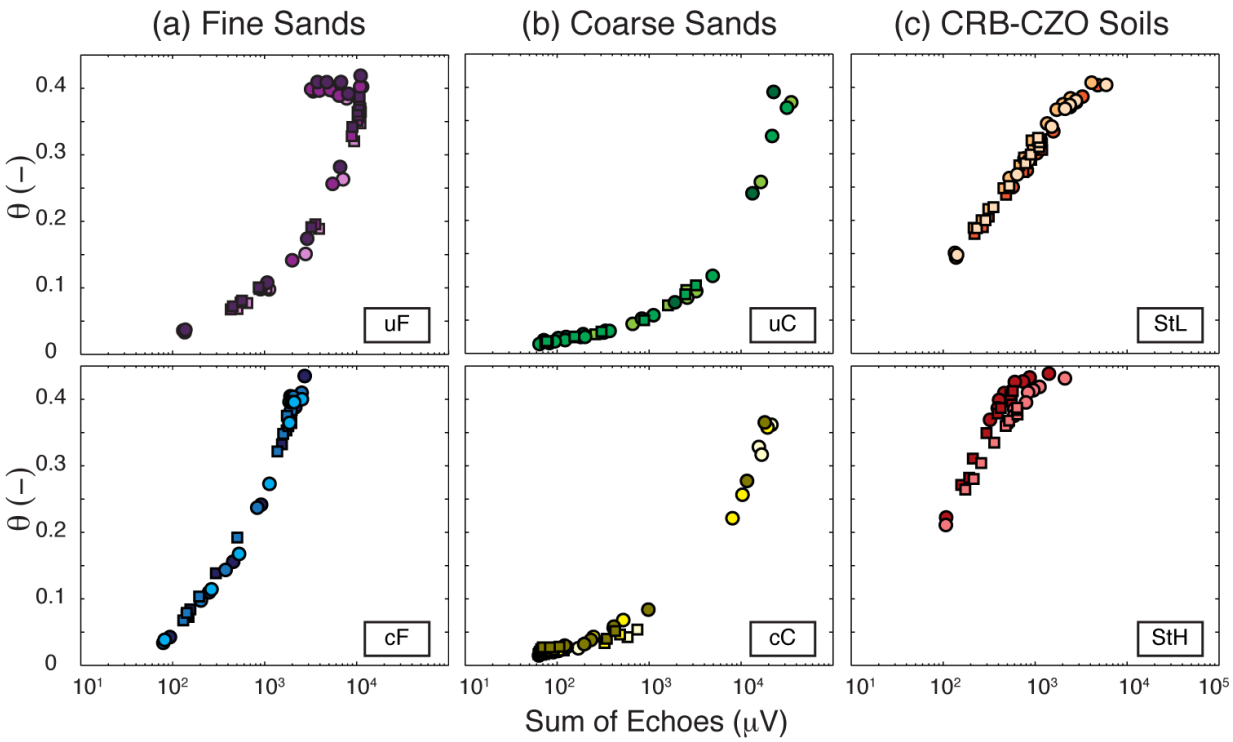

Figure 3-6: The sum-of-echoes, SOE, versus water content, θ, curves for the fine sands (a), the coarse sands (b), and CRB-CZO soils (c). The circles represent data collected during the drainage phase of the experiment; the squares represent data collected during the imbibition phase of the experiment. The colors represent the replicate samples for each material type.

The NMR response for the uF samples near saturation showed anomalous behavior. During drainage, when θ was close to saturation ($0.35 \leq \theta \leq 0.4$), corresponding to $0 \leq \psi \leq$ -15 kPa, we observed an order of magnitude shift in the location of the center of the T_2-distributions, an increase in the T_{2ML}^{-1} values, and a decrease in the SOE values (see uF panel in Figures 3-5a and 3-6a). This behavior was

observed in all replicate uF samples, but was not observed in the other samples in this study.

3.6 Discussion

Our study found that the θ-T_{2ML}^{-1} and θ-SOE curves do not exhibit hysteresis for unconsolidated sediments with a range of grain size distributions and ρ_2-values. Because the lack of hysteresis is evident in both curves, we conclude that this behavior is not due to the inversion approach or the choice of the regularization parameter used in the inversion algorithm. Furthermore, as the SOE values are very robust to noise and the signal-to-noise ratio for the NMR measurements were high (>100), these results are not due to noise in the data. From these results it is clear that numerical predictions of hysteresis in the NMR behavior as a function of θ (Mohnke et al., 2015), cannot be realized in experimental data. We conclude that the NMR measurement is not sensitive to the small-scale changes in the distribution of water within the pore space that occurs at similar θ but at different ψ during drainage and imbibition. As Porion et al. (1998) suggests, this is likely because the distribution of water in the pore space represents a similar average pore size during imbibition and drainage. NMR is not directly sensitive to forces exhibited on water in porous media, but rather to the size of the containing pores as is described in equation 3-4. It is important to understand how differences in α/r vary due to saturation during drainage and imbibition in order to interpret the measurement, however quantifying α/r at each step along the WRC is not possible.

The effect of α/r as a function of saturation on relaxation time can be explained by considering the hypothetical model presented in Figure 3-7, in which a sample with a layered/interconnected pore network is defined. Using a log-normal PSD defined by a mean pore size, r_{ML}, and standard deviation, σ, (Figure 3-7a), a layered soil sample can be constructed by randomly distributing different size pores within each layer (Figure 3-7b). The bottom layer is assumed to be in contact with a saturated porous plate. The degree of pore connectivity is also varied by defining the number of random connections between each pore of a layer to the underlying layer. Pore connectivity is defined as the percentage of pores on the underlying layer to which each pore in the overlying layer is randomly connected. The WRC can be determined for a range of ψ using equation 3-1, by assuming all pores with $r \geq r_c$ are capable of being emptied during drainage, and $r > r_c$ are capable of being filled during imbibition. In addition to this criterion, however, the saturation state only changes if a pathway to the porous plate is available, leading to hysteresis due the presence of regulating pores. We note that, unlike in real soils, the effect of trapped air and water within the pore space is not considered. This simplification predicts ideal behavior, in which the samples will obtain full saturation during imbibition and $\theta = 0$ during drainage. However, the effect of the physical pore network on hysteresis and α/r can still be evaluated. Values of α/r during drainage and imbibition can be calculated by considering the saturated pores at each value of ψ. In order to simulate cylindrical pores, α=2, but similar results were found when α=1 and 3 for planar and spherical pores respectively.

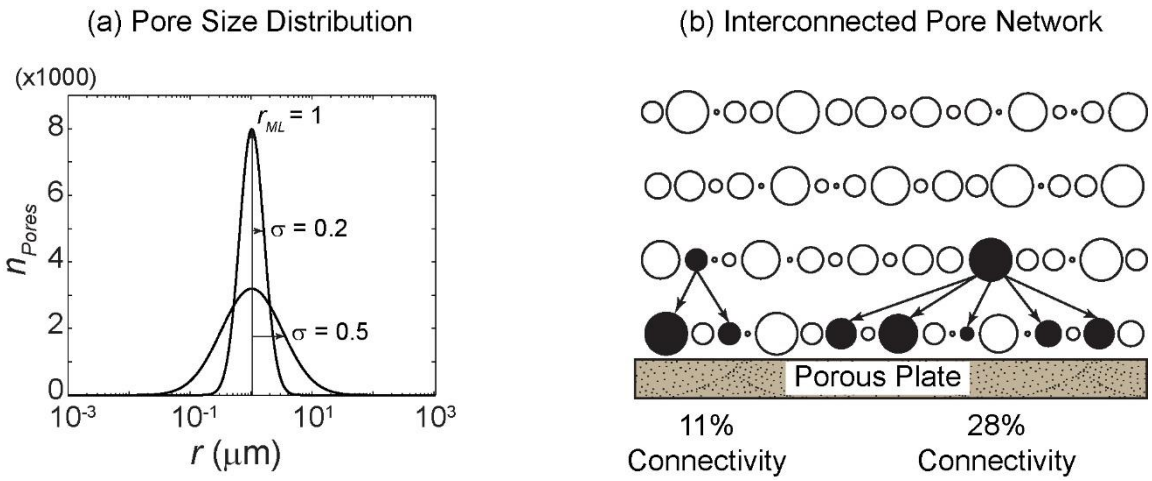

Figure 3-7: The interconnected 2D pore filling model in which layers of pores are randomly assembled and connected to one another. A pore size distribution (a) is randomly sampled to create a layered/interconnected pore network (b). The mean pore radius, r_{ML}, standard deviation, σ, and the degree of pore connectivity are defined in order to simulate drainage and imbibition.

Figure 3-8 shows the resulting WRCs from samples with $\sigma = 0.2$ and 0.5 (top and bottom rows respectively) and samples with increasing pore connectivity (2.5%, 10%, and 25%; a-c respectively). While the difference between the drainage and imbibition curves of the WRC increases with σ, this difference decreases as the pores become more connected. In Figure 3-9, θ versus α/r curves are calculated for the same model conditions shown in Figure 3-8. While hysteresis in the θ-α/r curves are evident for wide PSDs and low degrees of connectivity (e.g. Figure 3-9a, bottom row), the difference between drainage and imbibition curves is less than in the WRC. This difference decreases for narrow PSDs, and as the degree of connectivity increases. In certain cases, the difference between the θ-α/r curves during drainage and imbibition is indistinguishable (e.g. Figure 3-9c, top row).

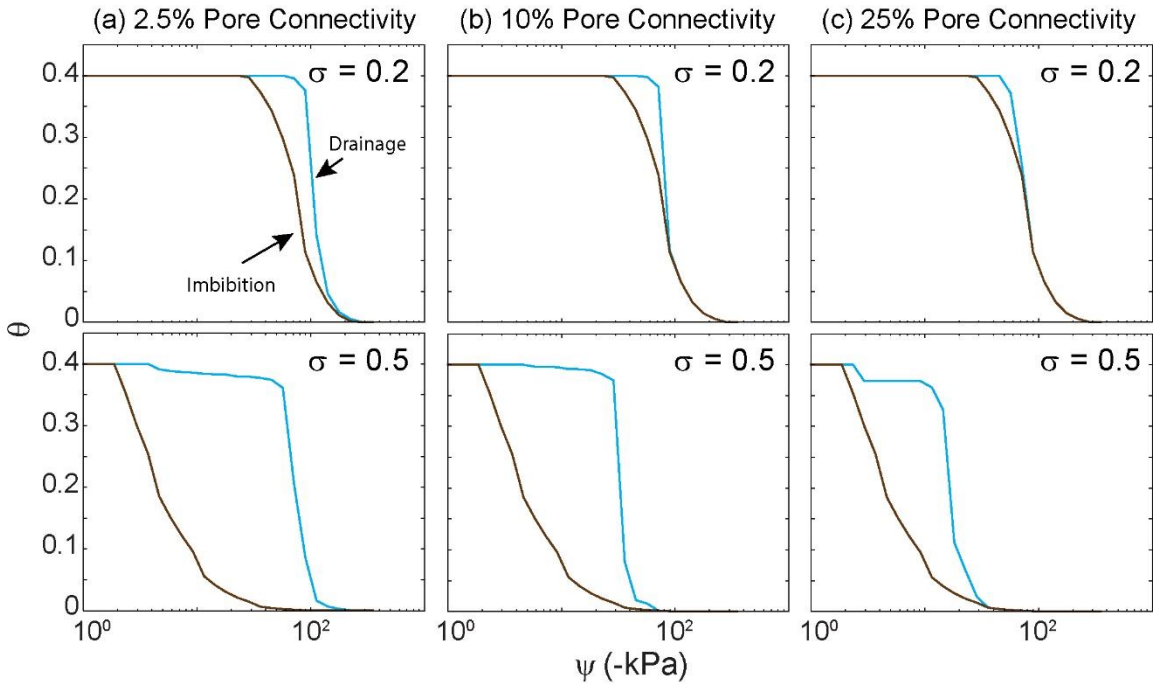

Figure 3-8: Water retention curves, WRC, during both drainage and imbibition predicted from the interconnected pore model presented in Figure 3-7, with pore size distributions characterized by a r_{ML}=1 μm and standard deviations of σ=0.2 (top row) and 0.5 (bottom row). Also shown are different degrees of interconnectivity between the pores: 2.5%, 10%, and 25% pore connectivity to the underlying layer (a, b, and c respectively).

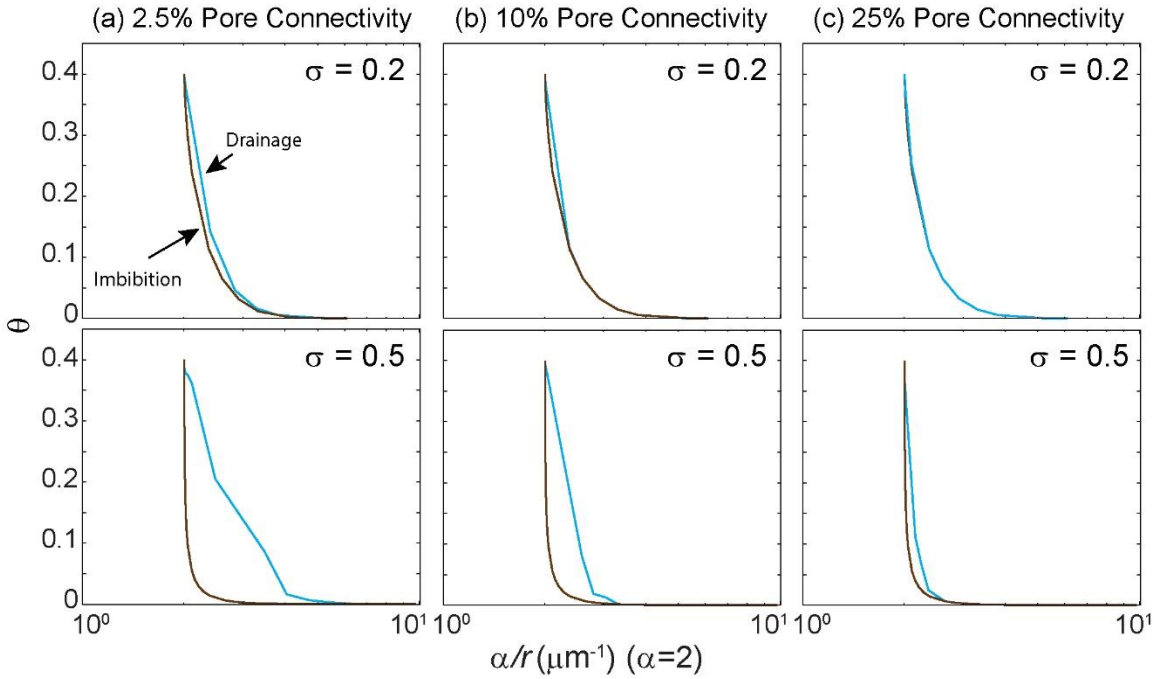

Figure 3-9: θ-α/r curves with α=2, during both drainage and imbibition predicted from the hypothetic model presented in Figure 3-7, with pore size distributions characterized by a r_{ML}=1 μm and standard deviations of σ=0.2 (top row) and 0.5 (bottom row). Also shown are different degrees of interconnectivity between the pores: 2.5%, 10%, and 25% pore connectivity to the underlying layer (a, b, and c respectively).

The predictions of the interconnected pore model indicate that NMR relaxation measurements are not capable of distinguishing between the drainage and imbibition curves of the WRC for soils that have a narrow PSDs and a high degrees of pore connectivity. A similar effect may explain why electrical geophysical measurements exhibited hysteresis in certain studies (Ulrich and Slater, 2004; Hen-Jones et al., 2014) but not in others (Muñoz-Castelblanco et al., 2012). r_{ML} was previously calculated to be 2.21 and 1.49 μm for the fine uncoated and coated sands respectively, and 9.1 and 3.5 μm for the coarse uncoated and coated sands respectively (Keating and Falzone, 2013). σ of the grain size distributions determined with LDPSA was calculated between 0.35 and 0.41 for all sands. These values predict the model of the wider distribution (bottom row;

Figure 3-8 and 3-9) is more representative of the synthetic sands in this study, indicating that similarities in the drainage and imbibition curves are due to pore connectivity as opposed to narrow values of σ.

Although the θ-T_{2ML}^{-1} and θ-SOE curves do not capture the hysteresis present in the WRCs, they do show differences depending on the grain size distribution of the material in the measured sample. This observation suggests that the θ-T_{2ML}^{-1} or θ-SOE curves could be correlated to a single branch or an average of the drainage and imbibition branches in the WRC. The model results presented in Figures 3-8 and 3-9 also indicates that considering the NMR relaxation time may provide some evidence into the connectivity of the pore network. However, in developing such a petrophysical relationship, care must be taken to account for a number of factors that affect the θ-T_{2ML}^{-1} and θ-SOE curves but not the WRC. In particular the effect of ρ_2, which influences the shape of the θ-T_{2ML}^{-1} and θ-SOE curves and the effect of a non-zero T_{2D}^{-1}, present in samples such as the StL soil.

3.7 Conclusion

The results from this study show that NMR relaxation measurements collected during both drainage and imbibition are not sensitive to hysteresis present in the water retention curve. This observation was consistent across measurements made on six samples: four synthetic sands and two natural soils that represent sediments with a range of grain size distributions and total iron contents. The lack of hysteresis in the θ versus T_{2ML}^{-1} and θ versus SOE curves indicates that NMR relaxation measurements are not

sensitive to difference in the distribution of pore water that occurs at similar ψ values for different branches in the water retention curve. These results can be explained by considering a hypothetical model of soils with log-normal pore size distributions and different interconnected pore spaces. As the standard deviation of the pore size distribution decreases, and the degree of interconnectivity of the pore space increases, the difference between the θ versus α/r curves during imbibition and drainage decreases. However, the dependence of T_{2ML}^{-1} and SOE on θ, as well as the effect of the grain size distribution on the relative positions of the θ versus T_{2ML}^{-1} or SOE curves, suggests that it may be possible to correlate these curves with the water retention curve. This study represents a significant step towards establishing this link and developing the petrophysical relationships necessary to exploit the full capabilities of the NMR measurements as a tool for characterizing the vadose zone.

Chapter 4

Algorithms for Removing Surface Water Signals from Surface NMR Infiltration Surveys[3]

4.1 Abstract

Surface nuclear magnetic resonance (surface NMR) is a geophysical method that directly detects water and can be used to determine the depth profile of water content within the subsurface. While surface NMR has proven useful for investigating groundwater in the saturated zone, its use to study the vadose zone is still in development. A recent study for the South Avra Valley Storage and Recovery Project (SAVSARP) demonstrated that surface NMR can be used to monitor infiltrating water associated with aquifer storage and recovery, a water resource management method in which surface water is stored in local aquifers during wet periods for use during dry periods. However, one of the major issues associated with using surface NMR to monitor infiltrating water is the influence of large bodies of surface water. In this study, we examine the effect that large bodies of surface water have on the surface NMR signal and propose three algorithms (the a priori, late-signal, and long-signal-inversion algorithm) to remove this signal. Using synthetic datasets, we assess the efficacy of each algorithm and determine that, while each algorithm is capable of suppressing the signal from a water layer with a thickness $\leq$ 5 m, the long-signal-inversion algorithm provides the most

[3] In review for publication in *Geophysics* as Falzone and Keating (2016b)

accurate and consistent results. Using a field example from the SAVSARP survey, we demonstrate the use of the long-signal-inversion algorithm to suppress the surface water signal. The results from this study show that the signal from surface water detected in a surface NMR survey can be suppressed to obtain the subsurface water content without the use of new measurements techniques or additional equipment.

4.2 Introduction

The practice of aquifer storage and recovery (ASR) is critical for water resource management in arid climates because it allows the storage of surface water in confined aquifers during wet periods for later use during dry periods (Fisher, 2013). A detailed understanding of aquifer recharge and regional groundwater flow patterns is essential for the successful storage of surface water in confined aquifers (Racz et al., 2012). Geophysical methods, including time domain reflectometry (Dahan et al., 2003), distributed temperature sensing (Constantz and Thomas, 1996; Blasch et al., 2002), gravity (Christiansen et al., 2011), and electrical resistivity (Mawer et al., 2013; Jayawickreme et al., 2010), are used to image aquifer recharge and to interpret groundwater flow patterns at the regional scale as well as the smaller local aquifer scale (these methods are reviewed in Ferré et al., 2007). While these commonly used geophysical methods can provide important information about aquifer recharge, they measure physical properties of the subsurface that are influenced by multiple factors, including grain size, sediment composition, and fluid conductivity, and are not uniquely sensitive to the parameter of interest, the subsurface water content. For example, in electrical resistivity measurements, low electrical resistivity is typically interpreted as higher water saturation (Archie, 1942), but it can also indicate high clay content or high fluid conductivity.

In contrast to more traditional geophysical methods, surface nuclear magnetic resonance (surface NMR) is directly sensitive to water and can be used to determine a 1D vertical distribution of water content in the subsurface. Furthermore, in saturated porous media, nuclear magnetic resonance (NMR) relaxation times have been correlated with the

pore diameter and used to predict the saturated hydraulic conductivity, (see Behroozmand et al., 2015, and references within). Walsh et al. (2014) presented the first study that showed that surface NMR can be used to monitor infiltration during ASR, and demonstrated the capability of surface NMR to both monitor a flood-induced wetting front and estimate the total amount of water recharged. However, as discussed in the study by Walsh et al., the interpretation of surface NMR data for ASR applications is complicated by two factors: (1) standard petrophysical NMR theory used to interpret surface NMR data assumes that the measured system is fully saturated, whereas in ASR the system can be in various states of saturation, (2) surface water present during infiltration can dominate the surface NMR signal making it difficult to characterize the infiltrating water in the subsurface. While there have been a number of recent publications focused on developing the petrophysical NMR theory to characterize variably saturated porous media in the vadose zone (Costabel and Günther, 2014; Costabel and Yaramanci, 2011b; Costabel and Yaramanci, 2013; Falzone and Keating, 2016a), to the best of the authors' knowledge, no studies have been published focused on removing the effect of the surface water from surface NMR datasets.

Figure 4-1a shows an example inverted surface NMR dataset – the relaxation time, T_2^*, distribution with depth – affected by surface water from Walsh et al. (2014); the dataset was collected at the Southern Avra Valley Storage and Recovery Project (SAVSARP) site in Tucson, Arizona. The effect of the surface water signal is evident as a large signal between 0 and 5 m, with long relaxation times centered at ~800 ms; a smaller signal between 2 m and 10 m depth with a relaxation time centered at ~10 ms shows the subsurface water content. Figure 4-1b and c demonstrate results of two

experimental methods used to suppress the surface water signal (Walsh et al., 2014). In Figure 4-1b a mono-exponential fit was used to model the surface water signal and subtract it from the original dataset. In Figure 4-1c the signal measured in a nearby loop was used to characterize the surface water signal and subtract it from the original dataset. While both methods successfully reduce the large signal associated with the surface water, the resulting images have very different total water content and T_2^* distributions versus depth profiles, making it difficult to determine which better represents the subsurface. This example demonstrates the need to develop and test methods to remove the surface water signal from surface NMR datasets. In this study we build upon the results of Walsh et al. (2014) and develop and evaluate algorithms for suppressing the surface water signal measured in surface NMR datasets. We note that while surface NMR inversions may be capable of distinguishing between surface and subsurface water if a priori information, such as the volume of the surface water and the resistivity of the water layer, is available and accurate, this information is often unavailable or inaccurate.

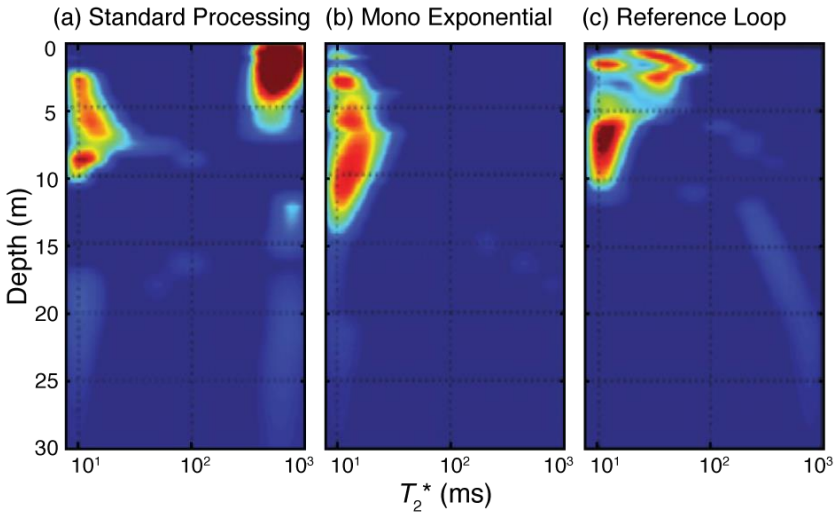

Figure 4-1. The March 29th dataset from the SAVSARP site, affected by a surface water layer, (a) compared to the results from two approaches for removing the surface water signal. In (b) a numerical approach was used to remove the surface water signal; in (c) the surface water signal was cancelled using the signal measured in a noise cancellation loop. Figure used with permission from Walsh et al. (2014).

Although ASR is the focus of our research, removing surface water from a surface NMR dataset is important for a range of applications. For example, in a recent study, surface NMR measurements were made on thermokarst lakes in a permafrost region located near Fairbanks, Alaska to characterize the unfrozen water content in the sediments below the lake (Parsekian et al., 2013). While the water content in the sediments below the lake was the signal of interest, the dominant signal in the dataset was the lake water. The authors mitigated the effect of the lake water using a blocky inversion and constraining for the known ice thickness, lake depth and the lake water content (100%). However, while the use of a blocky inversion provided information about the water content with depth, it only allows for a single relaxation time to represent the decay for each layer, limiting the relaxation time information obtained from the measurement. Furthermore, vadose zone studies may necessitate the use of a smooth inversion, since it

may require sensitivity to shifts in the relaxation time dependent on saturation (e.g., Falzone and Keating, 2016a).

In this study we focus on evaluating methods to remove the surface water that can be applied to standard surface NMR datasets (i.e., the stacked free induction decay, FID), and do not require the use of additional noise loops or new pulse sequences. These methods are applied to the stacked FID data prior to inverting the data, to allow for versatility in the choice of inversion algorithm. To test our hypothesis, that surface water suppression algorithms are capable of improving the interpretation of soil water in surface NMR datasets, we consider three numerical algorithms: (1) an a priori (AP) algorithm that uses a priori knowledge of the site to determine the surface water signal, (2) a late-signal (LS) algorithm that uses the signal recorded late in the measurement to determine the surface water signal, and (3) a long-signal-inversion (LSI) algorithm that uses an initial multi-exponential inversion of the recorded signal to determine the surface water signal. Using a synthetic dataset, we evaluate the efficacy of these algorithms and discuss the benefits and drawbacks of each. Finally, we test our algorithms using a surface NMR dataset collected during the ASR test at the SAVSARP site in Tucson, Arizona, presented in Figure 4-1 (Walsh et al., 2014).

4.3 Background and Theory

4.3.1 The surface NMR forward model

The surface NMR measurement relies on the NMR phenomena, in which atoms with unpaired protons or neutrons, when located in a static magnetic field with magnitude

B_0, will align with and precess about the magnetic field at the Larmor frequency, $f_0 = \frac{\gamma}{2\pi} B_0$. Here γ is the gyromagnetic ratio ($\frac{\gamma}{2\pi}$ = 42.576 MHz/T for protons in water). In the case of surface NMR, protons in water are the atoms of interest and B_0 is the magnitude of Earth's magnetic field at the survey site. To collect a surface NMR measurement a wire loop (typically 25 to 100 m in diameter) is laid out on the Earth's surface and used to transmit a radiofrequency electromagnetic pulse tuned to f_0. This energizing pulse, characterized by the pulse moment, q, which is equal to the magnitude of the applied current multiplied by the duration of the pulse, causes the proton spins to move out of alignment with Earth's magnetic field. Once the energizing pulse is removed, the spins return, or relax, back to their initial alignment with Earth's magnetic field. As they relax the spins induce an electromagnetic signal, typically measured in the same loop that was used to transmit the pulse, called the free induction decay (FID). In a typical surface NMR survey, each FID is stacked multiple times to improve the signal to noise ratio. The total surface NMR dataset, $A(q, t)$, collected at different pulse moments, results from protons relaxing at different depths, and, except in the presence of strong magnetic field inhomogeneities, is a multi-exponential decay.

For a 1D problem (i.e., a horizontally stratified Earth structure) $A(q, t)$ is,

$$A(q,t) = \int K(q,z) W(z, T_2^*) \int e^{-t(T_2^*)^{-1}} dT_2^* \, dz, \qquad (4\text{-}1)$$

where z is the vertical distance from the loop, t is time, T_2^* is the relaxation time, $W(z, T_2^*)$ is the distribution of water content with depth, and $K(q, z)$ is the kernel function (also called the sensitivity function) that describes how a change in the physical parameters at a point in the subsurface will change the surface NMR response. The kernel function is

affected by the resistivity structure of the subsurface, $\rho_s(z)$, the loop geometry, and Earth's magnetic field (both magnitude and direction) at the measurement location. Equation 4-1 is commonly used to develop synthetic surface NMR datasets to understand the surface NMR response from various groundwater scenarios, and to test new inversion algorithms (e.g., Parsekian et al., 2013). A detailed derivation of the surface NMR forward model can be found in Weichman et al. (2000).

4.3.2 Surface NMR inversion

While there are various surface NMR inversion algorithms available (see descriptions in Behroozmand et al., 2015), here we use the QT inversion as implemented in MRSmatlab (Müller-Petke and Yaramanci, 2010). The QT inversion algorithm uses the full surface NMR data cube in the inversion (i.e., the data collected at all pulse moments "Q" for the entire time series "T"). This approach can be used to obtain a smooth or blocky mono-exponential inversion, as well as a smooth multi-exponential inversion. For the purposes of this study we focus on the multi-exponential inversion of the amplitude of the complex NMR signal. By fitting a multi-exponential decay to the surface NMR signal in q versus t space, the data is inverted to obtain a model of the T_2^* distribution versus depth, and water content, θ, versus depth. Because the multi-exponential inverse problem is non-unique, a smoothing constraint, which is defined by the regularization parameter, is applied across both depth and T_2^*. The allowable range of values for depth, θ, and T_2^* can be defined by the user.

4.4 Surface Water Signal and Cancellation Algorithms

4.4.1 The effect of surface water on the forward model

Our research is concerned with removing the surface water signal from a surface NMR dataset that arises when an infiltration pond is used for ASR. We consider the scenario in which the loop is placed on the bottom of an infiltration pond. In this scenario, during infiltration, surface water is located above the transmitter/receiver loop and so depths both above and below the loop location (set to $z = 0$) must be considered. In this case equation 4-1 can be split into two parts:

$$A(q,t) = A_s(q,t)|_0^{\infty} + A_{SW}(q,t)|_{-z_{SW}}^{0}, \qquad (4\text{-}2)$$

where $A_s(q, t)$ is the signal originating from the subsurface, defined from $0 < z < \infty$ using the convention that z is positive below the loop with a resistivity structure of $\rho_s(z)$. $A_{SW}(q, t)$ is the signal originating from a z_{SW} thick surface water body, located from $-z_{SW} < z < 0$, with a resistivity of ρ_W. A third term accounting for the signal originating from the air above the surface water body is not included in equation 4-2 since the water content in air will be negligible. The kernel for this situation is more complex than the standard kernel used in the inversion of surface NMR data, as the energizing magnetic field must account for the resistivity structure both above and below the loop (Shope, 1982). Standard algorithms for inverting NMR data are not equipped to account for this type of survey geometry, and inverting NMR data without accounting for the resistivity of water layer may introduce additional uncertainty into the inversion results.

To understand the effect of the water layer on the energizing magnetic field and NMR response, we modeled the magnetic field using the approach outlined in Braun and

Yaramanci (2008) and Braun (2007). We compared the magnetic fields for three scenarios: a 35 m circular loop with no water above, a 35 m circular loop below a 5 m thick layer of water with ρ_W = 100 Ωm, and a 35 m circular loop below a 5 m thick layer of water with ρ_W = 1 Ωm. The magnetic fields were modeled using similar parameters used for the survey set up in Walsh et al. (2014): a total field strength of 47585 nT, corresponding to a Larmor frequency of 2026 Hz, and a subsurface resistivity structure of 32 Ωm from 0 to 5 m depth and 4 Ωm below 5 m depth. From the models we found that when comparing the 100 Ωm layer of water scenario to the no-water scenario, the magnetic field distributions were very similar. However, when comparing the 1 Ωm layer of water scenario to the no-water scenario, the magnetic field distributions were very different.

The effect of the water layer is highlighted when we compare the sounding curves (initial signal amplitude versus pulse moment) modeled using 100% subsurface water content for the three scenarios (Figure 4-2). No difference is discernable between the sounding curves when there is no water layer and when there is a 100 Ωm layer of water, however, there is a clear difference when the water layer resistivity is reduced to 1 Ωm. These results are consistent with the results of Braun and Yaramanci (2008), where it was shown that the kernel is strongly affected by subsurface structures with resistivities less than two times the loop diameter, which for a 35 m loop corresponds to 70 Ωm. Based on these results, we use 100 Ωm for the resistivity of the water layer in this study, which is within the range of the resistivity for groundwater (Telford et al., 1990), and note that if the water layer has a low resistivity (< two times the loop diameter) then the kernels used in the inversion algorithms will need to be adapted to account for the resistivity of the

water layer.

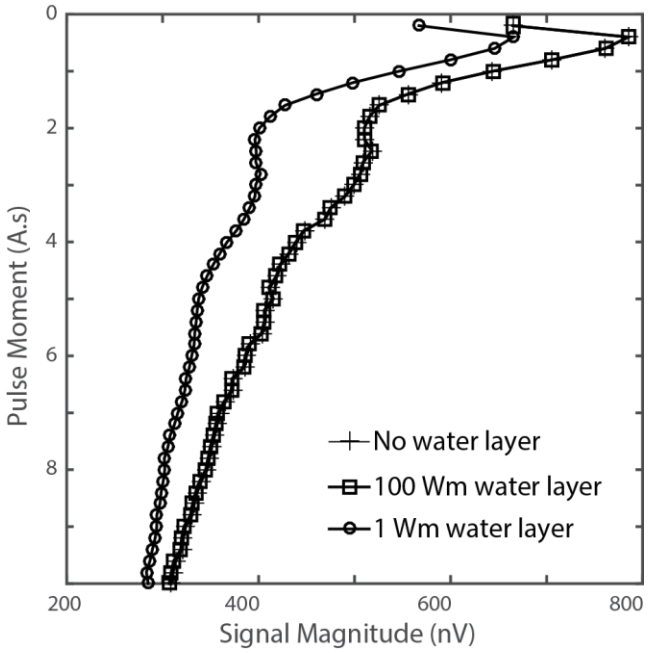

Figure 4-2. The modeled sounding curve resulting from a subsurface with 100% water content for three survey scenarios: a 35 m circular loop with no water above, a 35 m circular loop below a 5 m thick layer of water with ρ_W = 100 Ωm, and a 35 m circular loop below a 5 m thick layer of water with ρ_W = 1 Ωm. The signal was modeled using a total field strength of 47585 nT, corresponding to a Larmor frequency of 2026 Hz, and a subsurface resistivity structure of 32 Ωm from 0 to 5 m depth and 4 Ωm below 5 m depth.

There are a number of differences between the surface NMR signal from surface water, $A_{SW}(q, t)$, and the surface NMR signal from water in porous media, $A_S(q, t)$, that will help to differentiate the two signals. First, assuming no inhomogeneities in the static magnetic field, the signal from surface water is expected to be a mono-exponential decay, i.e., characterized by a single relaxation time, while the signal from water in porous media (the soil water) is expected to be a multi-exponential decay, characterized by a distribution of relaxation times (Mohnke and Yaramanci, 2005; Müller-Petke et al.,

2005). Second, the relaxation time associated with the surface water collected at Earth's magnetic field, T_{2SW}^*, is expected to be longer than the relaxation time associated with the soil water due to the fact that it is not affected by the surface relaxivity, or the ability of a pore surface to enhance relaxation (e.g. Müller et al., 2005; Legtchenko, 2013). T_{2SW}^* is given by (Grunewald and Knight, 2012),

$$T_{2SW}^{*-1} = T_{2B}^{-1} + T_{2H}^{-1}. \quad (4\text{-}3)$$

where T_{2B} is the bulk fluid relaxation time and T_{2H} is the relaxation that occurs due to dephasing in an inhomogeneous magnetic field. In a homogeneous field, T_{2SW}^* ranges from 600 to 1500 ms (Schirov et al., 1991), but could be shorter if the measurements are collected in an inhomogeneous magnetic field.

In contrast, T_2^* associated with water in sediments for measurements collected at Earth's magnetic field can be as long as 600 ms for gravel, but typically ranges from <30 ms for clayey sands to 180 ms for sands (Müller-Petke et al., 2005; Schirov et al., 1991). Furthermore, the relaxation time has been shown to decrease with decreasing saturation (Costabel and Günther, 2014; Falzone and Keating, 2016a), which will increase the contrast between surface water and soil water in partially saturated media. As such, the simplest way of removing surface water signal from the surface NMR dataset is to define a cutoff time, $T_{2SW,l}^*$, equal to the lower bound on the relaxation time expected for surface water, and remove the portion of the signal from the relaxation time distribution that has relaxation times greater than $T_{2SW,l}^*$ from each depth in the inverted surface NMR dataset. We call this approach the cutoff time (CT) approach. We note that if the difference between T_2^* of the groundwater and surface water is small or if the resulting

surface NMR dataset is primarily sensitive to surface water and not soil water, which is likely the case when surface water is present, then the CT approach will not work.

4.4.2 Suppressing the surface water signal

In this section we describe three algorithms for modeling the surface water signal, the a priori (AP) algorithm, the late-signal (LS) algorithm, and the long-signal-inversion (LSI) algorithm. In each of these algorithms, $A_{SW}(q, t)$ in equation 4-2 is modeled and then subtracted from the total signal, $A(q, t)$, to yield a modified surface NMR dataset that only contains the subsurface water content, $A_S(q, t)$. This process is applied to the stacked, noise cancelled, and demodulated FID, termed the "processed FID" here, for each pulse moment. Since these algorithms do not involve changes to the inversion algorithm, or changes in the way that the data are collected, they can be applied to a wide variety of surface NMR datasets and paired with any inversion scheme. We compare each of these approaches to the CT approach.

One concern in these approaches is the possibility that the surface water signal will be overestimated (i.e., the algorithm will "over-cancel" the signal), resulting in unrealistic negative values in the modified surface NMR dataset. Over-cancellation can occur if the modeled value of T_{2SW}^* is too fast or if the modeled initial signal amplitude, A_{0SW}, is too large. When necessary, the algorithms we have developed for modeling the surface water signal place constraints on the expected values of T_{2SW}^* and A_{0SW} in order to reduce the effects caused by over-cancelation. The approach used to constrain the value of A_{0SW} depends on the algorithm used.

4.4.2.1 A priori algorithm

In the AP algorithm a priori knowledge about the site (e.g., the depth of the surface water layer) is used to model the surface water signal and T_{2SW}^* is determined from an initial inversion of the entire uncorrected surface NMR dataset. T_{2SW}^* is assumed to be constant for all pulse moments. A forward model of a two-layer resistivity profile is used to model the surface water layer. The first layer has thickness z_{SW} and ρ_{SW} equal to the measured resistivity of the surface water or a value determined from the literature; the resistivity of the second layer, above z_{SW}, is near infinite ($1.28 \times 10^{14} - 3.9 \times 10^{14}$ Ωm, the resistivity for air; Pawar et al., 2009). A kernel is created with this resistivity structure, the survey layout, and the magnetic field (both magnitude and direction) at the measurement site and used to forward model the surface NMR response for each pulse moment. The modeled surface water signals are then subtracted from the processed FID for each pulse moment leaving the signal originating from the soil water. We note that this approach of separating the kernel of the water layer will work in environments with high resistivities (> two times the loop diameter, in this case greater than 70 Ωm); however, in low resistive environments a kernel will need to be calculated that accounts for the effect of the water layer on the energizing magnetic field.

Over-canceling the data for a single pulse moment can occur if the modeled surface water signal at time 0, $A_{SW}(q_i, t=0)$, is greater than the earliest measured signal in the processed FID, $A(q_i, t=0)$. If the signal in a given pulse moment is over-canceled, A_{0SW} is recalculated using a segment of the processed FID late in the data record. The time range for this segment of the processed FID should start late enough in the data record that the signal associated with the soil water has decayed, but the signal from the

surface water remains. The time range can be determined by considering the a priori value for T_{2SW}^*. For example, if the surface water signal has $T_{2SW}^* > 200$ ms and assuming that the soil water has $T_2^* < 200$ ms, then after 1000 ms the soil water will have decayed by more than 99%, and the surface water will dominate the signal. In this case, the time range can be set from $t = 1000$ ms until the end of the data record. The new value for A_{0SW} is then determined by fitting a mono-exponential decay with T_2^* set to T_{2SW}^* to the late-time segment of the processed FID.

4.4.2.2 Late signal algorithm

In the LS algorithm the surface water signal is modeled by fitting a mono-exponential decay to a segment of the processed FID at late times in the data record, determined as described above for the AP algorithm. Because the soil water is expected to decay much faster than the surface water, the segment can be selected so that only the surface water signal is present. The mono-exponential decay fit to the late-time interval is subtracted from the total signal to obtain the signal from the soil water. In this approach, which is similar to that presented in Walsh et al. (2014; Figure 4-1b), T_{2SW}^* is fit separately for each pulse moment, and so may vary for each processed FID. While there is a theoretical basis for assuming that T_{2SW}^* is constant, here we allow T_{2SW}^* to vary so that the surface water signal can be modeled for each pulse moment from the processed FID while limiting a reliance on a priori information. Furthermore, this approach allows for any variations in T_{2SW}^* that might arise from uncertainty in the data, for example due to inhomogeneities in the magnetic field (Grunewald and Knight, 2012).

The results from the LS algorithm are highly dependent on the accuracy of data points measured late in the signal and noisy data points can result in over-cancellation. In order to limit over-cancellation, a lower bound on T_{2SW}^*, $T_{2SW,l}^*$, is defined by estimating T_{2SW}^* from an initial inversion of the uncorrected surface NMR dataset. A value for $T_{2SW,l}^*$ is chosen that divides the surface water signal from the soil water signal. If the signal is still over-canceled, $T_{2SW,l}^*$ is redefined for each pulse moment to the relaxation time determined from a mono-exponential decay fit to the processed FID using an L1-norm. As the L1-norm is less sensitive to outliers than other norms and since it is expected that the surface NMR measurements will be primarily sensitive to signal from the surface water, the L1-norm fit will treats the points early in the decay (i.e., those that are influenced by soil water) as outliers, and will provide a minimum estimate for T_{2SW}^*. Because of the constraints on T_{2SW}^*, A_{0SW} does not need to be constrained.

4.4.2.3 Long-signal inversion algorithm

In the LSI algorithm the processed FID for each pulse moment is inverted to determine a distribution of T_2^* values. To obtain the T_2^* distribution for each pulse moment, the processed FID is inverted using a non-negative least squares inversion algorithm with second order Tikhonov regularization as described in Whitall et al. (1991). The regularization parameter is chosen using the L-curve corner criterion such that the model size and residual are both minimized (Hansen and O'Leary, 1993). Like in the CT approach, a cutoff time, $T_{2SW,l}^*$, is used to split the T_2^* distribution into the signal from the surface water and the signal from soil water. However, unlike the CT approach, which applies the cut off for each layer in the inverted surface NMR dataset, in the LSI

algorithm, the cut off is applied to the data collected at each pulse moment after inverting using a non-negative least squares approach. The log mean T_2^* value of the surface water signal (signal with $T_2^* > T_{2SW,l}^*$) and A_{0SW}^*, determined from the signal with $T_2^* \geq T_{2SW,l}^*$, are used to model the surface water signal for each pulse moment, which is then subtracted from the processed FID. Over-cancellation is not an issue with the LSI algorithm since only a subsample of the T_2^* distribution is used to model the surface water signal and the resulting modeled signals from the LSI algorithm are typically less than the measured signals.

4.4.3 SAVSARP infiltration test

We next discuss the surface water signal suppression algorithms in the context of a surface NMR survey collected during an infiltration study that took place at a large infiltration pond located at the South Avra Valley Storage and Recovery Project (SAVSARP) site between March 21st and April 26th of 2010 (Walsh et al., 2014). The SAVSARP site is located southwest of Tucson, AZ and was built to manage water resources in the central Arizona region. At this site infiltration ponds are used to actively infiltrate surface water diverted from the Colorado River into the local groundwater aquifer. The water table in the area has been described as being greater than 90 m deep (Arizona Department of Water Resources, 2010). Surface NMR measurements were made before, during, and after flooding to monitor infiltration. The first surface NMR dataset was collected on March 21st, prior to flooding, and serves as a background dataset. The next surface NMR dataset was collected on March 29th, after the pond was flooded and surface water was present. Subsequent surface NMR datasets were collected

weekly on April 5th, 12th, and 26th after the water in the pond had infiltrated into the subsurface. In this study we focus on the datasets collected on March 29th (when surface water was present) and on April 5th (when the infiltration pond was empty).

The surface NMR datasets were collected using a 35 m circular figure eight loop, set up on the bottom of the infiltration pond, such that on March 29th the loop was submerged beneath a 1.2 m layer of water. Two additional loops were used to cancel ambient electrical noise during the survey. The surface NMR measurements were made using an enhanced version of the commercial 4–channel GMR instrument with a maximum output of 8 kV and 800 A and a measurement dead-time of 2.8 ms (additional details in Walsh et al., 2014). For all measurements the data record was 4000 ms long. The magnetic field at the site was determined from the IGRF model (Finlay et al., 2010) and confirmed based on the frequency of detected NMR signals.

Electrical resistivity tomography (ERT) was used to determine the resistivity profiles at the SAVSARP site before and after infiltration, which were included in the inversion of the surface NMR datasets (Walsh et al., 2014). Both ERT profiles showed a two-layer resistivity structure. The ERT profile prior to infiltration showed a resistivity of 50 Ωm from 0 m to 5 m depth and a resistivity of 10 Ωm below 5 m depth. The ERT profile following infiltration showed a resistivity of 32 Ωm from 0 m to 5 m depth and a resistivity of 4 Ωm below 5 m depth. The depth of investigation was found to be ~9 m. The ERT results are discussed in more detail in Walsh et al. (2014). Quality assessment, signal processing, adaptive noise cancellation, and stacking of the surface NMR datasets were completed prior to data analysis using the GMR quality control software (GMR QC software; Walsh, 2008). In their initial inversion, Walsh et al. (2014) assumed that the

second layer from the ERT survey was infinitely deep, which led to an estimated depth of investigation for the surface NMR data of ~14 m. Although we recognize that uncertainty in the deep resistivity structure adds uncertainty to the interpretation of surface NMR data, we make the same assumptions here and also find a depth of investigation for the surface NMR survey of 14 m.

4.5 Analysis of Synthetic Datasets

4.5.1 Development of synthetic datasets affected by surface water

Figure 4-3a shows the models used to create the synthetic surface NMR datasets in which a surface water layer of thickness z_{SW} is located over a half-space with variable water content. Rather than creating a synthetic water content profile, we use the surface NMR data acquired as part of the SAVSARP study on April 5th, after the surface water had infiltrated and water was only present in the subsurface. We add to this dataset synthetic data created by modeling a surface NMR signal due to a layer of surface water with thicknesses varying from 0.5 to 5 m.

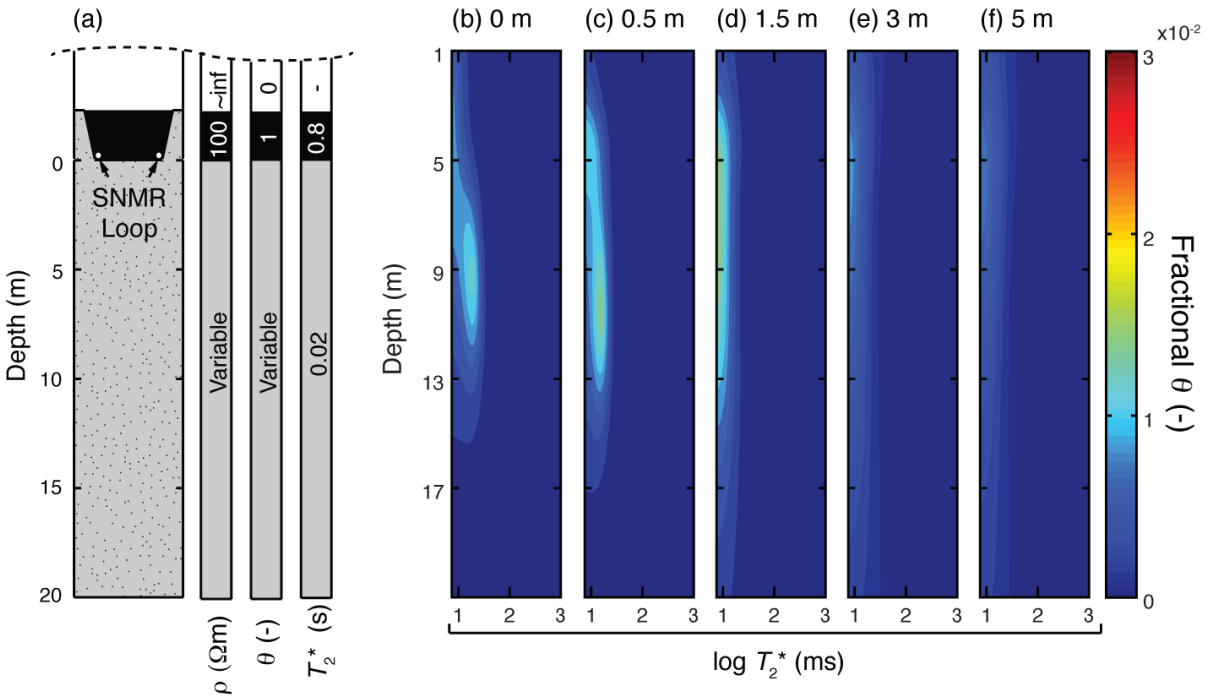

Figure 4-3. The effect of surface water layers of increasing thickness on the surface NMR measurement. A conceptual model of a surface water layer of thickness z_{SW} (a), is shown alongside the inversion results when z_{SW} = 0 m (b), 0.5 m (c), 1.5 m (d), 3 m (e), and 5 m (f). In c through f, all signal with T_2^* > 100 ms has been set to zero to highlight the effect of the surface water on the inverted soil water content, and to show the results when using the CT approach.

The inverted T_2^* distribution profile from the original April 5th dataset (i.e., with no added surface water signal) is shown in Figure 4-3b. The inverted profile shows a variable water content with depth with short T_2^* values. The majority of the water is located between 5 m and 13 m. The T_2^* distribution is centered between 10 ms and 20 ms and varies with depth, increasing from ~10 ms to ~20 ms from ~5 m to ~8 m, and then decreasing from ~20 ms to ~10 ms below ~11 m.

To approximate the surface water signal, we first created a kernel to represent the water and air layers (Kernel 2; Figure 4-3a). In Kernel 2 the resistivity for the water layer was set to 100 Ωm. The air was treated as a perfect resistor, and the loop configuration

and IGRF magnetic field were the same as for the surface NMR dataset collected on April 5th. T_2^* was set to 0.8 s based on an initial inversion of the March 29th dataset (Figure 4-1a). The values used for z_{SW} were 0 m, 0.5 m, 1.5 m, 3 m, and 5 m. No noise was added to the modeled surface water signal in order to preserve the original noise profile of the April 5th dataset.

The inverted profiles for the uncorrected synthetic datasets (i.e., the datasets prior to suppressing the signal associated with the surface water) are shown in Figure 4-3c-f. In all the inverted profiles from the uncorrected synthetic datasets, the signal with $T_2^* > 100$ ms has been set to 0 to highlight the signal from the soil water, which is equivalent to using the CT approach with $T_{2SW,l}^* = 100$ ms to remove the surface water.

It is clear from Figure 4-3c-f that the presence and thickness of the surface water layer substantially affects the soil water content in the inverted profile. When $z_{SW} = 0.5$ m (Figure 4-3c) the uncorrected inverted profile is similar to the original April 5th profile, but with a higher water content throughout. The maximum value in the T_2^* distribution profile increases as z_{SW} increases from 0 to 1.5 m, and then decreases from 1.5 to 5 m. The sum of the signal with $T_2^* <100$ ms is highest for the 1.5 m dataset and decreases when $z_{SW} > 1.5$ m (Figure 4-3f). Furthermore, the water content profile appears to be stretched over a greater region as z_{SW} increases. These results show that the presence of surface water can lead to uncertainty in the interpretation of soil water content and T_2^* distribution profiles and demonstrate that the CT approach is not sufficient to remove the effect of the surface water.

4.5.2 Suppression of surface water signal in synthetic datasets

We now test the three algorithms on the synthetic datasets with surface water layer thicknesses of 1.5 m and 5 m (Figure 4-3d and f). Examples of the uncorrected decay curves from the 1.5 m and 5 m datasets are plotted alongside the corresponding decay curves from the April 5th dataset in Figure 4-4a for q = 0.056 As, in 4-4b for q = 0.5645 As, and in 4-4c for q = 2.081 As. The residual plots calculated by subtracting the corrected datasets from the original April 5th dataset for each algorithm are also plotted in Figure 4-4; Figure 4-4d through f are the residual plots for a 1.5 m thick layer of water and Figure 4-4g through i are the residual plots for a 5 m thick layer of water. The corrected inverted profiles, in which the algorithms were applied to suppress the surface water signal, are shown in Figure 4-5c through e for the 1.5 m layer (top row) and the 5 m layer (bottom row). The inverted profile from the original April 5th dataset is shown in Figure 4-5a and the uncorrected inverted profiles from Figure 4-3d and f are shown in Figure 4-5b for comparison. The water content versus depth profiles are shown in Figure 4-5f for the original and the uncorrected modified April 5th dataset, as well as the datasets corrected using the AP, LS, and LSI algorithms.

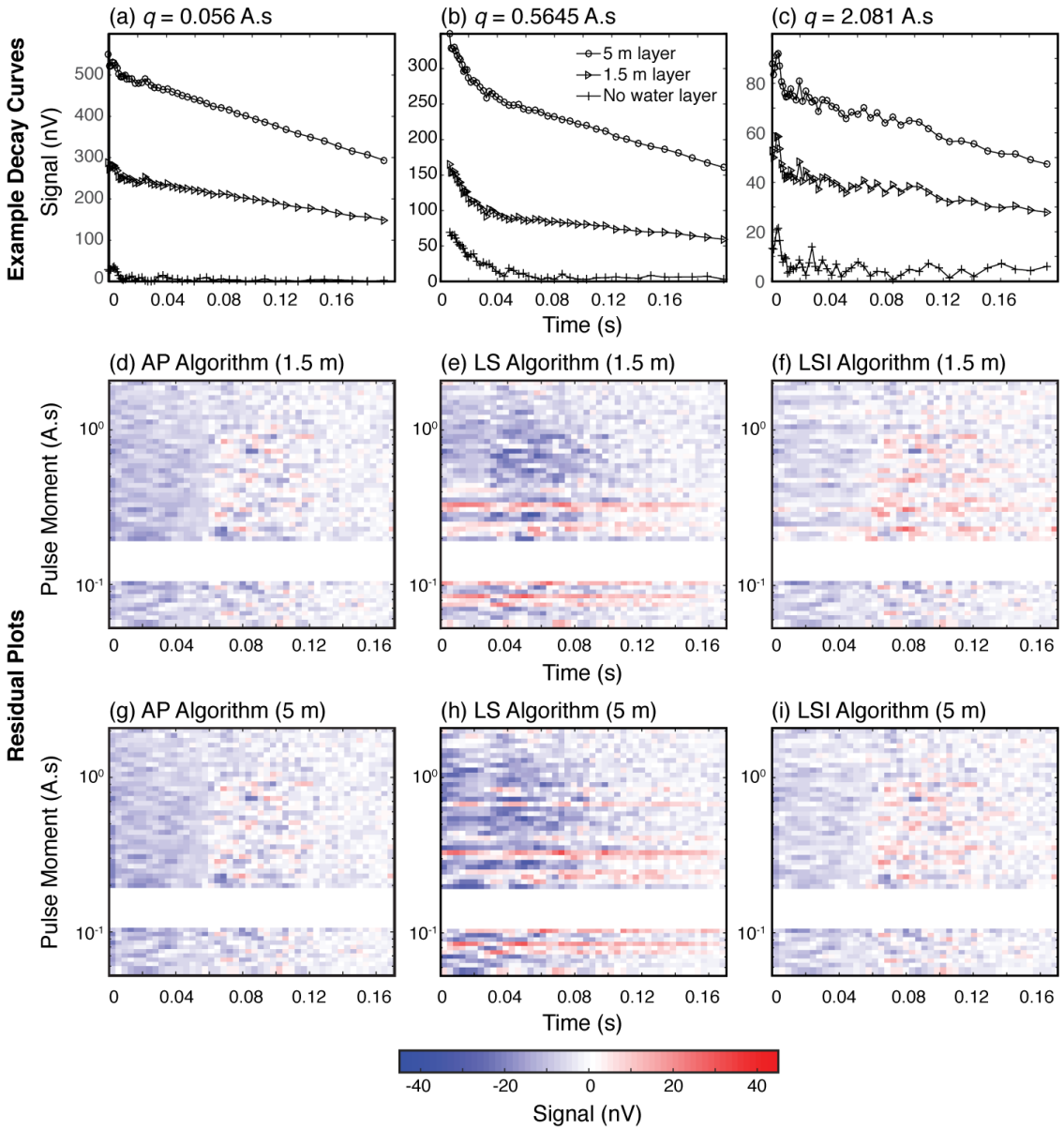

Figure 4-4. The decay curves for the original and modified datasets and the residual plots for the corrected datasets. The decay curves are shown for the original April 5th dataset and the datasets modified with a 1.5 m and 5 m water layer for three pulse moments: q = 0.056 A·s (a), 0.5645 A·s (b), and q = 2.081 A·s, (c). The residual plots, calculated by subtracting the original April 5th processed-FID from the corrected-modified FIDs, are shown for the 1.5 m water layer using the AP (d), LS (e), and LSI (f) algorithms and 5 m water layer using the AP (g), LS (h), and LSI (f) algorithms.

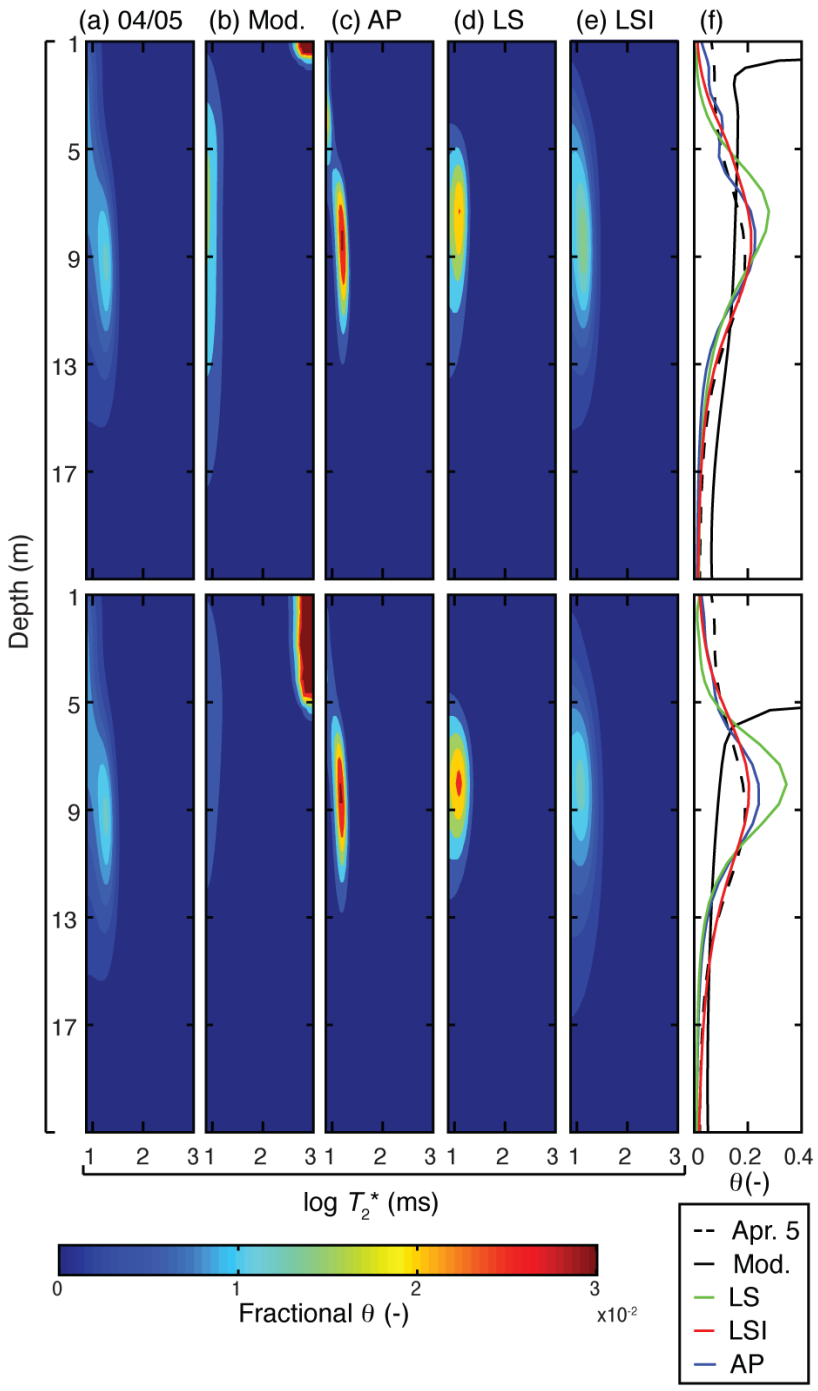

Figure 4-5. The surface water suppression algorithms applied to the synthetic surface NMR datasets shown in Figure 4-3. For reference the original April 5th dataset (a), and the uncorrected, modified datasets (b) are plotted. The inverted images show the surface water layer suppressed using the AP algorithm (c), the LS algorithm (d), and LSI algorithm (e). The water content versus depth profiles from the suppression algorithms and the original water and uncorrected modified profile are shown in (f). The results shown are for a 1.5 m thick surface water layer (top row) and a 5 m thick water layer (bottom row).

Based on the residual plots (Figure 4-4d and g), the AP algorithm produced larger error overall than the LS and LSI algorithms at early times (i.e. $t < 0.06$ s) in the decay curves. Furthermore, from the T_2^* distribution profiles of the datasets corrected using the AP algorithm (Figure 4-5c) we can see that, for the 1.5 m added layer of surface water, the location of the soil water content is recovered. However, the corrected dataset has much narrower T_2^* distributions, with a greater maximum water content, than the original April 5th inverted profile (compare to Figure 4-5a). For the corrected dataset with the 5 m added water layer, as with the 1.5 m layer, the depth location of the soil water content is recovered; the T_2^* distributions of the corrected datasets are again much narrower than the original T_2^* distributions with a higher maximum water content.

The residual plots for the LS algorithm (Figure 4-4e and h) show larger negative error for some pulse moments. Furthermore, for both the 1.5 m and 5 m thick layers, the inverted datasets resulting from the LS algorithm (Figure 4-5d) show constant relaxation time with depth, with the T_2^* distributions centered around ~10 ms. The water content is located between ~5 m and ~12 m, which is similar to the original April 5th profile; however, in the 5 m layer T_2^* distribution profile the maximum water content is greater than in the original inverted April 5th dataset.

The residual plots of both the 1.5 m and 5 m LSI corrected datasets (Figure 4-4f and i) show that this algorithm produces results that most closely match the April 5th dataset, i.e., have the lowest residual. The T_2^* distribution profiles for the datasets corrected using the LSI algorithm (Figure 4-5e) are consistent with the original April 5th dataset, with T_2^* shifting from ~10 ms to ~20 ms between ~4 m and ~13 m. Unlike the inversion results from the AP and LS algorithms, the breadth of the resulting T_2^*

distributions and the maximum water content in the distribution are comparable to the original April 5th dataset.

The water content profiles for all suppression algorithms are shown in Figure 4-5f. When compared to the uncorrected inverted water content profile (solid black line), all suppression algorithms substantially improve the water content profile. For the 1.5 m layer, the position of the original water content profile is recovered using the AP and LSI algorithms, but, for the 5 m layer using the AP algorithm, the maximum predicted water content of the profile is noticeably higher than the original profile, with $\theta \sim 0.25$ at a depth of ~8 m, compared to $\theta \sim 0.2$ with the LSI algorithm. Using the LS algorithm, the maximum predicted water content of the profile is larger than the other algorithms, with $\theta \sim 0.35$ for both the 1.5 m and 5 m datasets, and positioned at shallower depths in the profile at ~7 m, as opposed to ~8 m with the AP and LSI algorithms.

4.6 Discussion of Synthetic Results

In Figure 4-3, we demonstrated that a layer of surface water has an adverse effect on the interpretation of a surface NMR dataset, that increasing the thickness increased this effect, and that the CT approach does not sufficiently resolve these interpretation issues. In this section, using the synthetic datasets produced by modifying the April 5th dataset (Figure 4-5), we evaluate the effectiveness of each of the three algorithms used to suppress the signal associated with the surface water and compare them to the CT approach (using a cutoff time of 100 ms). The algorithms are evaluated based on the following criteria: (1) Does the suppression algorithm remove the surface water signal

from the dataset? (2) Does the corrected T_2^* distribution profile match the original T_2^* distribution profile? And, (3) does the corrected water content profile match the original water content profile?

From Figure 4-5, we can see that all three algorithms and the CT approach satisfy criterion 1; the majority of the signal associated with the surface water is removed from the inverted datasets (Figure 4-5c-e). The sum of the signal with $T_2^* > 100$ ms, is used here to indicate the signal associated with the surface water and to determine how much of the surface water was canceled with each algorithm; the percent reduction for each algorithm is given in Table 4-1. The values for the sum of the normalized signal with $T_2^* > 100$ ms are 9.7 and 20.9 for the uncorrected 1.5 m and 5 m datasets respectively. The sum of the signal associated with the surface water is reduced by >90% using all algorithms. The LSI algorithm performs the best, reducing the signal by 99.0% and 99.8% for the 1.5 m and 5 m datasets respectively. The LS algorithm performs the poorest and only reduces the signal by 91.0% and 96.6% for the 1.5 m and 5 m datasets respectively. The CT approach cancels all signal with $T_2^* > 100$ ms as these values are explicitly set to 0.

Table 4-1. An evaluation of the CT method and the AP, LS, and LSI algorithms to remove surface water signal from a surface NMR dataset. The percent reductions in the surface water signal are shown (column 3), along with the RMSD values calculated by comparing the T_2^* distribution profiles (column 4), and water content profiles (column 5) to the original April 5th dataset.

z_{sw} (m)	Correction method	Reduction in surface water signal (%)	RMSD of T_2^* distribution profile	RMSD of θ profile
1.5	**CT**	100	0.002	0.03
	AP	99.0	0.003	0.03
	LS	91.0	0.003	0.07
	LSI	99.0	0.002	0.03
5	**CT**	100	0.002	0.04
	AP	99.6	0.003	0.03
	LS	96.6	0.003	0.06
	LSI	99.8	0.001	0.03

We evaluate criterion 2 by comparing the root mean squared deviation (RMSD) values calculated from the differences between the corrected T_2^* distribution profiles and the original inverted dataset. The RMSD values for each of the corrected datasets and the CT approach are given in Table 4-1. The LS algorithm has the largest RMSD value for both layer thicknesses (RMSD = 0.003 for both datasets), and so reproduces the original dataset the worst. The LSI algorithm performs better than the LS and AP algorithms and slightly better than the CT approach, with RMSD values of 0.002 and 0.001 for the 1.5 and 5 m datasets respectively. Thus, according to criterion 2, the LSI algorithm performs the best in that it most closely reproduces the original datasets.

We evaluate criterion 3 by calculating the RMSD values from the difference between the corrected water content profile and the original inverted water content profile. The RMSD values for each of the corrected datasets and the CT approach are

given in Table 4-1 for the surface water layer thicknesses of 1.5 and 5 m. The RMSD values for the water content profiles corrected using the LS algorithm are higher than for all other algorithms, including the CT approach. The AP and LSI algorithms have RMSD values of 0.03 for both the 1.5 m and 5 m datasets, which are comparable to the CT approach (0.03 and 0.04 for the 1.5 and 5 m thick layers respectively). Thus, according to criterion 3, the AP and LSI algorithms perform the best.

Using the above stated criteria, we conclude that the LSI algorithm produces datasets corrected for a layer of surface water that are most similar to the original dataset. Using the LSI algorithm has the added advantage of not requiring accurate a priori knowledge, as required by the AP algorithm, or additional survey loops, such as the noise cancellation approach outlined in Walsh et al. (2014). Furthermore, the LSI algorithm cannot over-cancel the data making it less susceptible to processing errors, and, unlike the CT approach, does not have the interpretation issues highlighted in Figure 4-3.

4.7 Field Example and Results

We next consider the surface NMR dataset collected on March 29th at the SAVSARP site, in which there was a 1.2 m thick layer of surface water present at the time of the measurement. We present the results from the corrected March 29th datasets, in which the signal from the surface water was suppressed using the LSI algorithm (Figure 4-6b) alongside the other surface NMR datasets from the SAVSARP survey (March 21st, Figure 4-6a; April 5th, Figure 4-6c; April 12th, Figure 4-6d; and April 26th, Figure 4-6e). The ERT profile collected following infiltration was used to create the kernel used to invert the March 29th through April 26th datasets, while the ERT profile

collected before infiltration was used to create the kernel used to invert the March 21st dataset.

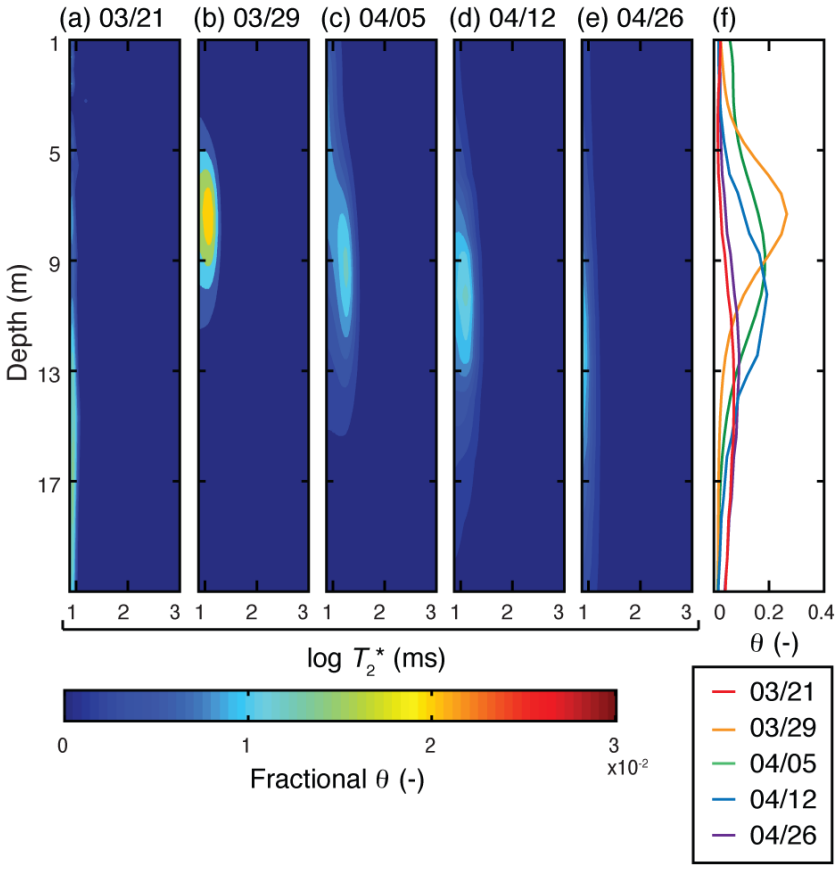

Figure 4-6. Relaxation time distributions versus depth for the SAVSARP surface NMR survey for data collected on March 21st (a) prior to flooding, March 29th corrected with the LSI algorithm (b), April 5th (c), April 12th (d), and April 26th (e). The water content versus depth profiles are shown in (f).

We first consider the March 29th dataset without correcting for the surface water signal (Figure 4-1a). The uncorrected inverted profile shows a prominent signal at shallow depths (< 5 m) with $T_2^* \geq 200$ ms, which we interpret to be the signal originating from the surface water. The soil water is located from a depth starting at ~2 m; at ~9 m the soil water content starts to decrease and reaches zero at ~13 m. Based on the

uncorrected T_2^* distribution profile from the March 29th dataset, we set $T_{2SW,l}^*$ = 200 ms for the LSI algorithm.

The inversion results after correcting the March 29th dataset with the LSI algorithm (Figure 4-6b) produce narrower T_2^* distributions versus depth than the uncorrected dataset. This T_2^* distribution versus depth profile is similar to the April 5th inverted dataset and is consistent with the inverted profiles from other days in the survey, with T_2^* distributions centered at T_2^*~10 ms.

The water content profiles for all days during the SAVSARP survey are shown in Figure 4-6f. For the March 29th dataset corrected using the LSI algorithm, the water content profiles show that the soil water is located between ~4 m and ~11 m with $\theta < 0.3$. The position of water on March 29th after correcting with the LSI algorithm is consistent with the inverted images from the other days of the survey, in which a body of infiltrating water is observed to be moving vertically downward and occupying a larger region of the subsurface over time.

4.8 Conclusion

In this study we present three algorithms for suppressing the signal associated with a large body of surface water measured during a surface NMR measurement: the a priori, the late-signal, and the long-signal-inversion algorithms. In each of the algorithms, the surface water signal is modeled and then subtracted from a processed and stacked dataset prior to inverting. As a result, these suppression algorithms can be used with any inversion algorithm and do not require new data collection schemes, such as new pulse

sequences or loop configurations, in order to obtain information about the soil water content. We note that, in the case where the water layer has a low resistivity (< two times the loop diameter), the kernel used in the inversion will need to be adapted to account for the effect of the water layer. While this study focused on removing the unwanted NMR signal associated with a body of standing water present during an infiltration test, the algorithms outlined here are applicable to any survey scenario where collecting NMR data in the vicinity of a large body of surface water is unavoidable.

The a priori, late-signal, and long-signal-inversion algorithms were found to work for datasets with surface water layers up to 5 m. Of the three algorithms, the long-signal-inversion algorithm, in which an initial non-negative least squares inversion of the processed FID at each pulse moment, is used to determine the contribution from the surface water signal, was found to be the most effective at suppressing the surface water signal. This algorithm requires little a priori knowledge, and produces inverted datasets with less error than using a cutoff time approach, in which only the signal less than a minimum value of 100 ms is considered. Finally, using a dataset collected during an infiltration experiment, we show that the LSI algorithm can be used to correct for the surface water signal in a field setting. The algorithms presented in this study show that surface NMR data can be accurately interpreted when collected in close vicinity to bodies of surface water.

Chapter 5

Summary of Research

5.1 NMR Relaxation as a Function of Saturation

This thesis is focused on developing NMR measurements as a means to study the vadose zone. The laboratory studies expand upon attempts to approximate the water retention curve (WRC) from saturated NMR measurements (Costabel and Yaramanci, 2011b; Costabel and Yaramanci, 2013; Costabel and Günther, 2014), by considering NMR measurements of unsaturated unconsolidated geologic media. Chapters 2 and 3 focus on understanding the NMR relaxation time versus saturation relationship.

In Chapter 2, the NMR relaxation versus saturation relationship was found to be a function of both the mean grain size, $d_{mean,}$ and the total iron content. While these characteristics are indirectly related to the NMR measurement, they are directly related to two physical characteristics that are important for the interpretation of NMR relaxation times: the mean pore size, r_{ML}, and surface relaxivity ρ_2. Saturated transverse relaxation time, T_2, distributions were found to be related to the d_{mean} and ρ_2 of the sample material. The relative shape of the surface relaxation, T_{2S}, versus saturation curves, measured during imbibition, was also found to be related to both d_{mean} and ρ_2. This result indicates that the relationship between relaxation time and saturation is dependent on the sample material's diffusion regime, which is itself a function of r_{ML} and ρ_2. The relative T_{2S} versus saturation curves were found to be linear for fast diffusion samples and exhibited a

power law relationship when the fast diffusion assumption was violated. Contrary to other studies, the relative T_{2S} versus saturation curves were not accurately explained by models based on ideal filling mechanisms such as a thin film (Costabel, 2011) or a capillary tube model (Falzone and Keating, 2016a). The inability of these models to predict the relaxation behavior exhibited by the samples in this study indicates that contemporary models based on ideal filling mechanisms are not sufficient for explaining relaxation that occurs outside the fast diffusion regime in unsaturated geologic media. This study shows that future models need to account for samples that relax outside the fast diffusion regime in order to explain NMR measurements in unsaturated geologic media.

The focus of Chapter 3 was the effect of drainage and imbibition hysteresis, a phenomenon common to the WRC, on T_2. Specifically, the effect of hysteresis on the T_{2ML}^{-1}-θ and SOE-θ curves were evaluated. Previous studies have predicted NMR sensitivity to hysteresis in models consisting of pores with ideal shapes (triangular pores; Mohnke et al., 2015), while other studies collected measurements under drainage and imbibition at low field strengths (20 MHz; Porion et al., 1998) and did not observe hysteresis. This study focused on unconsolidated geologic material that represents a range of both d_{mean} and ρ_2, analyzed at field strengths typical to NMR field instruments (i.e. 2 MHz). Despite all WRCs exhibiting hysteresis, the T_{2ML}^{-1}-θ and SOE-θ curves did not show hysteresis. While there are similarities between the T_{2ML}^{-1}-θ and SOE-θ curves and the WRCs in this study, the inability of these NMR parameters to measure hysteresis makes the measurement incapable of discerning from drainage and imbibition. The results of this study are well explained by a hypothetical filling model based on an

interconnected pore network, in which there are multiple pathways between pores. This model predicts that, for samples that have narrow pore size distributions and well connected pores, the WRC will exhibit hysteresis, however the α/r-θ curve will not be effected by drainage and imbibition history. These findings indicate that NMR may be capable of measuring either the drainage, imbibition, or an average WRC.

The experiments from Chapter 2 and 3 represent two different filling processes. The imbibition data presented in Chapter 2 was measured under continuous flow, and therefore likely represents a transient saturation state. The drainage and imbibition data presented in Chapter 3, however, was collected at static equilibrium. Comparing these datasets can be used to evaluate how the relaxation time versus saturation relationship is effected by the equilibrium state of the samples. In Figure 5-1, the $T_{2S,Rel}$ versus S_{NMR} curves are shown for the synthetic sands appearing in both Chapter 2 and 3 (uF, hF, uC, hC), plotted alongside the identity line for comparison. For the porous plate experiment, all $T_{2S,Rel}$ versus S_{NMR} curves appear to be linear during both drainage and imbibition. It is not possible to interpret the imbibition curves for uC and hC due to the inability of the samples to saturate under imbibition. The most noticable difference between the experiments is found in the comparison of the curves from the Group 2 samples defined in Chapter 2 (hF and hC), in which $\kappa \geq 0.1$. For these samples, the porous plate experiment produced linear curves, or $\lambda \sim 1$, versus the curves measured during the imbibition experiment, in which $\lambda > 1$. This observation was not evident for the Group 1 samples ($\kappa < 0.1$), in which all curves had $\lambda \sim 1$. The difference in these curves indicates that the relaxation time versus saturation relationship is not dependent on the equilibrium state of samples within the fast diffusion regime, but is dependent on the equilibrium

state of samples exhibiting relaxation outside the fast diffusion regime. These observations indicate the $T_{2S,Rel}$ versus S_{NMR} curves are representative of the equilibrium state of some samples; however a broader study is needed to study this effect further.

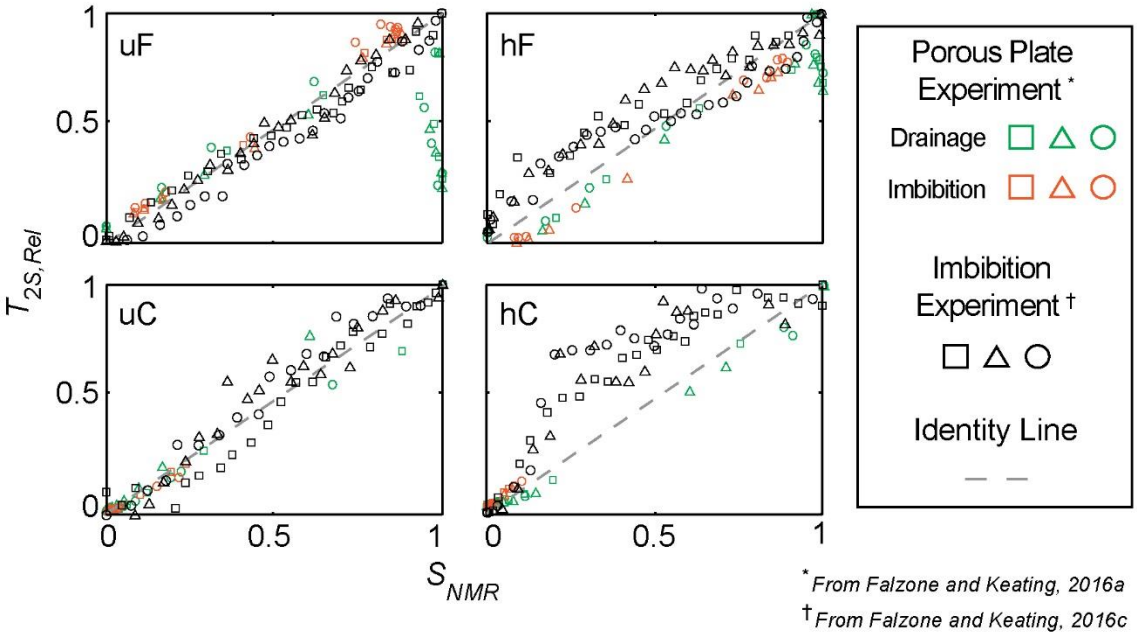

Figure 5-1. A comparison of the $T_{2S,Rel}$ versus S_{NMR} curves measured during the imbibition experiment discussed in Chapter 2 to the curves measured with the porous plate experiment during drainage and imbibition discussed in Chapter 3.

There is a considerable amount of evidence in the literature linking NMR relaxation time to the pore size of a saturated porous media (Timur, 1969; Seevers, 1966; Brownstein and Tarr, 1979; Godefroy et al., 2001), and also considerable amount of evidence that NMR relaxation time in unsaturated porous media is a function of saturation (Costabel and Yaramanci, 2011b; Costabel and Yaramanci, 2013; Bird and Preston, 2004; Ioannidis et al., 2006; Falzone and Keating, 2016a; Porion et al., 1998). The data in these studies confirm these observations, and suggest that NMR can provide

useful information to characterize processes in the vadose zone. The ability to characterize the filling mechanism of unsaturated porous media, and the physical nature of a pore space, remains a difficult task through conventional measurements (Romero and Simms, 2008). While the ability to directly relate NMR measurements to the WRC is currently not available, interpreting NMR relaxation times can provide knowledge about the pore filling mechanism, the pore size distribution, and the connectivity of the pore network, as demonstrated in this thesis.

5.2 Considerations for NMR Field Studies

The NMR relaxation time versus θ relation examined in the laboratory components of this thesis have important implications for field work, in that this relation has the potential to provide new non-invasive methods for characterizing water retention in situ. However, the use of infiltration tests to probe the vadose zone presents a clear problem for surface NMR datasets in that surface water associated with an infiltration test will directly affect the measurement. Consequently, data similar to what is presented in Chapters 2 and 3 may be difficult to obtain in a field setting. Chapter 4 provides a solution for the problem associated with the presence of surface water, and proves that NMR field measurements can aid conventional field experimental surveys of the vadose zone.

By reducing the signal associated with surface water, a surface NMR dataset can be made more sensitive to signal originating from the subsurface. Three surface water cancellation algorithms are presented in chapter 4, which can be applied to surface NMR

data prior to the inversion code. Of focus in this study is the survey presented in Walsh et al. (2014), in which an infiltration test using surface NMR as a monitoring tool was affected by the presence of a surface water layer. The datasets corrected using these algorithms on the synthetic modified April 5th dataset were found to be statistically similar to the original April 5th dataset. These results prove the use of a separate processing algorithm to the inversion code can remove unwanted surface water signal. Of particular interest is the Long-Signal Inversion algorithm, which requires little a priori information about a survey site. Similarities between the March 29th dataset, which was collected in the presence of a surface water layer, following cancellation with the LSI algorithm showed similar features to the rest of the datasets from the survey presented in Walsh et al. (2014). While this study focused specifically on an infiltration test, the algorithms outlined in this study may be useful for other scenarios in which signal from a body of surface water is significant. One example is the scenario presented in Parsekian et al. (2013), in which measuring the signal originating from a lake is unavoidable. The algorithms presented in Chapter 4 show that useful data from an infiltration test can be obtained from NMR field measurements despite the presence of large bodies of surface water.

5.3 Future Research

The laboratory components in this thesis improve our understanding of how NMR measurements are affected by variations in saturation, with the ultimate goal of determining the WRC in the field. While the research topics discussed in this thesis advance NMR as a field method to study the vadose zone, more research is needed

towards this goal. To accurately determine the WRC from NMR measurements, a comprehensive understanding of the relation between the pore size distribution and the relaxation time distribution is needed. This topic is not addressed specifically in this thesis, and relies on an independent understanding of ρ_2 to directly relate relaxation time to pore size. Developing petrophysical relationships that accurately relate the relaxation time distribution to the pore size distribution should receive a great deal of investigation in the future in order to improve analysis of both saturated and unsaturated samples.

Despite limitations in our ability to relate the relaxation time and pore size distributions, our current understanding of NMR measurements of unsaturated geologic media can still provide useful information of the hydrogeology of the vadose zone. While determining the WRC with NMR is still an experimental method, our level of understanding of how relaxation time relates to the WRC has progressed to the extent that field methods may provide important corroborating evidence for specific vadose zone environmental topics. The ability to directly determine the WRC with NMR measurements is not yet available; however the ability to rank the WRCs of samples with similar physical and mineralogical characteristics is possible. NMR can be used as a comparative method with the relationships defined in this thesis. This makes it possible for studying topics such as hydrophobicity (Nourmahnad et al., 2015), compaction (Smith et al., 2001), cementation (Hoyos et al., 2007), and other processes that involve changes in the WRC of a soil.

The use of NMR field measurements to support greater research projects focusing on the vadose zone, such as those focusing on agricultural issues (HLEF, 2009), could greatly improve our understanding of both the measurement and hydrogeologic

processes. The acceptance of NMR field measurements for vadose zone research would benefit from more case studies, in which NMR measurements are demonstrated alongside other methods (e.g. Knight et al., 2013). These types of studies should be prioritized for future NMR field research, as NMR has the potential to inform water resource management practices.

References

Archie, G.E., (1942), The electrical resistivity log as an aid in determining some reservoir characteristics, *Transactions of the AIME* **146**(1), 54–62.

Arizona Department of Water Resources, (2010), Active management areas, *in Arizona water atlas*, 8.5.

Attwa, M. and T. Günther, (2013), Spectral induced polarization measurements for predicting the hydraulic conductivity in sandy aquifers, *Hydrol. Earth Syst. Sci.***17**:4079-4094.

Behroozmand, A., K. Keating, and E. Auken, (2015), A review of the principles and applications of the NMR technique for near-surface characterization, *Surveys in Geophysics* **9**, 1-59.

Binley, A., L.D. Slater, M. Fukes, and G. Cassiani, (2005), Relationship between spectral induced polarization and hydraulic properties of saturated and unsaturated sandstone, *Water Resources Research* **41**(12):W12417

Bird, N.R.A. and A.R. Preston, (2004), Measurement of the size distribution of water-filled pores at different matric potentials by stray field nuclear magnetic resonance, *European Journal of Soil Science* **56**, 135–143.

Blasch, K., T.P.A. Ferré, A.H. Christensen, and J.P. Hoffmann, (2002), New field method to determine streamflow timing using electrical resistance sensors, *Vadose Zone Journal* **1**, 289–299.

Bloembergen, N. and L.O. Morgan, (1961), Proton relaxation times in paramagnetic solutions: Effects of electron spin relaxation, *The Journal of Chemical Physics* **34**(3), 842–850.

Brooks, R.J. and A.T. Corey, (1964), Hydraulic properties of porous media, *Hydrol. Pap.* **3**, 1-37.

Brownstein, K.R. and C.E. Tarr, (1979), Importance of classical diffusion in NMR studies of water in biological cells, *Physical Review A.* **19**(6), 2446–2453.

Bryar, T.R. and R.J. Knight, (2002), Sensitivity of nuclear magnetic resonance relaxation measurements to changing soil redox conditions, *Geophysical Research Letters* **29**(24), 50-1–50-4.

Buckingham, E., (1907), Water retention in soil, *Soil Bulletin (U.S. Department of Agriculture)* **36**.

Callaghan, P., (2011), Translational Dynamics and Magnetic Resonance: Principles of Pulsed Gradient Spin Echo NMR. Oxford University Press, Oxford, UK

Carr, H.Y. and E.M. Purcell, (1954), Effects of diffusion on free precession in nuclear magnetic resonance experiments, *Physical Review* **94**(3), 630–638.

Chang, D. and M.A. Ioannidis, (2002), Magnetization evolution in network models of porous rock under conditions of drainage and imbibition, *Journal of colloid and interface science* **253**, 159–170.

Chen, S., D. Georgi, C. Liu, and H.F. Thern, (2000), Summation of echoes: a simple, robust means for interpreting Nmr data, *SPWLA 41st Annual Logging Symposium*, 4–7 June, Dallas, Texas.

Chen, S., H.K. Liaw, and A.T. Watson, (1994), Measurements and analysis of fluid saturation-dependent NMR relaxation and linebroadening in porous media, *Magnetic Resonance Imaging* **12**(2), 201–202.

Christiansen, L., P.J. Binning, D. Rosbjerg, O.B. Andersen, and P. Bauer-Gottwein, (2011), Using time-lapse gravity for groundwater model calibration: an application to alluvial aquifer storage, *Water Resources Research*, **47**(6), W06503, 1–12

Constantz, J. and C.L. Thomas, (1996), The use of streambed temperature profiles to estimate depth, duration, and rate of percolation beneath arroyos, *Water Resources Research*, **32**(12), 3597–3602.

Costabel, S., (2011), Nuclear magnetic resonance on laboratory and field scale for estimating hydraulic parameters in the vadose zone, Ph.D. Thesis, Berlin University of Technology

Costabel, S. and U. Yaramanci, (2011a), Relative hydraulic conductivity in the vadose zone from magnetic resonance sounding – Brooks-corey parameterization of the capillary fringe, *Geophysics* **76**(3), G61–G71.

Costabel, S. and U. Yaramanci, (2011b), Relative hydraulic conductivity and effective saturation from Earth's field nuclear magnetic resonance – a method for assessing the vadose zone, *Near Surface Geophysics*, **9**(2), 155–167.

Costabel, S. and U. Yaramanci, (2013), Estimation of water retention parameters from nuclear magnetic resonance relaxation time distributions, *Water Resour. Res.* **49**(4), 2068–2079.

Costabel, S. and T. Günther, (2014), Noninvasive estimation of water retention parameters by observing the capillary fringe with magnetic resonance sounding, *Vadose Zone J.* **13**(6), 1–14.

Dahan, O., E.V. McDonald, and M.H. Young, (2003), Flexible time domain reflectometry probe for deep vadose zone monitoring, *Vadose Zone J.* **2**(2), 270–275.

D'Orazio, F., S. Bhattacharja, S.P. Halperin, and R. Gerhardt, (1990), Molecular diffusion and nuclear-magnetic-resonance relaxation in unsaturated porous silica glass, *Physical Review B* **42**(16), 9810–9818.

Dlubac, K., R. Knight, Y. Song, N. Bachman, B. Grau, J. Cannia, and J. Williams, (2013), Use of NMR logging to obtain estimates of hydraulic conductivity in the High Plains aquifer, Nebraska, USA, *Water Resour. Res.* **49**(4), 1871–1886.

Dlugosch, R., T. Günther, M. Müller-Petke, and U. Yaramanci, (2013), Improved prediction of hydraulic conductivity for coarse-grained unconsolidated material from nuclear magnetic resonance, *Geophysics* **78**(4), EN55–EN64.

Dunn, K., D.J. Bergman, and G.A. Latorraca, (2002), Nuclear Magnetic Resonance-Petrophysical and Logging Applications, Elsevier Science, Oxford, UK

Falzone, S. and K. Keating, (2016a), A numerical and laboratory study to determine the effect of pore size, surface relaxivity and saturation on NMR relaxation measurements, In Press *Near Surf. Geophys.*

Falzone, S. and K. Keating, (2016b), Algorithms for removing surface water signals from surface NMR infiltration surveys, Submitted *Geophysics.*

Falzone, S. and K. Keating, (2016c), The NMR relaxation response of unconsolidated sediments during drainage and imbibition, Submitted *Vadose Zone J.*.

Ferré, T.P.A., A. Binley, K.W. Blasch, J.B. Callegary, S.M Craford, J.B. Fink, A.L. Flint, L.E. Flint, J.P. Hoffmann, J.A. Izbicki, M.T. Levitt, D.R. Pool, and B.R. Scanlon, (2007), *Geophysical methods for investigating ground-water recharge*, Geological Survey (U.S.) Professional Paper 1703, Appendix 2, 375–412.

Finlay, C.C., S. Maus, C.D. Beggan, T.N. Bondar, A. Chambodut, T.A. Chernova, A. Chulliat, V.P. Golovkov, B. Hamilton, M. Hamoudi, R. Holme, G. Hulot, W. Kuang, B. Langlais, V. Lesur, F.J. Lowes, H. Lühr, S. Macmillan, M. Mandea, S. McLean, C. Manoj, M. Menvielle, I. Michaelis, N. Olsen, J. Rauberg, M. Rother, T.J. Sabaka, A. Tangborn, L. Tøffner-Clausen, E. Thébault, A.W.P. Thomson, L. Wardinski, Z. Wei, and T.I. Zvereva, (2010), *International Geomagnetic Reference Field: the eleventh generation: Geophysical Journal International* **183**(3), 1216–1230.

Fisher, A.T, (2013), Aquifer storage and recovery and managed aquifer recharge using wells: planning, hydrogeology, design, and operation, *Groundwater* **51**(3), 314–315.

Foley, I., S.A. Farooqui, and R.L. Kleinberg, (1996), Effect of paramagnetic ions on NMR relaxation of fluids at solid surfaces, *Journal of Magnetic Resonance, Series A* **123**(1):95–104.

Godefroy, S., J.P. Korb, M. Fleury, and R. Bryant, (2001), Surface nuclear magnetic relaxation and dynamics of water and oil in macroporous media, *Physical Review E* **64**(2), 021605-1–13.

Grunewald, E. and R. Knight, (2012), Nonexponential decay of the surface-NMR signal and implications for water content estimation, *Geophysics*, **77**(1), EN1–EN9.

Hansen, P.C. and D.P. O'Leary, (1993), The use of the L-curve in the regularization of discrete ill-posed problems, *SIAM Journal on Scientific Computing* **14**(6), 1487–1503.

Hen-Jones, R.M., P.N. Hughes, S. Glendinning, D.A. Gunn, J.C. Chambers, P.B. Wilkinson and S. Uhlemann, (2014), Determination of moisture content and soil suction in engineered fills using electrical resistivity, *6th International Conference on Unsaturated Soils, UNSAT, Sydney, Australia*, 1695–1699.

Hinedi, Z.R., Z.J. Kabala, T.H. Skaggs, D.B. Borchard, R.W.K. Lee, and A.C. Chang, (2010), Probing soil and aquifer material porosity with nuclear magnetic resonance, *Water Resources Research* **29**(12), 3861–3866.

Hoyos, L., H. Thudi, and A. Puppala, (2007), Soil-water retention properties of cement treated clay, *Problematic Soils and Rocks and in situ Characterization, America Society of Civil Engineers, GeoDenver 2007*:1-8.

Ioannidis, M.A., I. Chatzis, C. Lemaire, and R. Perunarkilli, (2006), Unsaturated hydraulic conductivity from nuclear magnetic resonance measurements, *Water Resources Research* **42**(7), W07201.

Jaeger, F., S. Bowe, H. Van As, and G.E. Schaumann, (2009), Evaluation of 1H NMR relaxometry for the assessment of pore-size distribution in soil samples, *European Journal of Soil Science* **60**(6), 1052–1064.

Jayawickreme, D.H., R.L. Van Dam, and D.W. Hyndman, (2010), Hydrological consequences of land-cover change: quantifying the influence of plants on soil moisture with time-lapse electrical resistivity, *Geophysics* **75**(4), WA43–WA50.

Keating, K. and S. Falzone, (2013), Relating NMR relaxation time distributions to particle size distributions for unconsolidated sand packs, *Geophysics* **78**(6), D461-D472.

Keating, K. and R. Knight, (2007), A laboratory study to determine the effects of iron oxides on proton NMR measurements, *Geophysics* **72**(1), E27.

Keating, K. and R. Knight, (2008), A laboratory study of the effect of magnetite ion NMR relaxation rates, *Journal of Applied Geophysics* **66**(3), 188-196.

Keating, K. and R. Knight, (2010), A laboratory study of the effect of Fe (II)-bearing minerals on nuclear magnetic resonance (NMR) relaxation measurements, *Geophysics* **75**(3), F71–F82.

Kenyon, W.E., (1991), Nuclear magnetic resonance as a petrophysical measurement, *Nuclear Geophysics* **6**(2), 153–172.

Kenyon, W.E., C. Straley, and J.F. Willemsen, (1988), A three-part study of NMR longitudinal relaxation properties of water-saturated sandstones, *SPE Form. Eval.* **3**(3), 622–636.

Kleinberg, R.L. and M.A. Horsfield, (1990), Transverse relaxation processes in porous sedimentary rocks, *Journal of Magnetic Resonance, Series* **88**(1), 9–19.

Kleinberg, R.L., W.E. Kenyon, and P.P. Mitra, (1994), Mechanisms of NMR relaxation of fluids in rocks, *Journal of Magnetic Resonance, Series A* **108**(2), 206–214.

Knight, R., E. Grunewald, T. Irons, K. Dlubac, Y. Song, H.N. Bachman, B. Grau, D. Walsh, J.D. Abraham, and J. Cannia, (2012), Field experiment provides ground truth for surface nuclear magnetic resonance measurement, *Geophysical Research Letters* **39**(3), L03304-1–7.

Knight, R., D.O. Walsh, J.J. Butler Jr., E. Grunewald, G. Liu, A.D. Parsekian, E.C. Reboulet, S. Knobbe, and M. Barrows, (2015), NMR logging to estimate hydraulic conductivity in unconsolidated aquifers, *Ground Water*, 1-11.

Koorevaar, P., G. Menelik, and C. Dirksen, (1983), Elements of soil physics. 1st im. Elsevier Science B.V., Amsterdam

Legchenko, A., J.M. Baltassat, A. Beauce, and J. Bernard, (2002), Nuclear magnetic resonance as a geophysical tool for hydrogeologists, *Journal of Applied Geophysics* **50**(1-2), 21–46.

Legchenko, A., J.M. Baltassat, A. Bobachev, C. Martin, H. Robain, and J.-M. Vouillamoz, (2004), Magnetic resonance sounding applied to aquifer characterization, *Ground Water* **42**(3), 363–373.

Legtchenko, A., (2013), Magnetic resonance imaging for groundwater: John Wiley & Sons, Technology and Engineering.

Likos, W.J., N. Lu, and J.W. Godt, (2014), Hysteresis and uncertainty in soil water-retention curve parameters, *J. Geotech. Geoenviron. Eng.* **140**(4):

Mattea, C., R. Kimmich, I. Ardelean, S. Wonorahardjo, and G. Farrher, (2004), Molecular exchange dynamics in partially filled microscale and nanoscale pores of silica glasses studied by field-cycling nuclear magnetic resonance relaxometry, *Journal of Chemical Physics* **121**, 10648–10656.

Mawer, C., P. Kitanidis, A. Pidlisecky, and R. Knight, (2013), Electrical resistivity for characterization and infiltration monitoring beneath a managed aquifer recharge pond, *Vadose Zone J.* **12**(1), 1–20.

Meiboom, S. and D. Gill, (1958), Modified spin-echo method for measuring nuclear relaxation times, *Review of Scientific Instruments* **29**, 688–691.

Miller, E.E. and R.D. Miller, (1956), Physical theory for capillary flow phenomena, *J. Appl. Phys.* **27**, 324–332.

Mohnke, O., (2014), Jointly deriving NMR surface relaxivity and pore size distributions by NMR relaxation experiments on partially desaturated rocks, *Water Resour. Res.* **50**(6), 5309–5321.

Mohnke, O., R. Jorand, C. Nordlund, and N. Klitzsch, (2015), Understanding NMR relaxometry of partially water-saturated rocks, *Hydrol. Earth Syst. Sci.* **19**, 2763–2773.

Mohnke, O. and U. Yaramanci, (2005), Forward modeling and inversion of MRS relaxation signals using multi-exponential decomposition, *Near Surface Geophysics* **3**(3), 165–185.

Mohnke, O. and U. Yaramanci, (2008), Pore size distributions and hydraulic conductivity of rocks derived from magnetic resonance sounding relaxation data using multi-exponential decay time inversion, *Journal of Applied Geophysics* **66**, 73–81.

Mualem, Y., (1974), A new model for predicting the hydraulic conductivity of unsaturated porous media, *Water Resour. Res.* **12**, 513–522.

Müller, M., S. Kooman, and U. Yaramanci, (2005), Nuclear magnetic resonance (NMR) properties of unconsolidated sediments in field and laboratory, *Near Surface Geophysics*, **3**(4), 275–285.

Müller-Petke, M., R. Dlugosch, and U. Yaramanci, (2011a), Evaluation of surface nuclear magnetic resonance-estimated subsurface water content, *New J. of Phys.* **13**, 1–18.

Müller-Petke, M., T. Hiller, R. Herrmann and U. Yaramanci, (2011b), Reliability and limitations of surface NMR assessed by comparison to borehole NMR, *Near Surface Geophysics* **9**(2), 123–134.

Müller-Petke, M. and U. Yaramanci, (2010), QT inversion – comprehensive use of the complete surface NMR data set, Geophysics **75**(4), WA199–WA209.

Muñoz-Castelblanco, J., J.-M. Pereira, P. Delage and Y.-J. Cui, (2012), The influence of changes in water content on the electrical resistivity of a natural unsaturated loess, *ASTM Geotech. Test. J.* **35**(1), 11–17.

Nimmo, J.R., (1992), Semiempirical model of soil water hysteresis, *Soil Sci. Soc. Am. J.* **56**, 1723–1730.

Nimmo, J.R., (1997), Modeling structural influences on soil water retention, *Soil Science Society of America* **61**, 712–719.

Nourmahnad, N., S. Tabatabaei and E. Hosseinipour, (2015), Effect of sewage sludge application on hydrophobicity and water retention curve of soil, *World Environmental and Water Resources Congress 2015*:2395-2402.

Oliviera, I.B., A.H. Demond, and A. Salehzadeh, (1996), Packing of sands for the production of homogeneous porous media, *Soil Science Society of America* **60**, 49–53.

Parsekian, A. D., G. Grosse, J. O. Walbrecker, M. Müller-Petke, K. Keating, L. Liu, B. M. Jones, and R. Knight, (2013), Detecting unfrozen sediments below thermokarst lakes with surface nuclear magnetic resonance, *Geophysical Research Letters*, **40**(3), 535–540.

Pawar, S. D., P. Murugavel, and D. M. Lal, (2009), Effect of relative humidity and sea level pressure on electrical conductivity of air over Indian Ocean, *Journal of Geophysical Research* **114**, 1–8.

Personna, Y.R., L. Slater, D. Ntarlagiannis, D.D. Werkema, and Z. Szabo, (2013), Complex resistivity signatures of ethanol biodegradation in porous media, *Journal of Contaminant Hydrology* **153**C:37-50.

Pohlmeier, A., S. Haber-Pohlmeier, and S. Stapf, (2009), A fast field cycling nuclear magnetic resonance relaxometry study of natural soils, *Vadose Zone Journal* **8**(3), 735–742.

Porion, P., A.M. Faugère, P. Levitz, H. Van Damme, A. Raoof, J.P. Guilbaud, and F. Chevoir, (1998), A NMR investigation of adsorption/desorption hysteresis in porous silica gels, *Magn. Reson. Imaging* **16**(5-6), 679–682.

Porion, P., A.M. Faugère, L.J. Michot, E. Paineau, and A. Delville, (2010), Orientational microdynamics and magnetic-field-induced ordering of clay platelets detected by 2H NMR spectroscopy, *Langmuir* **26**(10), 7035–7044.

Racz, A. J., A. T. Fisher, C. M. Schmidt, B. S. Lockwood, and M. Los Huertos, (2012), Spatial and temporal infiltration dynamics during managed aquifer recharge, *Ground Water* **50**(4), 562–570.

Rassi, E.M., S.L. Codd, and J.D. Seymour, (2011), Nuclear magnetic resonance characterization of the stationary dynamics of partially saturated media during steady-state infiltration flow, *New Journal of Physics* **13**(1), 015007-1–15.

Reedy, R.C. and B.R. Scanlon, (2003), Soil water content monitoring using electromagnetic induction, *Journal of Geotechnical and Geoenvironmental Engineering* **129**(11):1028-1039.

Richards, L.A., (1931), Capillary conduction of liquids through porous mediums, *Phys.* **1**(5), 318–333.

Robinson, J., L. Slater, T. Johnson, A. Shapiro, C. Tiedeman, D. Ntarlagiannis, C. Johnson, F. Day-Lewis, P. Lacombe, T. Imbrigiotta, and J. Lane, (2015), Imaging pathways in fractured rock using three-dimensional electrical resistivity tomography, *Ground Water*.

Romero, E. and P.H. Simms, (2008), Microstructure investigation in unsaturated soils: a review with special attention to contributions of mercury intrusion porosimetry and environmental scanning electron microscopy, *Geotechnical and Geological Engineering*, **26**(6):705–727.

Ryu, S., (2009), Effects of inhomogeneous partial absorption and the geometry of the boundary on population evolution of molecules diffusing in general porous media. *Physical Review E* **80**, 026109-1–16.

Schirov, M., A. Legchenko, and G. Creer, (1991), A new direct non-invasive groundwater detection technology for Australia, *Exploration Geophysics* **22**(2), 333–338.

Schwertmann, U. and R.M. Cornell, (1991), Iron Oxides in the Laboratory, Wiley-VCH.

Seevers, D.O., (1966), A nuclear magnetic method for determining the permeability of sandstones. In *Transactions of the SPWLA Annual Logging Symposium*, 1–14, Society Of Professional Well Log Analysis Houston, Texas

Slater, L., (2007), Near surface electrical characterization of hydraulic conductivity: from petrophysical properties to aquifer geometries-a review, *Surveys in Geophysics* **28**(2):169-197.

Slater, L., R. Knight, K. Singha, A. Binley, and E. Atekwana, (2006), "Near-surface geophysics: A new focus group". *Transactions, American Geophysical Union* **87**(25): 249

Smith, C.W., M.A. Johnston, and S.A. Lorentz, (2001), The effect of soil compaction on the water retention characteristics of soils in forest plantations, *South African Journal of Plant and Soil* **18**(3):87-97.

Sneider, R., S. Hubbard, M. Haney, G. Bawden, P. Hatchell, A. Revil, R. Calvert, A. Curtis, M. Fehler, P. Gerstoft, B. Hornby, M. Landro, D. Lesmes, K. Mehta, M. Mooney, C. Pacheco, S. Prejean, H. Sato, J. Schuster, K. Wapenaar, and M. Wilt, (2007), Advanced noninvasive geophysical monitoring techniques. *Annual Review of Earth and Planetary Sciences*. 35:653-683.

Stingaciu, L.R., A. Pohlmeier, P. Blumler, L. Weihermüller, D. van Dusschoten, S. Stapf, and H. Vereecken, (2009), Characterization of unsaturated porous media by high-field and low-field NMR relaxometry, *Water Resources Research* **45**(8), 1–11.

Stookey, L.L., (1970), Ferrozine-a new spectrophotometric reagent for iron, *Anal. Chem.* **42**(7), 779–781.

Sucre, O., A. Pohlmeier, A. Minière, and B. Blümich, (2011), Low-field NMR logging sensor for measuring hydraulic parameters of model soils, *J. Hydrol.* **406**(1-2), 30–38.

Swanson, R.D., K. Singha, F.D. Day-Lewis, A. Binley, K. Keating, and R. Haggerty, (2012), Direct geoelectrical evidence of mass transfer at the laboratory scale, *Water Resources Research* **48**, W10543-1–10.

Telford, W. M., L. P. Geldart, and R. E. Sheriff, (1990), *Applied geophysics*, Cambridge University Press.

Tikhonov, A.N., (1963), Solution of incorrectly formulated problems and the regularization method, *Soviet Mathematics* **4**, 1035–1038.

Timur A., (1969), Pulsed nuclear magnetic resonance studies of porosity, movable fluid, and permeability of sandstones, *Journal of Petroleum Technology* **21**(6), 775–786.

Ulrich, C. and L. Slater, (2004), Induced polarization measurements on unsaturated, unconsolidated sands, *Geophysics* **69**(3), 3762–771.

Walsh, D., (2008), Multi-channel surface NMR instrumentation and software for 1D/2D groundwater investigations, *Journal of Applied Geophysics* **66**(3–4), 140–150.

Walsh D., E.D. Grunewald, P. Turner, A. Hinnell, and T.P.A. Ferré, (2014), Surface NMR instrumentation and methods for detecting and characterizing water in the vadose zone, *Near Surface Geophysics* **12**(2), 271-284.

Walsh, D.O., E. Grunewald, and H. Zhang, (2013a), A novel NMR instrument for characterization of soil moisture, *Symposium on the Application of Geophysics to Engineering and Environmental Problems 2013*, 698–698.

Walsh, D., P. Turner, I. Frid, R. Shleby, J. Butler, C.D. Johnson, J. Cannia, D. Woodward, K. Williams, and J.W. Lane Jr., (2010), Field demonstration of slim-hole borehole nuclear magnetic resonance (NMR) logging tool for groundwater investigations, *American Geophysical Union Fall Meeting*, December 13, San Francisco, California.

Walsh, D.O., P. Turner, E. Grunewald, H. Zhang, J.J. Butler, Jr., E. Reboulet, and et al., (2013b), A small-diameter NMR logging tool for groundwater investigations. *Groundwater*, **51**(6), 914–926.

Whittall, K.P., M.J. Bronskill, and R.M. Henkelman, (1991), Investigation of analysis techniques for complicated NMR relaxation data, *Journal of Magnetic Resonance* **95**, 221–234.

Washburn, E.W., (1921), The dynamics of capillary flow, *Phys. Rev.* **17**(3), 273.

Weller, A., S. Nordsiek, and W. Debschutz, (2010), Estimating permeability of sandstone samples by nuclear magnetic resonance and spectral-induced polarization. *Geophysics*, **75**(6), E215–E226.

Weichman, P.B., E.M. Lavely, and M.H. Ritzwoller, (2000), Theory of surface nuclear magnetic resonance with applications to geophysical imaging problems. *Pysical Review E*, **62**, 1290–1312.

Whalley, W.R., E.S. Ober, and M. Jenkins, (2013), Measurement of the matric potential of soil water in the rhizosphere. *J. Exp. Bot.*

Wynn, J., (2002), Evaluating groundwater in arid lands using airborne magnetic/EM methods: an example in the southwestern U.S. and northern Mexico, *The Leading Edge*, January **21**:62:64.

Yao Y., D. Liu, J. Liu, and S. Xie, (2015), Assessing the water migration and permeability of large intact bituminous and anthracite coals using NMR relaxation spectrometry. *Transport Porous Media*, **107**(2), 527–542.

Yaramanci, U., G. Lange, and M. Hertrich, (2002), Aquifer characterisation using Surface NMR jointly with other geophysical techniques at the Nauen/Berlin test site. *Journal of Applied Geophysics* **50**(1-2), 47–65.

Yaramanci, U. and M. Müller-Petke (2009), Surface nuclear magnetic resonance—A unique tool for hydrogeophysics. *The Leading Edge* (October), 1240–1247.

Appendix: Methodology

A.1 Imbibition Experiment

The imbibition experiment is presented in Chapter 2 to collect the data shown in Figures 2-3, 2-4, 2-7, and 5-1. Water is pumped at a low flow rate into a sample holder filled with unconsolidated porous media. The sample holder is suspended within an NMR laboratory instrument. NMR measurements are collected at set intervals to collect measurements as saturation varies during imbibition. The sample holder and experimental apparatus are described in Figure A-1.

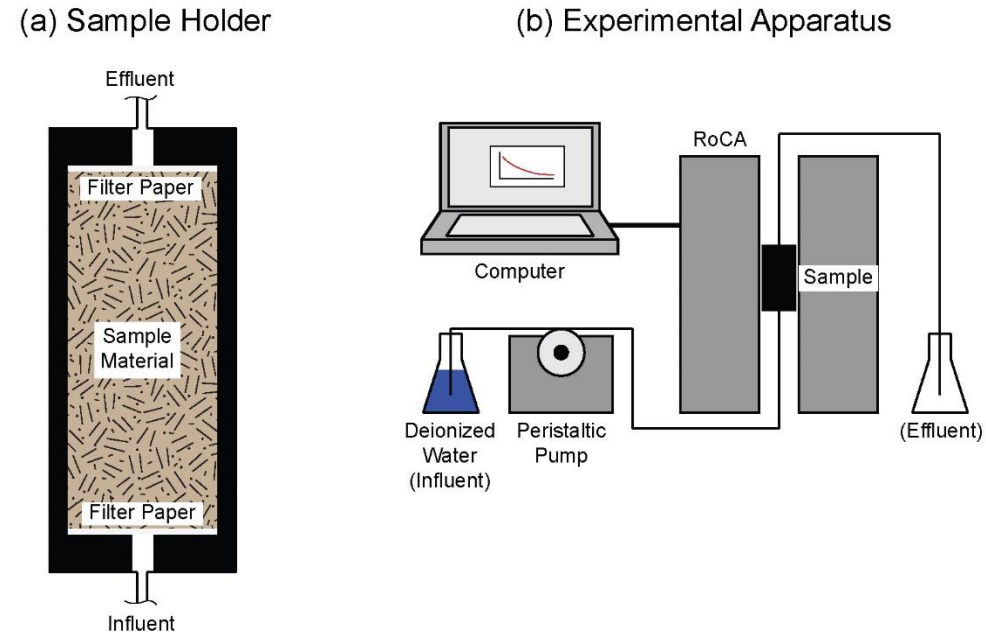

Figure A-1. The imbibition experiment sample holder (a) and experimental apparatus (b) used to collect the data presented in Chapter 2.

A.1.1 Sample holder

The sample holder (Figure A-1a) is designed to maintain the packing of an unconsolidated porous media and to allow water to flow through the sample. It includes two removable caps at both ends of the holder body in order to allow loading of material. Filter paper is placed at the base of each cap in order to maintain the integrity of the packing. A port in each cap allows water to pass through the sample material. The sample holder has an internal volume of 77.3 cm^3 (Lexan: inner diameter 2.9 cm, inner height 11.7 cm).

A.1.2 Experimental apparatus

The sample holder is suspended within the NMR instrument (Magritek Rock Core Analyzer) so it is positioned in the homogeneous static magnetic field, in the center of the machine (Figure A-1b). To position the holder at the correct height, it is set on a PVC pipe cut to length, which rests on the table within the bore of the instrument. Vinyl tubing is routed from a reservoir of deionized water located outside the instrument to a peristaltic pump, and then to the influent port on the sample holder through the bottom of the instrument. Another vinyl tube is routed from the effluent port on the sample holder to an effluent reservoir outside the instrument from the top.

A.1.3 Experimental procedure

After the sample was positioned in the NMR instrument, an initial "dry" measurement was first collected on the sample. At the start of the experiment, the influent tubing was primed using the peristaltic pump, so that the line and fitting at the bottom of sample holder was filled with water. Deionized water was then pumped through the sample holder at a rate of 50 μL/min, while NMR measurements were collected. The NMR instrument was programed to loop continuously in order to collect measurements every 20 min. throughout the experiment. Samples took between ~9-12 hours to saturate. Following the end of a sample run, sample material was removed and dried at 80^0C overnight to be used for additional measurements.

A.2 Porous Plate Experiment

The porous plate experiment is presented in Chapter 3 to collect the data shown in Figures 3-1, 3-2, 3-3, 3-4, 3-5, 3-6, and 5-1. Different saturation states are simulated during drainage and imbibition by varying ψ with a vacuum source. The experiment is used to measure the WRC under equilibrium conditions, and to obtain corresponding NMR measurements. The sample holder and experimental apparatus are shown in Figure A-2.

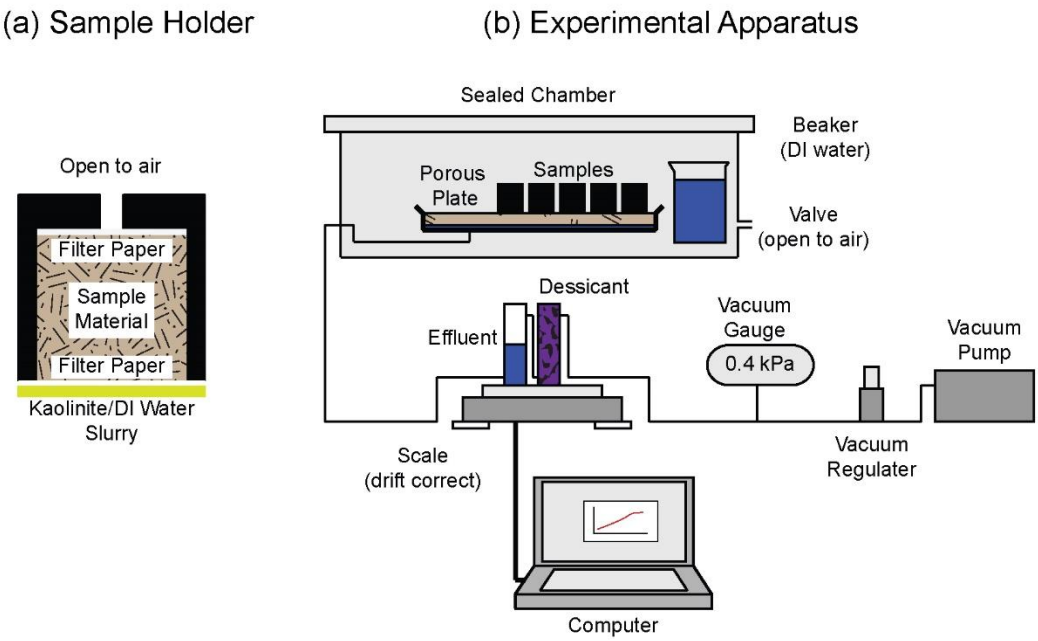

Figure A-2. The porous plate experiment sample holder (a) and experimental apparatus (b) used to collect the data presented in Chapter 3.

A.2.1 Sample holder

The sample holder (Figure A-2a) is designed to allow changes in saturation of an unconsolidated porous material, while maintaining the integrity of the sample packing. A port at the top of the sample holder is open to allow the free flow of air to and from the sample material. The bottom of the sample holder is open to allow hydraulic conductivity with water within the porous plate. In order to maintain the packing, filter paper is placed at both the top and bottom of the sample holder. The filter paper at the bottom is fixed to the sample holder with room temperature vulcanizing silicone. The bottom filter paper is coated with an approximate 1-to-1 mixture of kaolinite clay and deionized water.

A.2.2 Experimental apparatus

A porous plate with a known air entry value (Figure A-2b), or the value of ψ at which the plate will desaturate. In the case of this experiment, a plate with an air entry value of ~-50 kPa was used. The minimum value of ψ must be greater than this value to avoid desaturating the plate. The porous plate has a nylon grid attached to the bottom by a rubber liner in order to maintain the flow of water to and from the plate. Water must remain in contact with the plate at all times during the experiment.

All sample holders are fixed to the porous plate with the kaolinite clay mixture. The samples and porous plate are located within a sealable chamber in order to control evaporation. Beakers of water are placed inside the chamber to control the humidity. A valve to the chamber is left open to allow the flow of air to and from the samples. A tube is routed from the port on the porous plate liner to a double chamber reservoir outside the chamber. This reservoir is used to gravimetrically monitor the flow of water to and from the samples. The tube first connects to the bottom of a chamber halfway filled with water. Water must remain in the water chamber during the course of the experiment. A tube is then routed from the top of the water chamber to the bottom of the second chamber, which is filled with desiccant. The second chamber is used to control evaporation from the water chamber, and must also be placed on the scale. The tube is then routed from the top of the desiccant chamber to a vacuum regulator, which is used to set ψ. A vacuum gauge is installed between the regulator and the desiccant chamber to monitor ψ. A tube is finally routed from the regulator to a vacuum pump. The scale is connected to a computer with a serial port or USB connection, and used to monitor the changes in the mass of the reservoir.

A.2.3 Experimental procedure

The ψ was decreased to induce drainage, and increased to induce imbibition. Equilibrium conditions were assumed to be attained when the change in mass was <0.01g for 4 hours; which took between 1-4 weeks depending on the degree of saturation of the samples (longer for low saturations). When these conditions were met, the vacuum pump was turned off, the samples were removed from the porous plate, cleaned of any kaolinite clay mixture and weighted to determine the θ. NMR measurements were then collected using the Magritek Rock Core Analyzer. While the samples were removed from the plate, all kaolinite clay mixture remaining on the porous plate was removed and the water reservoir was replenished if needed. After NMR analysis, the samples were recoated with the kaolinite clay mixture and placed back on the plate. The chamber was then resealed, the water/desiccant reservoir positioned back on the scale, and the vacuum pump restarted. The new value of ψ was set using the vacuum regulator, and monitoring on the computer was then reset.